Tip-induced Superconductivity in Topological Semimetals

Thesis submitted for the partial fulfilment of the degree of

Doctor of Philosophy

By

Leena

Department of Physical Sciences

Indian Institute of Science Education and Research

(IISER), Mohali, Sector 81, S. A. S. Nagar, Manauli,

PO: 140306, Punjab, India.

June, 2017

Dedicated to

my parents

Declaration

The work presented in this thesis has been carried out by me under the guidance of Dr. Goutam Sheet at Indian Institute of Science Education and Research (IISER) Mohali. This work has not been submitted in part or in full for a degree, a diploma, or a fellowship to any other university or institute. Whenever contributions of others are involved, every effort is made to indicate this clearly, with due acknowledgment of collaborative research and discussions. This thesis is a bonafide record of original work done by me and all sources listed within have been detailed in the bibliography.

Date:

Place :

Leena

In my capacity as the supervisor of the candidate's thesis work, I certify that the above statements by the candidate are true to the best of my knowledge.

Dr. Goutam Sheet (Supervisor)

Acknowledgment

First of all, I wish to express my sincere gratitude to my supervisor Dr. Goutam Sheet for his invaluable advice and timely support without which this work would not has been possible. I would like to take this occasion to thank him for providing me a great chance to have an expertise on low temperature point-contact spectroscopy. He always gave me an insight to accomplish the research problems with an entirely different perspective and mentor me like a friend. I cannot forget his wonderful company and the overnight discussions on various topics. The enthusiastic and an outstanding personality he has towards research always motivated me and influenced my graduate life. He always provided me an environment which helped me to increase my work efficiency and helped me to be a good researcher.

I am very thankful to Prof. N. Sathyamurthy, Director at IISER Mohali for his support. My sincere gratitude to my doctoral committee members Dr. Yogesh Singh and Dr. Sanjeev Kumar for their invaluable help and regular feedback during my PhD tenure. I thank my collaborators Prof. Ashok Ganguli, Dr. Gohil Thakur and Zeba Haque from Indian Institute of Technology (IIT), Delhi; Prof. Claudia Felser, Dr. Chandra Shekhar, Vicky Süß from Max Plank Institute, Germany; Dr. Prabhat Mandal from Saha Institute of Nuclear Physics (SINP), Kolkata; Dr. Kaniska Biswas, Satya N. Guin, Devendra S. Negi, Ranjan Datta, Ananya Banik, Shashwat Anand from Jawaharlal Nehru Centre for Advanced Scientific Research (JNCASR), Bangalore; Dr. Somobrata Acharya, Subrata Maji, Piyush Kanti Sarkar, Sujoy Kumar Ghosh, Dipankar Mandal from Indian Association for the Cultivation of Science (IACS), Kolkata for providing high quality samples during scanning probe microscopy and point-contact spectroscopy measurements. My sincere thank to Prof. Umesh Wagmare from Jawaharlal Nehru Centre for Advanced Scientific Research (JNCASR), Bangalore for providing theoretical explanations to my research

ideas. I couldn't have completed my PhD work without the help and support from the staff of the physics department at IISER Mohali.

This work would not have been successfully completed without the help of some of the very important people. I would like to say many thanks to my colleagues Dr. Sirshendu Gayen and Dr. Shilpa Sanwlani for having valuable discussions and for encouraging me during my PhD work. Along with them I would like to thank Sandeep for giving me feedback during my thesis writing. I would also like to thank my labmates Ritesh, Shekhar, Aslam, Balal, Sandeep, Anshu, Suman, Soumya, Aastha, Mamta, Aashi, Neetu, Soumya, Shamma, Ashwini, Kavita, Anzar, Amit, Shalender for being my friend and to make this journey memorable. I am very much thankful to Abhishek, Ashima, Avtar, Jithin, Shubhra, Preetha, Aaveg, Lalit, Dr. Jagmeet and Prateek for being my good friends and providing valuable assistance. I would like to specially thank Avtar Singh for constantly supplying liq. Helium and many things that were required as part of my work. I would like to thank Mr. Subhash Pai from Excel Instruments for his help for the Point Contact Spectroscopy probe and importantly to Mukesh Kumar for machining work whenever I required during my work. I am also grateful to Neetika, Nirmal, Geeta, Shallu, Shelly, Priyanka, Ashardeep and many others.

I would like to thank all my teachers from high school to graduate school who helped me to reach this phase of my life. I would'nt be able to mention all names but I would like to thank Dr. K. P. Yogendran from Indian Institute of Science Education and Research (IISER), Triputi, Dr. Dinesh Agarwal from Inter-University Accelerator Center (IUAC) Delhi, Dr. Ashok Kumar from Delhi University, Delhi and Dr. Samar Silhotra, Punjab University, Chandigarh for helping me to choose right career direction. My special thanks to Mr. Soumil (Pikki) for becoming my first and best friend in the lab.

I dedicate this thesis to my parents and family for their unconditional support and love in good and bad times. I would like to thank my brother Rajeev and his

wife Pooja; my sister Deep and her husband Sudhir, Mamta and her husband Neeraj for their motivation and love. They helped me to become a good human being. One thing that I would like to mention here is that I always “Thank God”.

List of Publications:

1. Mesoscopic superconductivity and high spin-polarization coexisting at metallic point contacts on Weyl semimetal TaAs, **Leena Aggarwal**, Sirshendu Gayen, Shekhar Das, Ritesh Kumar, Vicky Süß, Chandra Shekhar, Claudia Felser & Goutam Sheet, *Nature Communications* 8, 13974 (2017).

2. Unconventional Superconductivity at Mesoscopic Point-contacts on the 3- Dimensional Dirac Semi-metal Cd_3As_2, **Leena Aggarwal**, Abhishek Gaurav, Gohil S. Thakur, Zeba Haque, Ashok K. Ganguli & Goutam Sheet, *Nature Materials* 15, 32 (2016).

3. Local Ferroelectricity in SnTe above Room Temperature Driven by Competing Phonon Instabilities and Soft Resonant Bonding, **Leena Aggarwal**, Ananya Banik, Shashwat Anand, Umesh V. Waghmare, Kanishka Biswas & Goutam Sheet, *Journal of Materiomics* 2, 196 (2016).

4. Mesoscopic superconductivity discovered at metallic point-contacts on the topological crystalline insulator $Pb_{0.6}Sn_{0.4}Te$, Shekhar Das, **Leena Aggarwal**, Subhajit Roychowdhury, Mohammad Aslam, Sirshendu Gayen, Kanishka Biswas & Goutam Sheet, *Applied Physics Letters* 109, 13 (2016).

5. Enhanced zero-bias conductance peak and splitting at mesoscopic interfaces between an s-wave superconductor and a 3D Dirac semimetal, **Leena Aggarwal**, Sirshendu Gayen, Shekhar Das, Gohil S. Thakur, Ashok K. Ganguli & Goutam Sheet, *Applied Physics Letters* 109, 252602 (2016).

6. Self-oriented -Crystallinity in Poly (vinylidene fluoride) Ferroelectric and Piezo-sensitive Ultra-thin Langmuir-Schaefer Film, Subrata Maji, Piyush Kanti Sarkar, **Leena Aggarwal**, Sujoy Kumar Ghosh, Dipankar Mandal, Goutam Sheet & Somobrata Acharya, *Phys. Chem. Chem. Phys.* 17, 8159 (2015).

7. Direct evidence of strong local ferroelectric ordering in a thermoelectric semiconductor, **Leena Aggarwal**, Jagmeet S. Sekhon, Satya N. Guin, Ashima Arora, Devendra S. Negi, Ranjan Datta, Kanishka Biswas & Goutam Sheet, *Applied Physics Letters* 105, 113903 (2014).

8. Voltage induced local hysteretic phase switching in silicon, Jagmeet S. Sekhon, Leena Aggarwal & Goutam Sheet, *Applied Physics Letters* 104, 162908 (2014).

9. Tip-induced Superconductivity in the Topological Semimetal ZrSiS, **Leena Aggarwal**, Mohammad Aslam, Chandan Singh, Sirshendu Gayen, Prabhat Mandal, Mukul Kabir & Goutam Sheet, To be submitted.

Abstract

In this thesis, we have shown the emergence of a tip-induced superconducting phase (TISC) at mesoscopic junctions between a normal metal (Ag) and a topological Dirac (Cd_3As_2) or Weyl semimetal (TaAs) or nodal semimetal (ZrSiS). The emerging interfacial superconductivity under a mesoscopic junction is unexpected and novel because the materials forming the mesoscopic contacts are non-superconducting in nature. From theoretical considerations it is believed that the topological semimetals exist close to the topological phase boundaries and can be driven into topologically distinct phases by breaking certain symmetries. The emerging TISC on the topological semimetals discussed in the thesis are most possibly due to topological phase transitions driven by the metallic point-contacts. In order to investigate the nature of the superconducting phase in such cases, we have done transport and magneto-transport based spectroscopic measurements by employing point-contact spectroscopy (PCS). PCS is an energy resolved spectroscopic measurement technique which involves mesoscopic contacts between two materials. PCS on superconducting materials provides useful information about the energy gap and its symmetry in the momentum space.

In addition to this work on topological semimetals, we have also studied physical properties of several semiconductors using different modes of scanning probe microscopy (SPM). The modes include Atomic force microscopy (AFM), Piezoresponse force microscopy (PFM), Magnetic force microscopy (MFM) *etc.*. Through PFM we have shown the existence of local ferroelectric ordering in certain semiconducting materials like $AgSbSe_2$ and SnTe which also have superior thermoelectric properties. From PFM experiments on a number of non-ferroelectric systems (Silicon, printed circuit board *etc.*) we have shown that PFM cannot be used as a "smoking gun" of ferroelectricity. In this context we have shown the ferroelectric-

like hysteresis behavior emerging on silicon. We have also shown nano-structuring on silicon using AFM lithography.

To justify the above works, we have chosen the following thesis plan:

Chapter I is an introduction to the work presented in the thesis. It includes discussion on methods and attempts that have been made to investigate the superconducting phase on topologically non-trivial materials in the past. This chapter highlights the advantage of point-contact spectroscopy to explore TISC on topological materials, where bulk characterization tools fail. It also includes detailed discussion of PCS on mesoscopic NS junctions in different regimes of transport followed by the discussion of theoretical model has been used to analyze the PCS spectra. In order to highlight all the key features in different regimes of transport for a superconducting point-contact, we have also shown representative differential conductance (dI/dV) spectra on a known conventional superconductor, lead (Pb) by making a metallic point-contact using silver (Ag) tips.

Chapter II describes the instrumentation and experimentation of a point-contact probe. A point contact spectroscopy probe is developed in-house to carry out dI/dV measurements at low temperatures down to 1.5 K and high magnetic field of about 6 Tesla. The schematic picture of the home-built point-contact probe.The data acquisition set-up and method also developed in house has also been discussed.

Chapter III shows emergence of an unexpected superconducting phase at the mesoscopic point-contacts between pure silver (Ag) and a 3D Dirac semi-metal Cd_3As_2. Such a phase a critical temperature more than 8 K while neither Cd_3As_2 nor Ag are superconductors. Further, point-contact made on Cd_3As_2 with a superconducting tip of Nb we have shown the emergence of a pronounced zero-bias conductance peak which undergoes splitting in energy under certain conditions, indicating the possibility of Majorana bound states as expected at the interfaces between s-wave superconductors and topologically non-trivial materials with high degree of spin-orbit coupling.

Chapter IV deals with tip induced superconductivity on the Weyl semimetal tantalum arsenide (TaAs). A mesoscopic contact on TaAs/Ag shows a superconducting transition at a temperature of 7 K. Moreover, the magnetic field and temperature dependent spectra show systematic evolution with magnetic field as expected for superconducting point-contacts. A suppression of Andreev reflection amplitude is also seen which can be attributed to the existence of spin polarization at the surface of TaAs. All the spectra obtained on TaAs are remarkably fitted well using BTK model, which is traditionally for conventional superconductors. Therefore, our results indicate that there is coexistence of conventional superconductivity and spin-polarization at the point-contact on TaAs.

Chapter V introduces another highly stable and fascinating material that belongs to the family of topological semimetals–the so-called topological nodal semimetal ZrSiS. A novel superconducting phase with a remarkably high T_c of 7.5 K is induced in single crystals of ZrSiS by a non-superconducting metallic tip of Ag. This superconducting phase is expected to co-exist with the well preserved topological properties of ZrSiS thereby emerging as a strong candidate for topological superconductivity.

Chapter VI deals with SPM measurements on certain semiconductors like $AgSbSe_2$, SnTe *etc.*. Through such measurements, for the first time, we have shown the existence of a new type of multi-functional materials where nano-scale ferroelectric domains coexist with superior thermoelectric properties. We named them ferroelectric thermoelectrics. The materials in which such unique coexistence was observed include $AgSbSe_2$ and SnTe. In this chapter we also discuss another important technical observation regarding PFM. From PFM experiments on a large number of non-ferroelectric systems we have shown that PFM hysteresis and "butterfly loops" cannot be considered a "hallmark signatures" of ferroelectricity. In this context, we have shown that hysteretic phase switching can be observed in popular semiconductors like Silicon, a material that is frequently used as a base

material/substrate for PFM measurements. Our results show that in such cases, a "fake" ferroelectric-like signal might emerge from the underlying substrate itself. Furthermore, in this chapter we have also shown how nano-meter scale topographic structures can be written on Silicon through AFM lithography under ambient conditions.

Chapter VII contains a brief summary of the main results of the present thesis.

CONTENTS

1 Introduction

The investigation of superconductivity in materials harbouring exotic quasiparticles like Dirac, Weyl or Majorana fermions [1–4] has drawn tremendous attention in contemporary condensed matter physics. A newly discovered class of materials with non-trivial band structures, known as topological materials [5–7], host such exotic quasiparticles. Such systems also exist close to topological phase boundaries which, in principle, make it possible to drive them into further exotic phases of matter like topological superconductors, for example. Partial realization of such an idea has been achieved through chemical doping [8–10] and applying high pressure [11–16] into such systems. For example, when Cu is intercalated into otherwise non-superconducting bismuth selenide (Bi_2Se_3) [15], a layered topological insulator, shows superconductivity below 3.8 K and bismuth telluride (Bi_2Te_3) [16] another topological insulator belonging to the same class shows superconductivity with $T_C =$ 3 K under a pressure of 3-6 GPa. In this thesis, we report a new method of inducing superconductivity and studying the nature of superconductivity in such systems by simply making mesoscopic point contacts using normal elemental metals. Such a superconducting phase induced by a non-superconducting tip is referred to as "tip-induced superconductivity (TISC)" in literature.

Since the newly discovered method helps realization of a new mesoscopic superconducting phase in the form of superconducting nano-droplets under points of contact between different materials, traditional bulk characterization tools for characterizing superconductors [17] e.g., four-probe resistance and magnetization measurements fail to provide much information regarding the superconducting phase. We have shown that such a phase, however, can be detected through transport and magneto-transport based spectroscopic measurements in different regimes of mesoscopic transport. [18–21] Such a phase emerges only under a confined geometry between a tip and a topologically non-trivial material — this discovery opens up

a new direction in understanding the emergence of superconductivity from a new perspective and hints to significant application potential in nano-electronic devices which may pave the way for fault-tolerant quantum computing [22, 23] through the experimental realization of Majorana fermions. [24]

In the following section, I will discuss how a superconducting phase that emerges only under mesoscopic point contacts can be detected and confirmed by exploring the spectroscopic signatures in different regimes of transport that are unique to superconducting point contacts.

1.1 Tip Induced Superconductivity (TISC)

Bulk superconductors are perfect conductors as well as perfect diamagnets and are traditionally characterized by zero resistance and negative susceptibility. [17] These two important properties of superconductivity are challenging to observe under point contact even for known superconductors. The reasons for non-zero resistance for superconducting point-contacts are: (a) the resistance of the non-superconducting component of the point-contacts, [18] (b) finite number of conducting channels [25] and (c) possible mismatch of the Fermi-velocities in the two materials forming the point-contacts. [18, 26] Hence measurement of "zero-resistance" is not necessarily a hallmark signature of superconductivity under point contacts. Testing the perfect diamagnetism of the confined region under point contact is also challenging due to extremely low expected signal to noise ratio compared to what is usually achieved in a lab. Therefore, in order to detect the superconducting nature that emerges on the non-superconducting materials under point-contacts, we have performed PCS. [18,27] There are several strong spectroscopic signatures in addition to sharp resistive transition to confirm the superconducting phase emerging only under point contacts, which we discuss in the following sections.

1.2 Point-contact spectroscopy (PCS)

Transport of electrons through a macroscopic metal is characterized by Ohm's law which exhibits linear $I-V$ curve [19], showing a finite resistance because of inelastic scattering from various scattering centers like phonons in metals, magnons in magnets and impurities. However, when electrons transport through a narrow constriction between two metals with diameter (a) smaller than the mean scattering length (l) of electrons within the constriction, the electrons do not undergo any scattering statistically and the electrons accelerate to attain higher and higher kinetic energy. When the kinetic energy is sufficiently high, the electrons can undergo scattering from the elementary excitation modes thereby leading to non-linearities in the $I-V$ characteristics. Through such mechanism, energy resolved spectroscopy can be performed which gives various spectroscopic informations of the materials. PCS is an experimental technique to perform such measurements.

1.2.1 Transport of electrons through a metallic point-contact

There are several methods to perform PCS like needle-anvil, shear method, break junctions and lithography to fabricate mesoscopic junctions. [18] We have used "needle-anvil" method in which a sharp tip of a material is brought in contact with the other material in such a way that the two electrodes just touch each other and make a mesoscopic ohmic contact. The schematic of a PCS experiment is shown in Figure 1.1. It depicts a point-contact between two metals through which electrons transport from one metal to another. Four electrical connections are made to perform transport measurements.

The resistance to electronic transport between two metals is given by Wexler's formula [25] as shown below:

$$R_{PC} = \frac{2h/e^2}{(ak_F)^2} + \Gamma(l/a)\frac{\rho(T)}{2a} \tag{1}$$

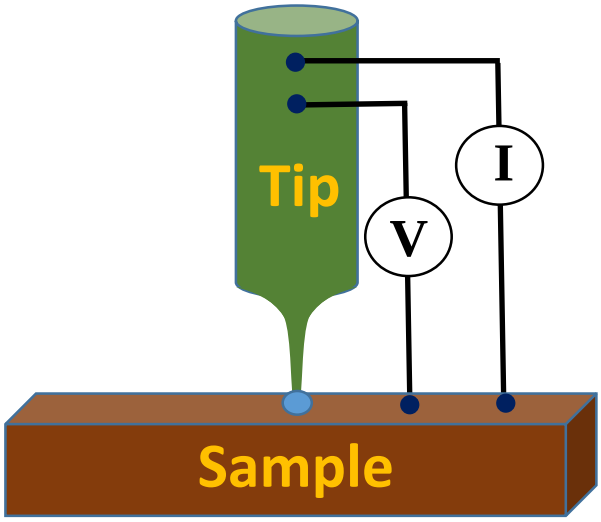

Figure 1.1: The schematic diagram of PCS experiment, showing a point-contact between two metals.

In the above equation, h is the Planck's constant, e is the charge of a single electron, a is the contact diameter. ρ is the bulk resistivity of the material and T is the effective temperature at the point-contact. Γ (gamma function) varies from 0.7 to 1 with the decrease of l/a ratio from ∞ to zero. Formula shows that the resistance of a point-contact between two metals depends upon mainly two parameters. The primary parameter is contact diameter 'a' between the sample and the tip. And second one is the mean free path 'l' (elastic or inelastic) of an electron. Depending upon l/a ratio, transport of electrons can be categorized into different regimes *i.e.* quantum/ ballistic/ thermal/ intermediate regime.

Quantum Regime: When the point-contact diameter is in the order of angstrom *i.e.* de-Broglie wave length then conductance gets quantized, which is given by $G_0 = N \times \frac{2e^2}{h}$, where N is number of the conducting channels. [30]

Ballistic Regime: A point-contact is in the ballistic regime when the point-contact diameter becomes larger than the de-broglie wave length and smaller than the electronic elastic mean free path (l_e) i.e. $a < l_e$. In this regime, statistically, the electrons do not suffer any inelastic scattering within the contact and they move ballistically without any dissipation. However, because of large number of conducting channels and physical properties of point-contact, there is always some

finite resistance at a mesoscopic contact which is equal to the Sharvin's resistance (R_S) represented as a first term in the equation (1). The first term of the equation (1) depends only on the geometry of the point-contact. [31]

Thermal Regime: In thermal regime, the contact diameter is larger than the inelastic electronic mean free path of electrons (l_i) i.e. $a > l_i$ where inelastic scattering becomes more prominent. The point-contact resistance in this regime is represented by Maxwell's resistance (R_M) *i.e.* the second term in equation (1). It depends directly on the resistivity of the materials forming the point-contact. Because of inelastic scattering, a large part of energy is dissipated.

Intermediate Regime: When the point-contact diameter lies somewhere in between two extreme regimes *i.e.* ballistic and thermal regimes, the point-contact is said to be in an intermediate regime. In this regime both Sharvin's resistance and Maxwell's resistances contribute. The contact resistance is given by Wexler's equation (1).

Similarly, PCS has been used to study the superconducting properties of a superconductor by replacing one of the metal forming a point-contact by a superconductor. The electronic transport in the ballistic regime through an NS interface is governed by Andreev Reflection (AR). It provides energy resolved spectroscopic information of two materials and gives the superconducting energy gap. In the next section, we will discuss AR in more details. We will also introduce the theoretical model given by Blonder, Tinkham, Klapwijk (BTK), that has been traditionally used to study AR in superconducting point-contacts. A modified BTK model including spin polarization of the fermi surface will be discussed.

1.2.2 Transport of electrons through a superconducting point-contact

1.2.2.1 Point-contact AR spectroscopy: Ballistic regime of transport:

Figure 1.2 shows the schematic diagram of AR process which describes the electronic transport from a metal to a superconductor in an NS junction. [32] The quasipar-

ticle density of states (DOS) profile of a superconductor is shown along with the superconducting energy gap (Δ). Since the superconducting energy gap is usually in the order of meV, DOS profile of a normal metal side can be approximated to be flat.

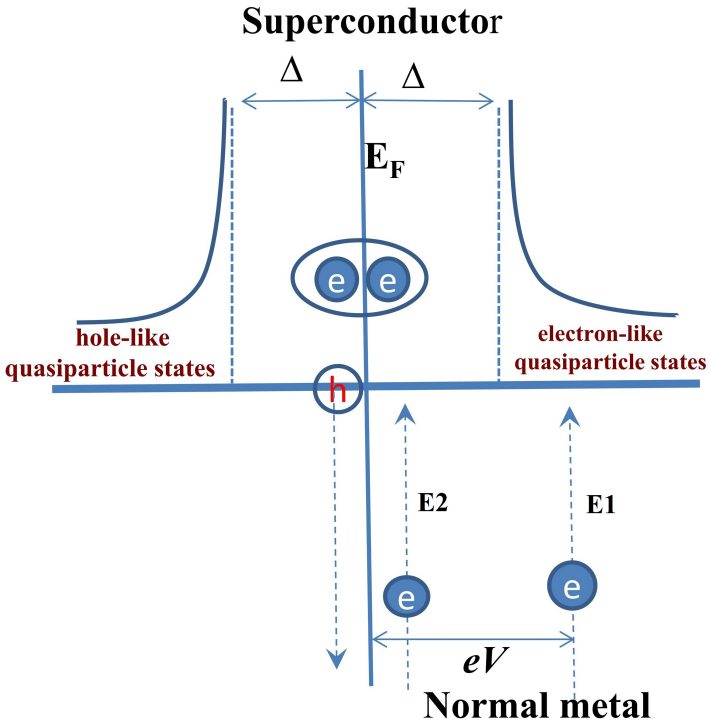

Figure 1.2: The schematic diagram of AR process describing electronic transport through an NS junction from a metal to a superconductor in the ballistic regime of transport. The dotted lines represent the superconducting energy gap in the quasiparticle density of state of a superconductor and dotted arrows representing the 'trajectory' of electron and hole through an NS junction under different bias.

Generally, electrons passing through an NS junction undergo three processes (1) Normal transmission (2) Normal reflection (3) AR. [20] When interface is biased such that electrons in the metal side have energy E1 (shown in figure 1.2), electrons transmit to the superconductor side due to presence of accessible states for electrons in that side. However, when the applied dc bias is such that the electronic energy lies within the superconducting gap i.e. E2 (shown in figure 1.2), then electrons can not undergo normal transmission because of superconducting energy gap where only cooper pairs can exist. There no accessible state for a single particle to move within the superconducting energy gap. At that energy scale electrons can undergo normal reflection or AR or both depending upon the strength of the potential barrier at the

interface. An electron reflects as a hole and for conservation of charge a cooper pair propagates in the superconductor and consequently conductance gets enhanced. A simulated normalized differential conductance, $((dI/dV)_N)$ versus V spectrum (also called PCAR spectrum) is shown in figure 1.3 (a). It shows that within the gap conductance becomes twice than outside the gap for a transparent point-contact at $T=0$.

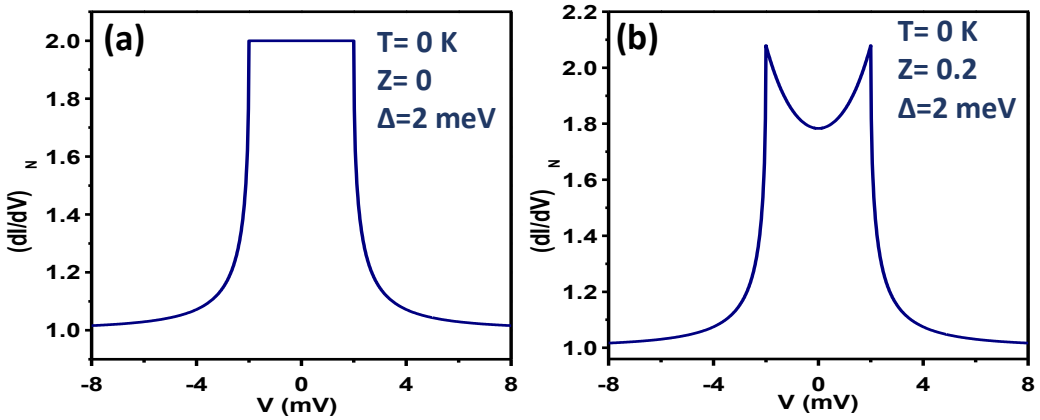

Figure 1.3: The BTK simulated $((dI/dV)_N)$ vs. V spectra at T=0 K and $\Delta=2\,meV$ (a) without barrier ($Z=0$) and (b) with finite barrier ($Z=0.2$). Here 'Z' is a dimensionless quantity i.e. $Z=\frac{V_0}{\hbar v_F}$ where, v_F is fermi velocity. It represents the barrier strength at NS interface.

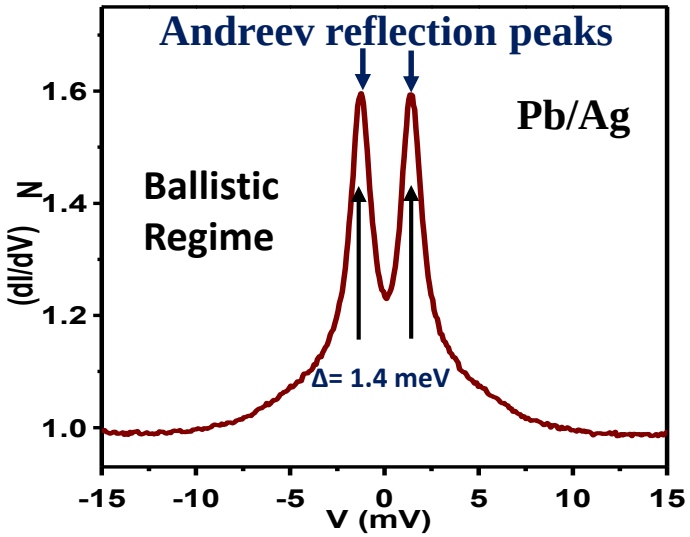

Figure 1.4: A $(dI/dV)_N$ vs. V spectrum on Pb/Ag point contact in the ballistic regime of transport.

In practice, there is always a finite barrier at the interface which results in two peaks in the spectrum symmetric about $V=0$. These peaks are called AR peaks

which give directly an estimated value of superconducting energy gap (shown in figure 1.3 (b)).

In figure 1.4, we have introduced experimentally obtained $(dI/dV)_N$ vs. V point-contact spectrum in ballistic regime of transport on a known superconductor, lead (Pb) by making a metallic point-contact with silver (Ag) tip. The two symmetric peaks about $V=0$, a hallmark of AR peaks, provide an estimated value of superconducting energy gap which is approximately 1.4 meV in this case.

BTK formalism: The theoretical model to analyze the PCAR spectrum is given by Blonder, Thinkham and Klapwijk (BTK) [33]. This is one dimensional model. The model considers all the possible processes like transmission, reflection and AR occur at NS junctions where electrons move perpendicular to the interface of two materials. The model considers a delta function, $H=V_0\delta(x)$ for the junction. BTK model has also taken care of barrier at the junction due to presence of oxide layer or fermi mismatch of materials, by adding a parameter i.e. Z. It represents barrier width which is a dimensionless parameter, $Z=\dfrac{V_0}{\hbar v_F}$, where, v_F is fermi velocity. In order to simulate PCAR spectrum by BTK model, we first calculate a expression for $I-V$ curve. We consider a wave function for electron and hole as below,

$$\psi=\begin{bmatrix} f(x,t) \\ g(x,t) \end{bmatrix} \tag{2}$$

$f(x,t)$ and $g(x,t)$ are electron and hole wave function respectively. Bogoliubov-de Gennes [17] equations for these wave functions are written as follow:

$$\iota\hbar\frac{\partial f}{\partial x}=[-\frac{\hbar^2\nabla^2}{2m}-\mu(x)+V(x)]f(x,t)+\Delta(x)g(x,t) \tag{3}$$

$$\iota\hbar\frac{\partial g}{\partial x}=-[-\frac{\hbar^2\nabla^2}{2m}-\mu(x)+V(x)]g(x,t)+\Delta(x)f(x,t) \tag{4}$$

Here, $\Delta(x)$ is the energy gap, $\mu(x)$ is the chemical potential. The trial wave functions to calculate the current at the interface are:

$$\psi = \begin{bmatrix} u \\ v \end{bmatrix} e^{\frac{\iota kx - \iota Et}{\hbar}} \tag{5}$$

$$f = ue^{\frac{\iota kx - \iota Et}{\hbar}} \& g = ve^{\frac{\iota kx - \iota Et}{\hbar}} \tag{6}$$

$$E = \sqrt{[\hbar^2 k^2/2m - \mu]^2 - \Delta^2} \tag{7}$$

$$u^2 = \frac{1}{2}[1 + \frac{\sqrt{(E - \Delta^2}}{E}] \tag{8}$$

$$v^2 = 1 - u^2 \tag{9}$$

Then incident, reflected and transmitted wave functions are:

$$\Psi_{inc} = \begin{bmatrix} 1 \\ 0 \end{bmatrix} e^{\iota kx} e^{\iota Et/\hbar} \tag{10}$$

$$\Psi_{refl} = [a \begin{bmatrix} 0 \\ 1 \end{bmatrix} e^{\iota kx} + b \begin{bmatrix} 1 \\ 0 \end{bmatrix} e^{-\iota kx}] e^{-\iota Et/\hbar} \tag{11}$$

$$\Psi_{tran} = [c \begin{bmatrix} u \\ v \end{bmatrix} e^{\iota kx} + d \begin{bmatrix} v \\ u \end{bmatrix} e^{-\iota kx}] e^{-\iota Et/\hbar} \tag{12}$$

Where coefficients a and b are given by $a = u_0 v_0/\gamma, b = -(u_0^2 - v_0^2)(Z^2 + \iota Z)/\gamma$. u_0^2 and v_0^2 are the probabilities of an electronic state being occupied and unoccupied respectively:

$$u_0^2 = \frac{1}{2}[1 + \frac{\sqrt{(E + \iota\Gamma) - \Delta^2}}{E + \iota\Gamma}], v_0^2 = 1 - u_0^2 \tag{13}$$

Γ represents the shortening of quasiparticle life times due to inelastic scattering near the contacts which is discussed as a modified BTK model separately. However, in a simple BTK model, only elastic scattering is considered at N/S interface, therefore, Γ is remained zero here.

$$\gamma^2 = \gamma\gamma^*, \gamma = u_0^2 + (u_0^2 - v_0^2)Z^2 \tag{14}$$

The boundary conditions for particles moving at $x = 0$ from normal metal to superconductor are as follow:

(i) Ψ at $x = 0$, so $\Psi_S(0) = \Psi_N(0)$

(ii) $(\hbar/2m)(\Psi_S^{'} - \Psi_N^{'}) = H\Psi(0)$, the derivative of boundary condition for delta function.

If electrons tunnel through an NS junction then number of occupied states is $N_N(E)f(E)$ and number of unoccupied final states is $N_S(E + eV)[1 - f(E + eV)]$. Here, $N_N(E)$ is density of states of the normal metal, $N_S(E)$ is density of states of the superconductor and $f(E)$ is the Fermi function. For reverse current joint probability for this process is $N_N(E)f(E+eV)N_S(E+eV)[1-f(E)]$. By subtracting the reverse current from the forward current, net current through an NS junction is [20, 33]

$$I_{NS} = \alpha\,|\,T\,|^2 \int_{-\infty}^{+\infty} N_N(E)N_S(E+eV)[f(E-eV) - f(E)][1+A(E)-B(E)]dE \tag{15}$$

where α is the constant that depends upon the junction and fermi velocity. $|\,T\,|^2$ is a phenomenological tunneling matrix element that depends on the type of insulator between the N/S junction and governs whether the event occurs. In practice, $N_N(E) = N_N(0)$, then differential conductance at T= 0 is given as below:

$$G_{NS} \equiv \frac{dI_{NS}}{dV} \mid_{T=0} \propto N_S(e \mid V \mid) \tag{16}$$

The calculated dI/dV gives the density of states of a superconductor which is observed in the tunneling regime spectrum [34] as shown in figure 1.5 with high Z value i.e. $Z = 2$. In PCAR electrons move through a point-contact and suffer scattering during transport, therefore, Z should be small. If we use the BTK formulation to incorporate ARs (Andreev reflections), the current that flows across the junction is:

$$I_{ballistic} \propto \int_{-\infty}^{+\infty} [f(E - eV) - f(E)][1 + A(E) - B(E)]dE \tag{17}$$

$A(E)$ is the AR probability and $B(E)$ is the normal reflection probability that is given by $A(E) = aa^*$ and $B(E) = bb^*$ respectively.

$$A_{\mathrm{u}}(E) = \frac{\Delta^2/E^2}{1 - \epsilon(1 + 2Z^2)^2}, for E < \Delta \tag{18}$$

$$A_{\mathrm{u}}(E) = \frac{(uv)^2}{\gamma^2}, for E > \Delta \tag{19}$$

$$B_{\mathrm{u}}(E) = 1 - A(E), for E < \Delta \tag{20}$$

$$B_{\mathrm{u}}(E) = \frac{((u)^2 - (v)^2)^2 Z^2(1 + Z^2)}{\gamma^2}, for E > \Delta \tag{21}$$

$$\gamma^2 = (((u)^2 - (v)^2)Z^2 + (u)^2)^2 \tag{22}$$

$$\epsilon = (E^2 - \Delta^2)/E^2 \tag{23}$$

The expression for the dI/dV of an NS junction corresponding to the AR process

at $T=0$ is given as below:

$$G_{ballistic} = \frac{dI_{NS}}{dV}\,|_{T=0} \propto (1 + A(eV) - B(eV)) \tag{24}$$

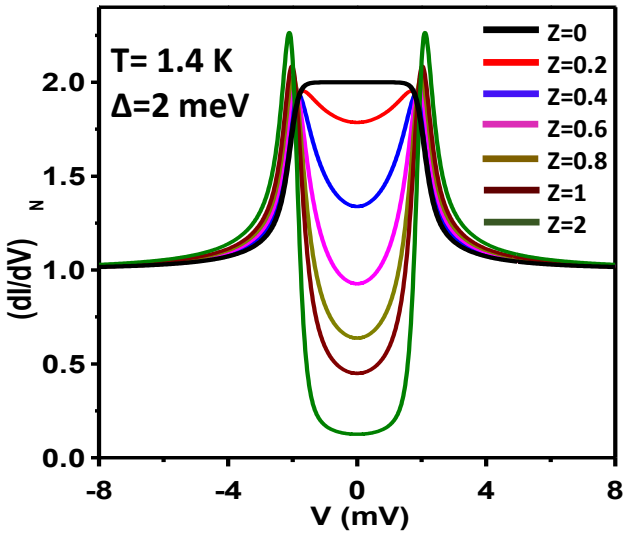

Figure 1.5: The simulated $(dI/dV)_N$ vs. V spectra using BTK theory at T=1.4 K and $\Delta = 2\,meV$ with variation in Z. It is showing the transition of point-contact spectra from transport regime (low Z value) to tunneling regime (high Z value).

In this equation 1+A(E)-B(E) [33] represents transmission coefficient for electrical current. This coefficient incorporates the fact that when a hole is reflected a positive charge moves in the opposite direction of the incident electron. Such a current is represented by A(E) and will add to the incident current. Similarly, reflected electrons are represented by B(E) and will reduce the current. Figure 1.5 represents $(dI/dV)_N$ vs. V spectra using above expression with different Z values. The represented BTK simulated spectra show the transition of point-contact transport regime (low Z) to tunneling regime (high Z) at $T = 1.4\,K$. In the case of $Z = 0$ (transparent interface), the reflection process govern only Andreev process. In the case of strong surface barrier $(Z^2(u^2 - v^2) >> 1)$, there is no AR and shows only quantum tunneling process.

BTK has also introduced the expression for dI/dV at different temperatures. In figure 1.6, simulated $(dI/dV)_N$ is presented at $\Delta = 2\,meV$ and $Z = 0.2$ with variation in temperature from 0 K to 30 K, showing thermal broadening. With increase in T

Andreev peaks are smeared out finally leave a single zero-bias.

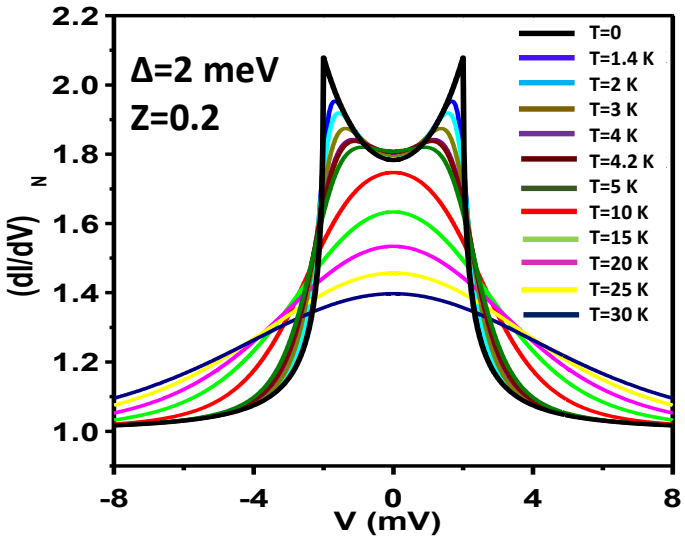

Figure 1.6: The simulated $(dI/dV)_N$ vs. V spectra using BTK thoery at finite barrier width, $Z = 0.2$ and $\Delta = 2\,meV$ with variation in temperature (T), showing thermal broadening.

Modified BTK theory with spin polarization: As per BTK theory [33,35] when the point contact is between a superconductor and an unpolarized (normal) metal, the current is given by

$$I_{\mathrm{u}} = C \int_{-\infty}^{+\infty} [f(E - eV) - f(E)][1 + A_{\mathrm{u}}(E) - B_{\mathrm{u}}(E)]dE \tag{25}$$

Where, $A_{\mathrm{u}}(E)$ is the AR probability and $B_{\mathrm{u}}(E)$ is the normal reflection probability for an unpolarized current. For a fully polarized current, the same formula can be used by replacing A_{u} and B_{u} with A_{p} and B_{p} respectively. A_{p} and B_{p} are respective probabilities for a fully spin polarized Fermi surface of the non-superconducting electrode forming the point contact. The subscripts u and p denote the coefficients for the unpolarized and polarized current respectively. $A_{\mathrm{u}}(E)$, $B_{\mathrm{u}}(E)$, $A_{\mathrm{p}}(E)$ & $B_{\mathrm{p}}(E)$ were calculated using the following formula:

for the entire range of E:

$$A_{\mathrm{p}}(E) = 0 \tag{26}$$

$$B_{\mathrm{p}}(E) = 1, for E < \Delta \tag{27}$$

$$B_{\mathrm{p}}(E) = \frac{(\sqrt{\frac{E^2-\Delta^2}{E^2}} - 1)^2 + 4Z^2(\frac{E^2-\Delta^2}{E^2})}{(\sqrt{\frac{E^2-\Delta^2}{E^2}} + 1)^2 + 4Z^2(\frac{E^2-\Delta^2}{E^2})}, for E > \Delta \tag{28}$$

$$A_{\mathrm{u}}(E) = \frac{\Delta^2}{E^2 + (\Delta^2 - E^2)(1+2Z^2)^2}, for E < \Delta \tag{29}$$

$$A_{\mathrm{u}}(E) = \frac{(u^s v^s)^2}{\gamma^2}, for E > \Delta \tag{30}$$

$$B_{\mathrm{u}}(E) = 1 - A(E), for E < \Delta \tag{31}$$

$$B_{\mathrm{u}}(E) = \frac{((u^s)^2 - (v^s)^2))^2 Z^2(1+Z^2)}{\gamma^2}, for E > \Delta \tag{32}$$

$$\gamma^2 = (((u^s)^2 - (v^s)^2)Z^2 + (u^s)^2)^2, \tag{33}$$

Here u^s and v^s are obtained from the solution of the Bogoliubov-de Gennes (BdG) equation in the superconductor:

$$(u^s)^2 = 1 - (v^s)^2 = 1/2[1 + \sqrt{\frac{E^2 - \Delta^2}{E^2}}] \tag{34}$$

$$Z = \frac{V_0}{\hbar v_F} \tag{35}$$

After calculating the I_{u} and I_{p} we have simply written the total modified current including the transport spin polarization P_{t} as

$$I_{\mathrm{mod}} = (1 - P_{\mathrm{t}})I_{\mathrm{u}} + P_{\mathrm{t}} I_{\mathrm{p}} \tag{36}$$

We have plotted the simulated data using BTK theory in figure 1.7 at different values of polarization, P. It shows that the normalized zero bias conductance drops from 2 when $P=0$ to 0 when $P=1$ (100 %). This is used to fit the experimental dI/dV curves to determine the transport spin polarization, P_{t}. [36].

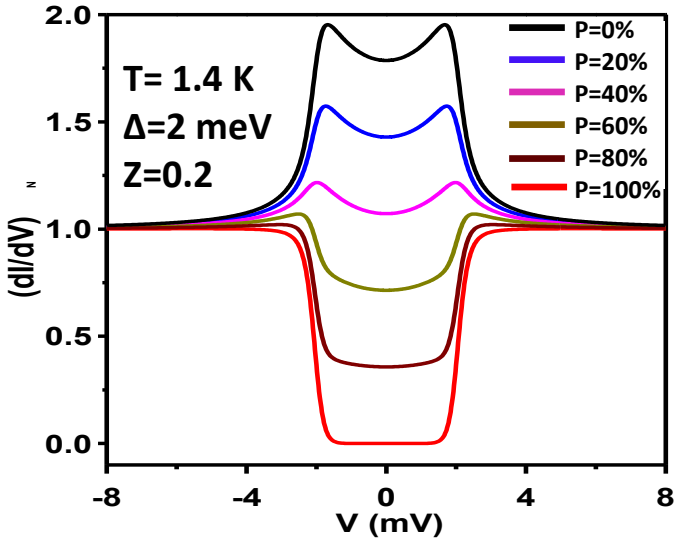

Figure 1.7: The simulated $(\mathrm{dI/dV})_N$ vs. V spectra using BTK thoery at $T=1.4\,K$ and $\Delta=2\,meV$ with variation in P values from 0% to 100% .

Modified BTK theory for unconventional superconducting phase: The BTK formalism is valid for PCAR spectrum obtained between a conventional superconductor and a normal metal and usually shows sharper features than experimentally observed spectra. This is because, it considers only elastic scattering at N/S interface, however, experimentally electrons also suffer with inelastic scattering. Therefore, to incorporate the broadening of peaks [37], one more parameter, Γ is involved. Γ [37] represents the shortening of quasiparticle life times due to inelastic scattering at the contacts.

The broadening could be accounted by adding an imaginary component Γ to Energy E, i.e., $E \rightarrow E + i\Gamma$. In such fittings, the value of Γ was constrained to be very small, i.e., smaller than 10% of Δ. Physically adding an imaginary component to the energy means introducing finite lifetime of the quasiparticles. Therefore, Γ should be small compared to Δ. Otherwise, the superconducting phase cannot be

stable.

$$\iota\hbar\frac{\partial f}{\partial x} = [\frac{\hbar^2\Delta^2}{2m} + \mu(x) + \iota\Gamma - V(x)]f(x,t) + \Delta g(x,t) \tag{37}$$

$$\iota\hbar\frac{\partial g}{\partial x} = -[\frac{\hbar^2\nabla^2}{2m} + \mu(x) + \iota\Gamma - V(x)]g(x,t) + \Delta f(x,t) \tag{38}$$

$$f = ue^{\frac{\iota tx - \iota Et - \Gamma t}{\hbar}} \tag{39}$$

$$g = ve^{\frac{\iota tx - \iota Et - \Gamma t}{\hbar}} \tag{40}$$

$$I_{ballistic} = C\int_{-\infty}^{+\infty}[f(E - eV) - f(E)][1 + A(E) - B(E)]dE \tag{41}$$

$A(E) = aa^*$ and $B(E) = bb^*$, where the coefficients a and b are given by

$$a = u_0v_0/\gamma \tag{42}$$

$$b = -(u_0^2 - v_0^2)(Z^2 + \iota Z)/\gamma \tag{43}$$

where u_0^2 and v_0^2 are the probabilities of an electronic state being occupied and unoccupied respectively which are written as:

$$u_0^2 = \frac{1}{2}[1 + \frac{\sqrt{(E + \iota\Gamma) - \Delta^2}}{E + \iota\Gamma}] \tag{44}$$

$$v_0^2 = 1 - u_0^2 \tag{45}$$

$$\gamma = u_0^2 + (u_0^2 - v_0^2)Z^2 \& \gamma^2 = \gamma\gamma^* \tag{46}$$

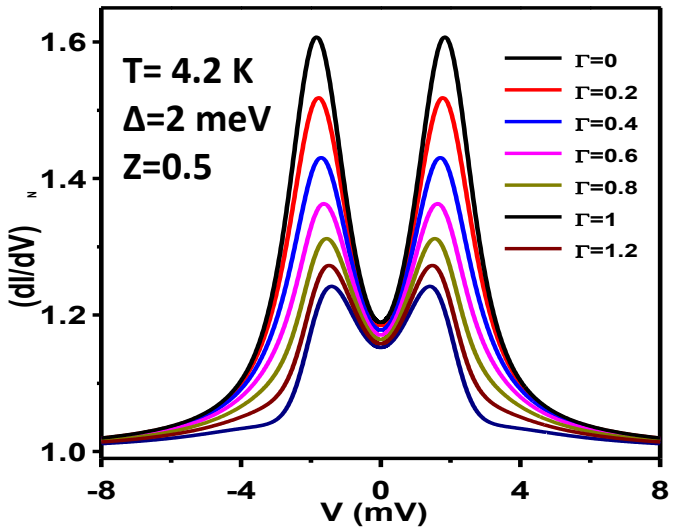

Figure 1.8: The simulated $(dI/dV)_N$ vs. V spectra using BTK theory at T=1.4 K and $\Delta = 2\,meV$, changing Γ values.

Figure 1.8 shows the simulated $(dI/dV)_N$ versus V spectra with different values of Γ. They are significantly broader than the spectra without Γ. With increase in the ratio of Γ/Δ, the amplitude of $(dI/dV)_N$ gets decrease and the spectra become more broader. Hence, by addition of more fitting parameters *i.e.* Γ and P in conventional BTK model, the modified one becomes more flexible.

In order to explore other regimes of transport of point-contact, we have investigated the Pb/Ag point-contacts in thermal and intermediate regimes as well.

1.2.2.2 Transport of electrons through a superconducting point-contact: Thermal and Intermediate regimes:

In thermal regime, point-contact resistance (R_M) depends on the bulk resistivity of materials forming point-contact. Therefore, if we make a a point-contact between a superconductor and a metal and perform temperature dependent study, the point-contact shows the signature of a superconducting transition below critical temperature. In figure 1.9 (a) we have shown temperature dependent resistance measurements on Pb by forming a mesoscopic point-contact using Ag tip in thermal regime. It shows a transition at temperature around 7.2 K, which is the T_c for the bulk Pb. It also shows the evolution of critical temperature with increasing magnetic field as expected for a

superconducting point-contact.

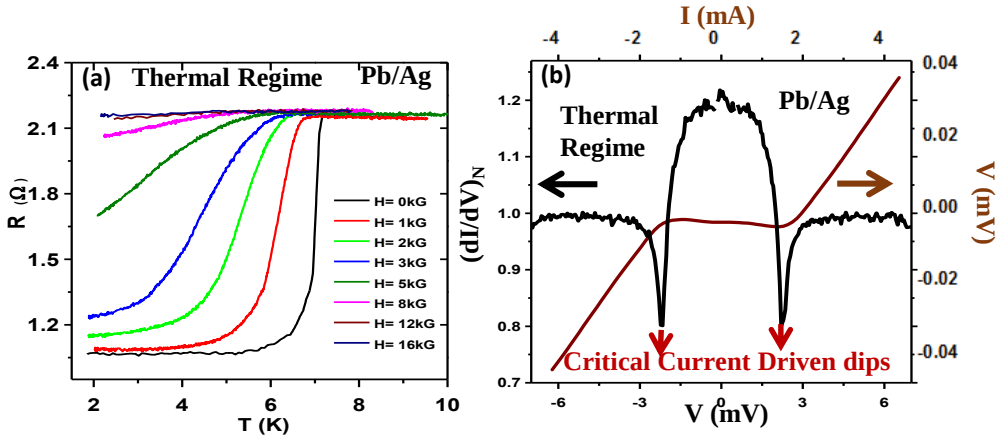

Figure 1.9: (a) Magnetic field dependence $R-T$ data on Pb/Ag point contacts in thermal regime of transport. (b) A $(dI/dV)_N$ vs. V spectrum on Pb/Ag point contact in the same point-contact as shown in (a). The dips in $(dI/dV)_N$ originate owing to the critical current of the superconducting junction. The line shows the $I-V$ curve corresponding to R_M after subtracting R_S. The flat portion shows the dissipationless current flowing through the point contact.

Further, $I-V$ curve of the same point-contact shows non-linearity corresponding to the critical current value of the superconductor and resistance of the contact is given by Wexler's formula ($R_{PC}= R_S + R_M$). From BTK theory, we can calculate an approximate $I-V$ characteristic associated with the ballistic component (R_S) of a point-contact resistance and then subtract the same from the $I-V$ associated with the total point contact resistance (R_{PC}). The resultant $I-V$ thus obtained is associated with the Maxwell's contribution (R_M) alone. The resultant $I-V$ characteristic of the same point-contact leads to the non-linearity in the $I-V$ curve (shown in figure 1.9 (b)). The flat portion in figure 1.9 (b) shows dissipation less current state which rises up as current flowing through the point-contact exceeds critical current value of point-contact. Such non-linearities are seen clearly in $(dI/dV)_N$ versus V spectrum as two sharp dips symmetric about $V=0$. A representative spectrum on Pb/Ag point-contact in thermal regime of transport on Pb/Ag is shown in figure 1.9 (b), showing critical current driven dips.

As the tip is withdrawn gradually from the sample the thermal regime point-contact transition to a ballistic regime through an intermediate regime. The tip

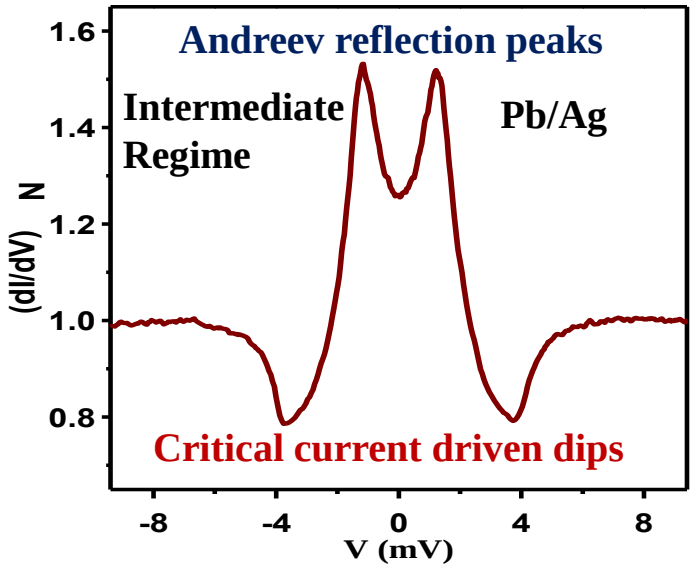

Figure 1.10: A $(dI/dV)_N$ vs. V spectrum on Pb/Ag point contacts in intermediate regime of transport.

is gradually withdrawn in small steps so as to reduce the contact area without breaking the contact and the spectra are recorded for each successive contacts. One representative spectrum in the intermediate regime on Pb/Ag point contact is shown in figure 1.10. In the intermediate regime of transport, we have found signature of critical current driven features (dips in $(dI/dV)_N$ symmetric about $V=0$) as well as AR driven features (peaks in $(dI/dV)_N$ symmetric about $V=0$) in the spectrum.

To conclude, in this chapter, we have discussed PCS in general by exploring different regimes of mesoscopic transport. The detailed discussion of PCAR spectroscopy which has been used to study the energy and spin resolved spectroscopic properties are also included. Finally, we have shown various spectral features (hallmark of TISC) in different regimes of transport under the metallic point-contact on a known superconductor, Pb. In this thesis, we discuss our recent results on the discovery of TISC phase in different topological semimetals. The organization of the thesis is as follow:

In chapter 2 we discuss details of PCS technique, instrumentation, electronics and software development followed by our results on 3D topological Dirac semimetals Cd_3As_2, Weyl semimetal TaAs and nodal semimetal ZrSiS in chapters 3 - 5.

In chapter 6 we show the high temperature measurements on the semiconducting materials using different modes of scanning based microscopy followed by summary of the thesis.

1.3 Appendix

1.3.1 Why does the point-contact resistance (R_{PC}) not become zero?

A bulk superconductor indeed shows zero resistance. However, when a mesoscopic contact is made on a superconductor with a non-superconducting metal, the contact resistance cannot usually be zero. Figure 1.9 (a) in chapter 1 shows $R-T$ data on Pb/Ag point-contact in thermal regime of transport where it is clear that the resistance does not become zero down to 1.4 K. This shows that for a superconducting point-contact, the contact resistance may not become zero. Actually, the point-contact resistance depends a lot on the size of the point contact where the contact resistance is given by Wexlers formula (as shown in equation (1)).

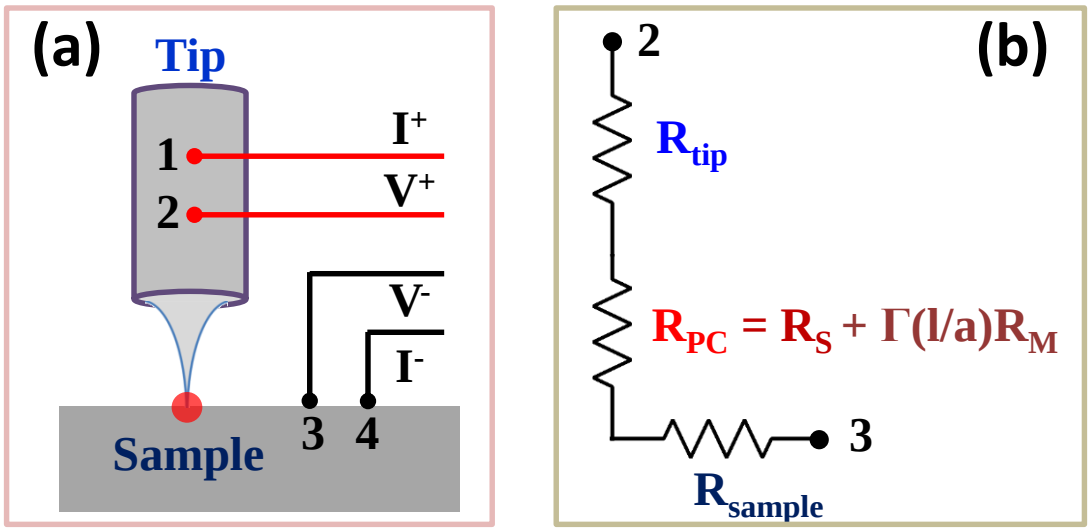

Figure A1.1: A schematic diagram showing different components of resistance that are measured in a point contact geometry.

In figure A1.1, we show how different components of resistance are measured in a point contact geometry . Even when the bulk of the superconductor transitions to the superconducting phase, the point-contact resistance must remain non-zero because (i) there is always a temperature independent Sharvin's contribution and (ii) the non-superconducting component within the current path in the point contact will always show non-zero resistance and (iii) possible mismatch of the Fermi-velocities in the two materials forming the point-contact. As illustrated in figure A1.1, even when

$R_{tip} = R_{sample} = 0$, for SS point contacts, R_{PC} can remain non-zero. Therefore, in this case, since the superconducting phase emerges only under the point contacts where the bulk of the sample continues to remain non-superconducting, measurement of "zero-resistance" is not a relevant experiment.

2 Experimental details and Instrumentation

PCS technique has played a significant role to study the superconducting properties of materials under mesoscopic contacts. In the following section, I will describe the technical details of PCS measurements followed by a discussion on the fabrication of a home-built setup for performing such experiments at low temperature.

2.1 Experimental technique

Several techniques are developed to perform PCS measurements e.g. needle-anvil [38], shear method [39], breaks junctions [40], lithography [41] etc. I have used needle-anvil method to study solid-state materials like single crystals, polycrystalline, thin films and foils. It includes a sharp tip (like a needle) of a material which is brought close to another material such that a mesoscopic contact can be formed (shown in figure 2.1).

To study different transport regimes of point-contact a pseudo four probe method (figure 2.1) was used where two leads were put on the sample and other two leads were put on the tip using silver epoxy. These four leads were used to measure the differential resistance (dV/dI) across the point-contacts to perform low temperature PCS measurements. In order to manipulate the size of the point contact a differential screw arrangement was attached with a rotator through a long stainless steel tube which can be controlled from outside the cryostat. Usually a point-contact shows the tunneling regime due to presence of an insulating layer on the surface of the tip and the sample. In order to perform PCS measurements, tip is pressed further such that very small cracks are developed on the dielectric layer which result into nano-electrical contacts.

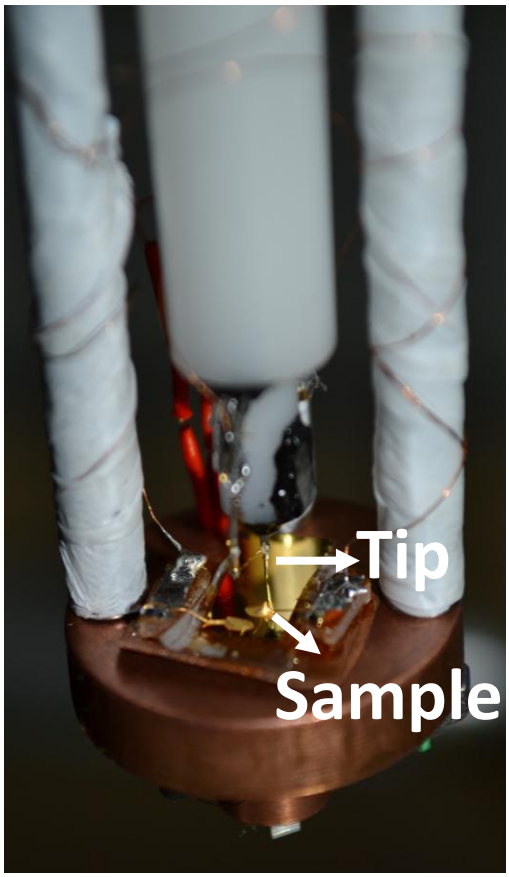

Figure 2.1: The image of bottom part of point-contact probe showing experimental arrangement of point-contact spectroscopy measurements using needle-anvil method.

2.2 Instrumentation

The low temperature measurements were performed in a liquid helium cryostat working down to 1.4 K (figure 2.2 (a)). To avoid the vibration during the measurements, the cryostat was completely isolated from the rest part of the building by using many layers of highly vibration absorbing materials like styrofoam, neoprene and quartz sand. The cryostat was equipped with a three-axis vector magnet which can apply a maximum magnetic field of 6 Tesla along the vertical direction using a superconducting solenoid and 1 T in the horizontal plane using four superconducting Helmholtz coils with AMI (American Magnetics, Inc.) controller (figure 2.2 (b)). The cryostat was also equipped with a dynamic variable temperature insert (VTI) inside which there was one static VTI as shown in figure 2.3. The bottom part of the static VTI was made of copper for efficient cooling. The sample probe was inserted

inside the static VTI which was first evacuated and then filled with exchange (dry helium) gas to cool down the sample area.

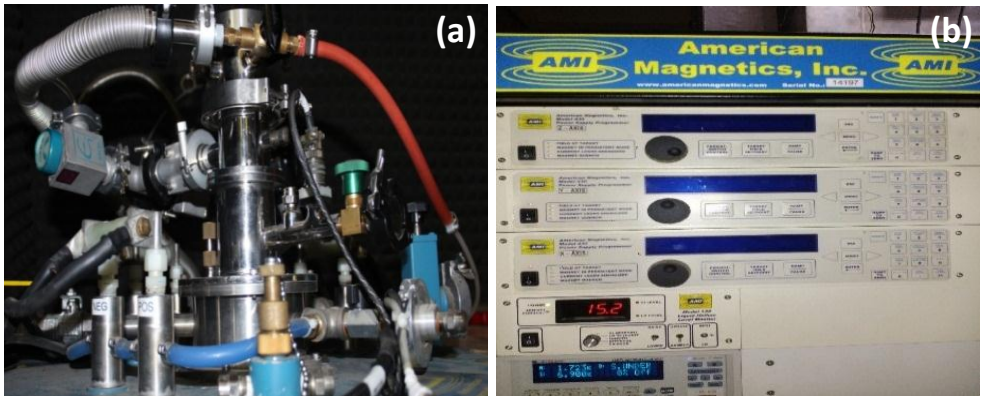

Figure 2.2: Low temperature point-contact set-up containing (a) cryostat working down to 1.4 K temperature and (b) a AMI vector controller with maximum magnetic field about 6 Tesla.

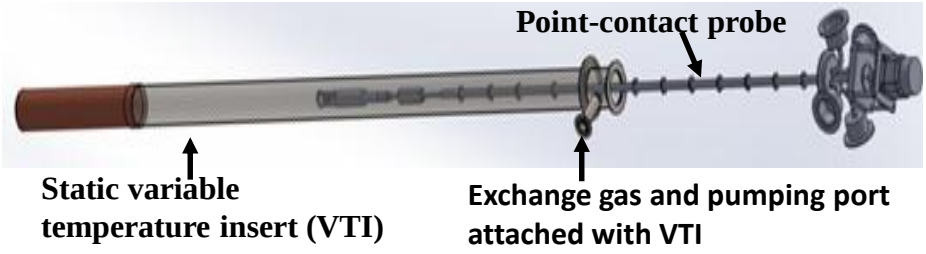

Figure 2.3: The solid work image of point-contact probe inserted in the static VTI.

2.2.1 Point-contact probe

The low temperature point-contact probe was designed and fabricated in house. The image of point-contact probe is shown in figure 2.4. The probe consists of a long stainless steel tube at the end of which the probe-head is mounted. The bottom part of the probe is equipped with a 100 threads per inch (t.p.i.) differential screw that is rotated by a shaft running to the top of the cryostat through probe head. The screw is threaded to a copper cylinder in such a way that its one end is attached to shaft and other end is attached to a copper block inside the cylinder. When we use rotator to move the screw through the shaft, cooper block moves forward and backward. That copper block is attached to a teflon cylinder to which tip is fixed.

This is the design of differential screw assembly through which linear motion of the tip is achieved. The electrical connections are made by twisted pairs of cooper wires. The sample-holder is made of a 1" dia. copper disk. A cernox thermometer is mounted on the copper disc for the measurement of temperature. The temperature of the disc is varied by a heater mounted on the same copper disc.

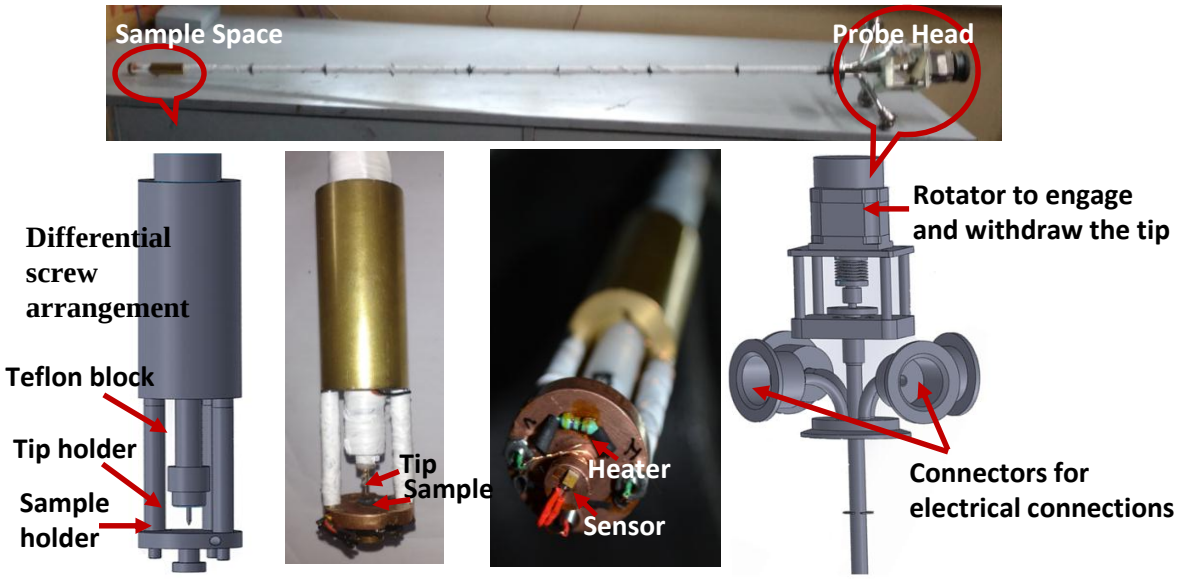

Figure 2.4: A image of a home-built point-contact probe with close view of different parts of the probe.

The tips are fabricated by cutting a 0.25 mm dia. metal wire at an angle. The tip is mounted on the tip holder and two gold contact leads are made on the tip with silver epoxy. The samples are mounted on the sample holder and two silver-epoxy contact leads are mounted on the sample as well.

2.2.2 Electronics and data acquisition set-up for analysis of PCS spectra

The differential conductance as a function of dc bias voltage across the point-contact is measured by ac modulation technique using lock-in amplifier (figure 2.5 (a)). The setup contains Stanford SS330 DSP lock-in amplifier, a dc current source (Model-6220,frequency range: few tens of Hz to few kHz, multiples of line frequency should be avoided to reduce noise level), and a multimeter (Model-2000) from Keithley Inc. A Model-350 temperature controller from Lakeshore Inc is used to monitor and

control the sample temperature.

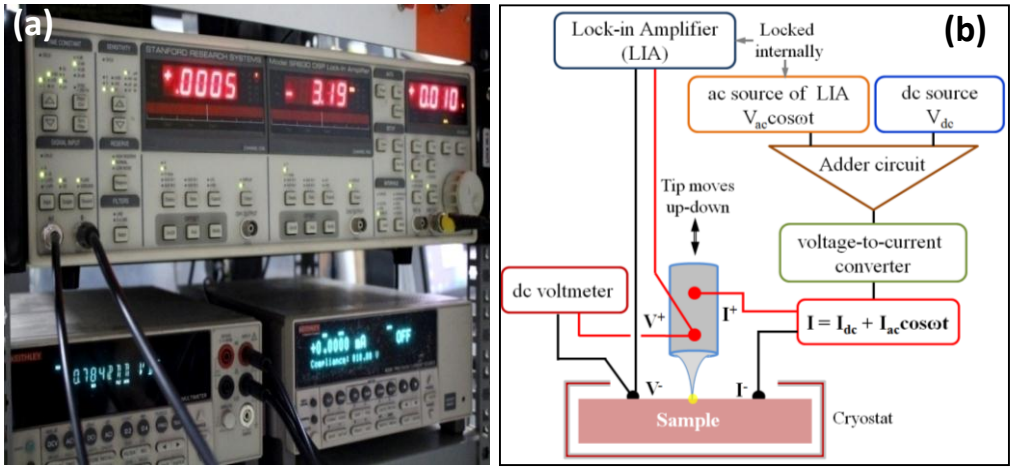

Figure 2.5: (a) A lock-in based modulation technique used to record the dV/dI with respect to V across the point-contact (measured by a digital multimeter, Keithley 2000). (b) The schematic diagram of electronics set-up for performing PCS.

The schematic of lock-in based ac modulation technique, used to obtain the point-contact spectra *i.e.* dV/dI *vs.* V data, is shown in figure 2.5 (b). A sweeping dc current I_{dc} coupled with a small fixed amplitude ac current $I_{ac}cos\omega t$ ($I_{dc} \gg I_{ac}$) from lock-in (by applying an ac voltage through a high resistance, at least thousand times the contact resistance) with internal locking is passed through the point contact and the dc output voltage across the point contact V is recorded by a voltmeter or a digital multimeter while the differential resistance dV/dI (proportional to the ac output voltage locked externally at the first harmonic) is measured by a lock-in amplifier working at 375 Hz. The signal locked at first harmonic is proportional to dV/dI (and second harmonic to d^2V/dI^2): the output voltage can be expressed by Taylor expansion, $V(I = I_{dc} + I_{ac}cos\omega t) = V(I_{dc}) + \left(\frac{dV}{dI}\right)|_{I_{dc}} I_{ac}cos\omega t + \frac{1}{2}\left(\frac{d^2V}{dI^2}\right)|_{I_{dc}} (I_{ac}cos\omega t)^2 + \cdots = V(I_{dc}) + \left(\frac{dV}{dI}\right)|_{I_{dc}} I_{ac}cos\omega t + \frac{1}{4}\left(\frac{d^2V}{dI^2}\right)|_{I_{dc}} (I_{ac})^2(1 + cos2\omega t) + \cdots$ The reason behind setting the frequency 375 Hz was to avoid multiples of 50 hz line frequency. The ac component of the input current should not be very high since this voltage determines the resolution of the measurement technique. This current is typically set such that the first harmonic response of the lock-in is roughly only 1% of the voltage scale of interest i.e., for a PCAR experiment, since the superconducting

gap is typically few millivolts, the lock in response should be of the order of few micro volts.

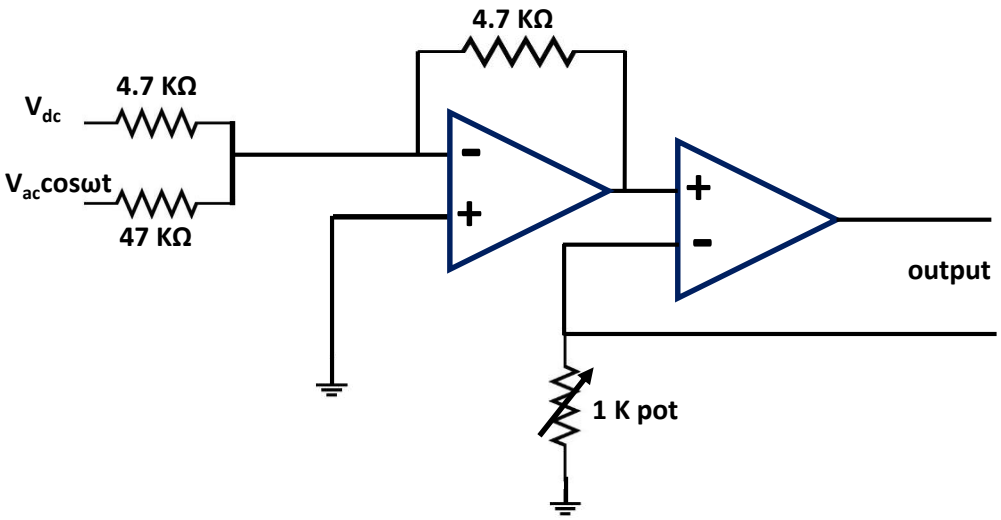

Figure 2.6: The schematic diagram of electrical circuit of an adder followed by a current converter.

Another simple alternative is using of a voltage to current (V-I) converter (figure 2.6) through which a couple signal of dc input with a very small ac input is fed across the point-contact. The data acquisition is performed through GPIB connection and the measurement is made completely automated (using LabVIEW platform) with full control over the measurement parameters like temperature and magnetic field through interactive graphic-user-interface (GUI).

3 TISC in the 3D Dirac semimetal Cd_3As_2

Although the 3D topological Dirac semi-metals [42–44] can be stable where the Dirac points are protected by symmetry, they exist close to topological phase boundaries, and therefore, they are expected to be driven into topologically distinct phases by explicit symmetry breaking. [45] The proposed new phases of matter that could be derived from a 3D topological Dirac semi-metal through explicit symmetry breaking include new topological insulators [6], Weyl semi-metals [4, 46], and topological superconductors. [47–50] Therefore, the 3D Dirac semi-metals provide a novel platform where topologically diverse quantum phase transitions can be realized. Recently the II-V semiconductor Cd_3As_2 has been shown to be a stable 3D Dirac semi-metal by angle resolved photoemission spectroscopy (ARPES) [43] and scanning tunneling spectroscopy (STS) [51] experiments. The ARPES experiments concluded that Dirac fermions exist in the bulk of Cd_3As_2 with linear energy dispersion along all three directions in the momentum space. In order to detect possible exotic phases on the topological semimetal Cd_3As_2, we have performed PCS measurements by making nanometer scale junctions between pure elemental normal metals like silver (Ag) and Cd_3As_2.

3.1 Point-contact spectroscopy: Different regimes of transport on Cd_3As_2

In figure 3.1 (a), we have shown temperature dependent resistance measurements on a mesoscopic point-contacts in thermal regime showing a transition at temperature around 7.5 K. This transition looks similar to the superconducting transition. In order to further investigate the possible superconducting nature of the point-contacts we have performed magnetic field dependence of the same point-contact. We observed that for a given point-contact the superconducting transition temperature decreases with increasing magnetic field (figure 3.1 (b)) as expected for a supercon-

ducting point-contact.

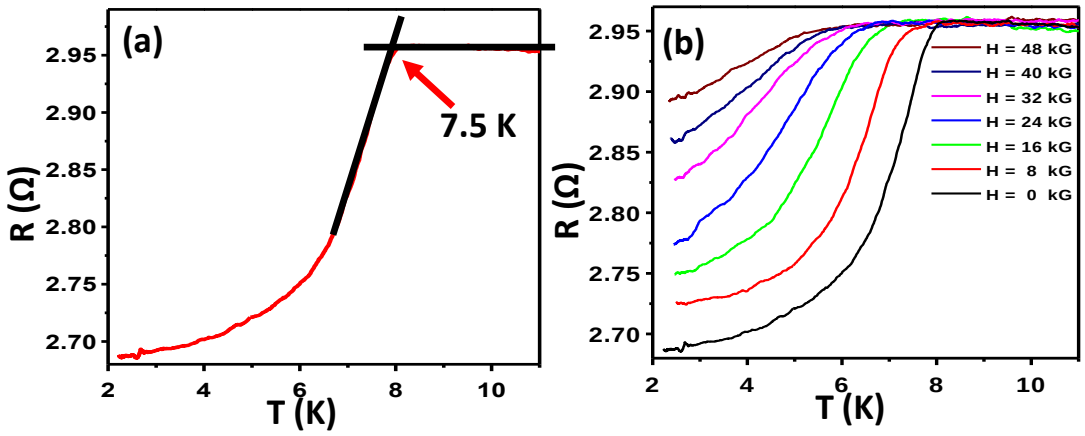

Figure 3.1: (a) A point-contact $R-T$ on Cd_3As_2 representing superconducting transition at 7.5 K (b) H-dependence of point contact $R-T$ showing systematic evolution of superconducting transition with applied magnetic field.

The measured normalized differential conductance ($(dI/dV)_N$) as a function of a dc-bias (V) developed across a thermal point-contact between Ag and Cd_3As_2 is shown in figure 3.2 (a). Two sharp dips in $(dI/dV)_N$ are observed at $\pm 5\,mV$ respectively confirming that the point-contact is superconducting [26]. The $I-V$ shown as a blue line in the figure corresponds to the total resistance of the point-contact ($R_{PC} = R_M + R_S$) [25]. We have separately calculated the $I-V$ corresponding to R_S [19] using the theory of Blonder-Tinkham and Klapwijk (BTK) for superconducting point-contacts and subtracted the same from R_{PC}. The resultant $I-V$ corresponding to R_M is shown in figure 3.2 (b) and it clearly shows dissipation less current state which rise up as current flowing through the point-contact exceeds critical current value of point-contact. Two sharp dips appear when the dc-current flowing through the point-contact reaches the critical current for the given point-contact. [18,26]. These observations show the evidence of superconducting phase on Cd_3As_2 point-contact.

By manipulating the size of contact diameter by withdrawing the tip gradually from the sample, we can speculate different regimes under the point-contacts. In the ballistic regime where Sharvin's resistance dominates, two dips are seen symmetric about $V = 0$ in the $(dI/dV)_N$ vs. V spectrum which is a hallmark of AR. [33] In figure

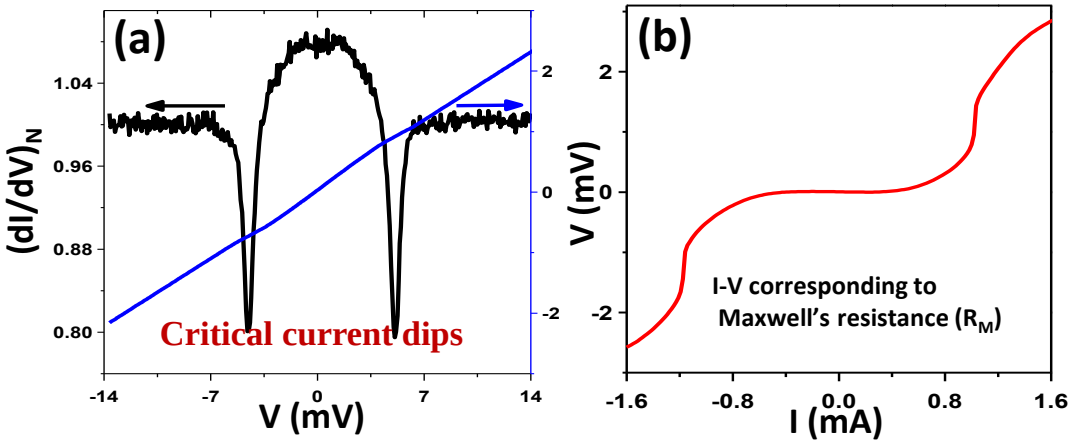

Figure 3.2: (a) A $(dI/dV)_N$ versus V spectrum close to the thermal regime: The dips in $(dI/dV)_N$ originate due to the critical current of the superconducting junction. The blue line shows the $I-V$ corresponding to the total resistance (R_M+R_S) of the point-contact. (b) The $I-V$ corresponding to R_M after subtracting R_S. This shows the dissipationless current flowing through the point-contact.

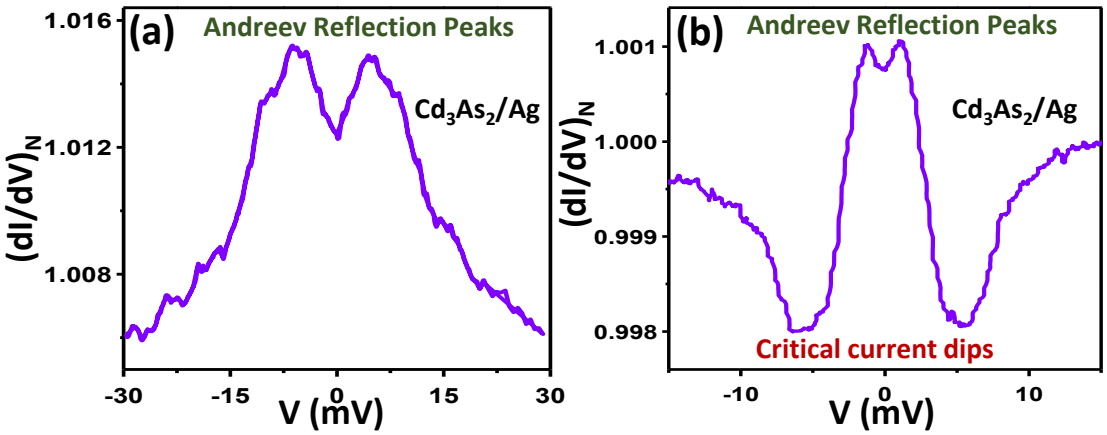

Figure 3.3: (a) A $(dI/dV)_N$ vs. V spectrum in ballistic regime of transport at Cd_3As_2/ Ag point-contact. Two peaks symmetric about $V=0$ show the AR peaks. (b) A $(dI/dV)_N$ vs. V spectrum in thermal regime of transport at Cd_3As_2/ Ag point-contact. It shows both AR peaks and critical current driven dips.

3.3 (a), a representative spectrum is obtained on the point-contact in the ballistic regime. In between two extreme regimes i.e. thermal regime and ballistic regime, the point transition through so-called intermediate regime. [26] One representative spectrum in the intermediate regime on Cd_3As_2/Ag point contact is shown in Figure 3.3 (b). In the intermediate regime of transport, we have found signature of critical current driven features (dips in $(dI/dV)_N$ symmetric about $V=0$) as well as AR driven features (peaks in $(dI/dV)_N$ symmetric about $V=0$) in the spectrum.

We have observed strikingly similar features on Cd_3As_2/Ag point-contact as observed on Pb/Ag point-contact. However, neither Cd_3As_2 nor Ag are supercon-

ductor. It may conclude that the metallic point-contacts on Cd_3As_2 are superconducting.

3.2 Magnetic field dependence

In Figure 3.4 (a), we show how the critical current dominated spectra obtained from the point-contacts close to the thermal limit evolve with magnetic field. [26] The central dip (due to superconducting transition below the critical current) in the spectra evolves smoothly with magnetic field and disappears at $H_c = 4.5\,\mathrm{T}$. The critical-current driven side-peaks also show systematic evolution with magnetic field. [18] Further, as the tip is withdrawn from the sample slowly, the thermal regime point-contacts transition to a ballistic regime through an intermediate regime. One representative spectrum in the intermediate regime is shown in Figure 3.4 (b). In the intermediate regime of transport, we have found signature of critical current driven features (peaks in $(dV/dI)_N$ symmetric about $V = 0$) as well as Andreev reflection driven features (dips in $(dV/dI)_N$ symmetric about $V = 0$) in the spectrum. In this case the gap-structure appears at a lower voltage due to the thermal contribution to the spectrum. The magnetic field dependence of the same spectrum show the evolution of the gap structure and the critical current peaks with increasing the magnetic field.

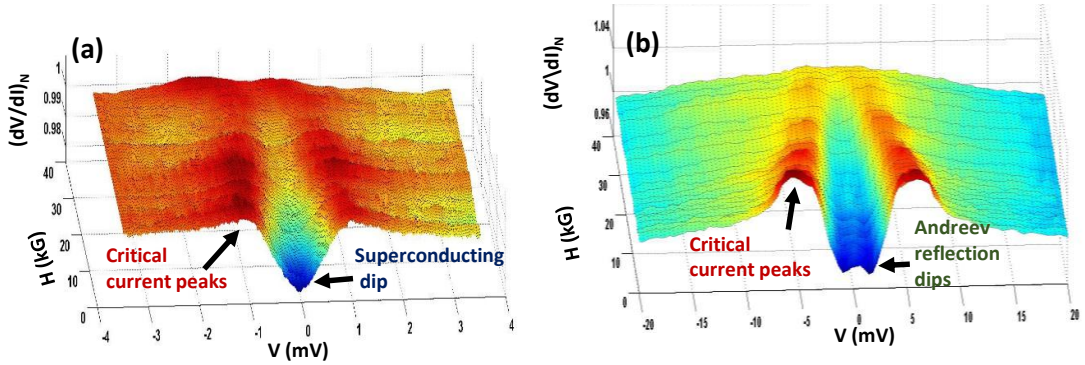

Figure 3.4: (a) Magnetic field dependence of a spectrum in the thermal regime. The peaks in $((dI/dV)_N$ due to critical current of the superconducting point-contact are indicated by arrows. (b) The magnetic field dependence of a point-contact spectrum in the intermediate regime. The peaks in $(dI/dV)_N$ originating from critical current of the superconducting point-contact and the dips in $(dI/dV)_N$ originating from the AR at the interface between Cd_3As_2 and Ag are indicated by arrows.

3.3 Unconventional Nature of Superconductivity

3.3.1 Existence of Pseudogap

In order to determining the nature of superconductivity it is important to perform spectroscopy when there is no inelastic scattering occurs under the point-contact and for that we do PCS in ballistic regime of transport. [18] A ($(dI/dV)_N$) vs. V spectrum in ballistic regime is shown in figure 3.5 (a), we observe Andreev peaks appear at 6.7 meV, which is a hallmark of AR [33]. It is also observed that the peaks

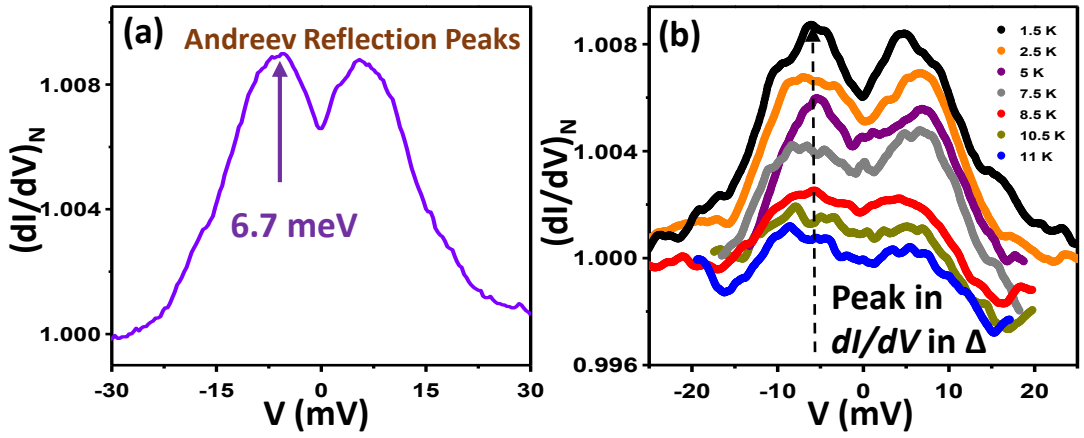

Figure 3.5: (a) Spectrum captured from a point-contact in the ballistic regime of transport showing the gap (Δ) features. The spectra have been given a vertical shift for visual clarity. The scheme of computing Δ is also shown. (b) The temperature dependence of Δ. In this plot we show more data points than the number of spectra shown. Δ survives above 13 K which is more than 2 times T_c and does not show considerable temperature dependence indicating the presence of a pseudogap.

are significantly broader than what is expected from BTK theory that is traditionally used to analyze AR spectra obtained on conventional BCS superconductors. [52, 53] This might be due to a large inelastic broadening [37]parameter at the interface and/or an unconventional pairing. In order to analyze such spectra quantitatively a theoretical model for AR taking into account the non-trivial topological properties of one of the electrodes forming the point-contact must be developed. Nevertheless, the position of the peaks provides an approximate estimate of the gap. [33] From the spectra provided in figure 3.5 (a) it is found that the magnitude of the gap in this case is approximately 6.7 meV. This value is unusually large given the low T_c (> 8 K) of the superconducting phase as that points to a dramatically large value

for $\Delta/k_BT_c \sim 10$.

To obtain further insight about the gap feature observed at 1.4 K we have performed temperature dependence of the $(dI/dV)_N$ spectra in the ballistic regime (Figure 3.5(b)). Surprisingly, the position of the peak in $(dI/dV)_N$ does not show significant shift with increasing temperature and the peaks survive up to 13 K beyond which the spectra become flat due to thermal broadening. This observation is strikingly similar to the pseudo-gap feature observed in case of the cuprates where the peaks in $(dI/dV)_N$ representing the pseudogap do not shift with temperature. [54, 55] It should also be noted that although the onset temperature of superconductivity is 6 K, the AR like features are observed up to 13 K. Similar observation was made earlier in the context of the ferro-pnictide [56, 57] and the chalcogenide superconductors. [57] This was attributed to (1) AR originating from pre-formed phase incoherent Cooper pairs [58] in the normal state of epitaxial thin films of ferropnictide superconductors [56] and (2) a novel phase of matter not related to superconductivity in the normal state of the iron chalcogenide superconductors. [57] However, in the second case the spectral features exhibited a systematic temperature dependence unlike what we observe here.

3.3.2 Concave curvature of $H - T$ phase diagram

Further investigate the superconducting nature of the point contacts we have constructed the $H-T$ phase diagram (Figure 3.6(b)). [17] As it is seen in Figure 3.6(a), for a given point contact, T_c decreases with increasing magnetic field. The transition becomes less clear above a magnetic field of 4.8 Tesla. We note that the critical field of a superconducting point contact can be significantly different from the critical field of the bulk superconductor itself. [59]

In Figure 3.6(b), we also show the empirical prediction for the $H - T$ phase diagram as a dashed line for a conventional superconductor. An approximate extrapolation of the empirical $H - T$ curve indicates a critical field as high as 14 T

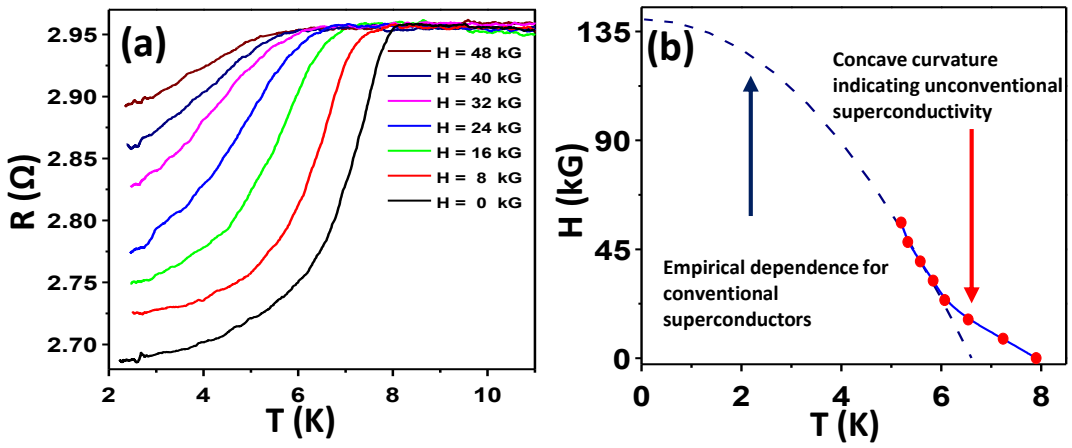

Figure 3.6: (a) Magnetic field dependence of the $R-T$ for a point-contact in thermal regime of transport. (b) The $H-T$ phase diagram. The dotted line shows the empirical prediction for a conventional superconductor. The red dots are the data points extracted from the graphs in (a).

for the given point contact. The deviation of the measured data from the empirical prediction at higher temperature with a concave curvature could be an indication of unconventional superconductivity. [17] However, the concave curvature in the $H-T$ phase diagram alone does not prove the existence of unconventional pairing. In fact, the intrinsic disorder induced by the point contact might also cause a concave curvature.

3.3.3 Zero Bias Conductance Peak (ZBCP)

In order to investigate the relation of this gap with superconductivity, we have probed the magnetic field dependence of the spectra obtained on a point-contact in the ballistic regime (Figure 3.7). The gap features show systematic dependence on magnetic field and the extrapolation of this dependence indicates that the gap feature vanishes around 45 kG. Therefore, it is confirmed that in this case the pseudogap is a precursor phase to the superconducting state.

All the spectra obtained in the ballistic regime also show a peak structure in $(dI/dV)_N$ at $V=0$. When the over-all signal is large, this structure is clearly visible. As shown in Figure 3.7, for certain point-contacts, this zero-bias conductance peak (ZBCP) is pronounced. Such a ZBCP is commonly seen for *ab*-plane tunneling in *d*-wave superconductors where it is attributed to the existence of zero energy

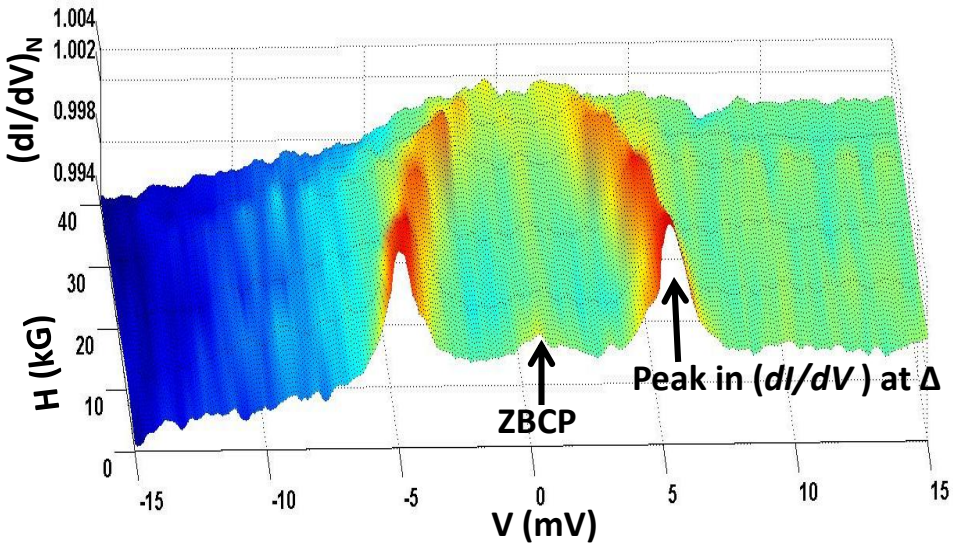

Figure 3.7: Magnetic field dependence a spectrum in the ballistic regime showing the evolution of the gap feature as well as a prominent ZBCP with magnetic field.

Andreev Bound states (ABS). [60] Such unique magnetic field dependence hints to the existence of Andreev bound states (ABS) due to a possible p-wave component in the order parameter symmetry of the new superconducting phase. [61] From the magnetic field dependence it is seen that the ABS is robust and survives up to a high magnetic field. Since the superconducting phase has been derived from a topologically non-trivial system, the robustness against applied large magnetic field might also indicate the existence of time-reversal-invariant Majorana edge-modes in the Cd_3As_2 point-contacts. [62, 63] In fact, such a ZBCP with similar magnetic field dependence was earlier observed in the topological superconductor $Cu_xBi_2Se_3$, where the ZBCP was attributed to the existence of Majorana Fermions. [64–66]

3.3.4 Order parameter symmetry

From the general shape of the dV/dI spectra it is clear that the intermediate regime data has contribution from both AR and critical current. In order to confirm the existence of the AR contribution, we have differentiated the expression of current ($I_{ballistic}$) with respect to V and compared the same with the experimental data. The representative fittings with the fitting parameters are shown in figure 3.8. The data obtained in the ballistic regime are significantly broader than the BTK prediction.

This is because in the ballistic regime the inelastic scattering processes are forbidden and therefore, the features associated with unconventional component of the order parameter are prominent.

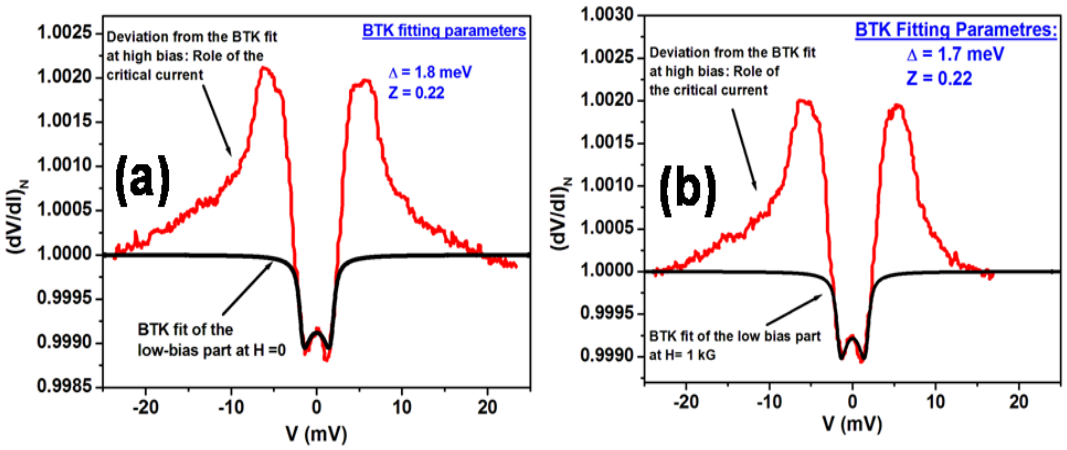

Figure 3.8: Two Ag-Cd_3As_2 point-contact spectra obtained at different magnetic fields in the intermediate regime with low-bias BTK fits.

The fact that we could fit the low-bias part of the spectrum with BTK theory also confirms that the order parameter symmetry in the new superconducting phase is a mixed angular momentum symmetry with a strong s-wave component. From the analysis and discussion regarding the observed ZBCP presented in the main text there is a strong indication that a $s + p$-wave type of symmetry is possible in this new superconducting phase. [67]

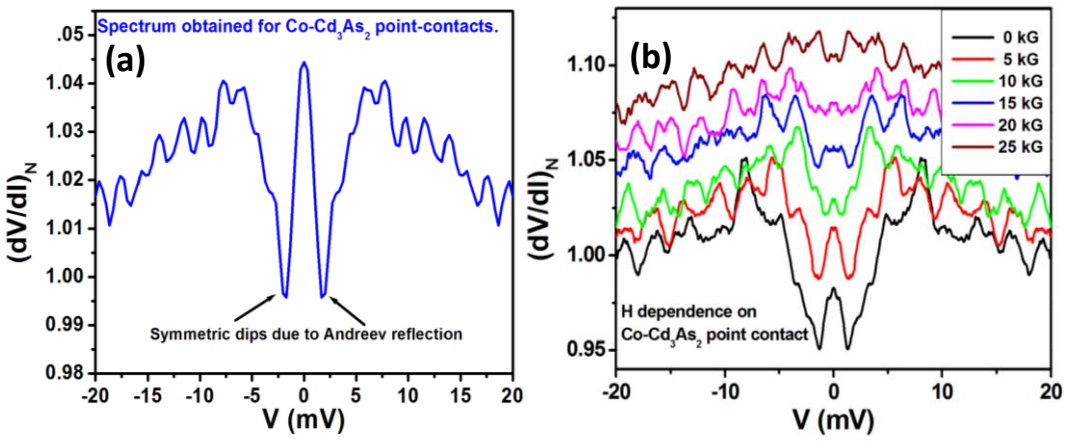

Figure 3.9: (a) A dV/dI_N spectrum obtained from a Co-Cd_3As_2 point-contact. (b)Magnetic field dependence of another spectrum.

The possible p-wave contribution is further supported by our experiments on

the point-contacts made with a spin-polarized metal (Cobalt) where the AR related features are clearly visible (as in figure 3.9) indicating that the superconducting properties are not strongly suppressed by the proximity of a metal with spin-polarized Fermi-surface. Moreover, the superconductivity related features for the Co-Cd_3As_2 point-contacts survived up to a high magnetic field of 25 kG.

3.3.5 ZBCP and splitting in Cd_3As_2

The investigation of the complex superconducting phases, particularly in the newly discovered topologically nontrivial systems have raised the possibility of exploring the topological superconducting phase that are expected to host some of the most elusive particles predicted in quantum field theory, the Majorana fermions [68, 69]. Discovery of superconducting phase in topological non-trivial 3D Dirac semimetal, Cd_3As_2 [70–72], where the material itself does not show superconductivity but under nano-meter scale interfaces between normal metals and Cd_3As_2 become superconducting with unconventional pairing interactions. [73] Since from theoretical perspective significant progress has been made in understanding the possible "smoking gun" signature of Majorana modes that might emerge at the interfaces between a known *s*-wave superconductor and a high spin-orbit coupling semiconductor [74–86]. The investigation of such mode we have performed point contact spectroscopy on Cd_3As_2 with sharp tips of Nb, a conventional *s*-wave superconductor.

3.3.5.1 Point-contact spectroscopy in different transport regimes using Nb tip: Figure 3.10 (a) shows a typical point-contact spectrum obtained between a non-superconducting elemental metal like silver (Ag) and Cd_3As_2. The two peaks symmetric about $V = 0$ in this spectrum appear due to AR between the normal metal and a superconducting phase that is induced at the point of contact and the position of the peaks gives an approximate estimate of the superconducting energy gap which in this case was $\sim 5.5\, meV$. A tiny zero-bias conductance peak (ZBCP)

is also observed in the spectrum.

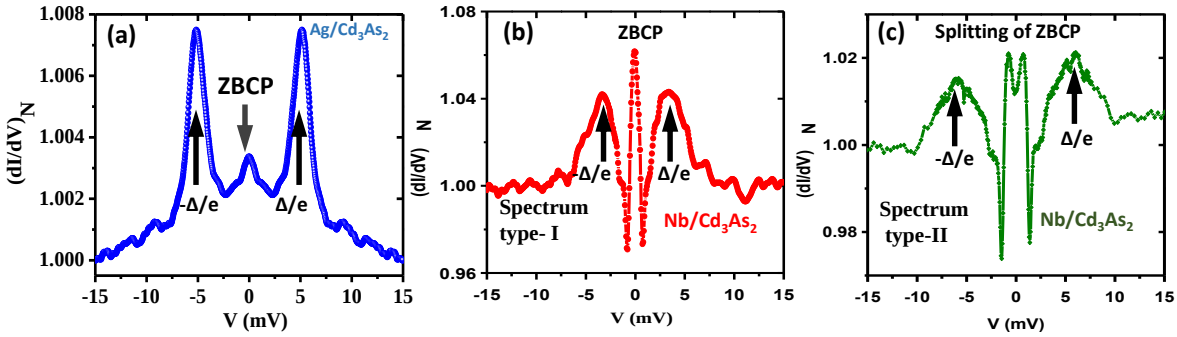

Figure 3.10: (a) Ag/Cd_3As_2 point-contact showing a zero-bias conductance peak (ZBCP) along with two sharp peaks corresponding to the induced superconducting gap voltage. (b) Nb/Cd_3As_2 point-contact showing a very prominent ZBCP without splitting — we call this type-I spectrum. (c) For a different barrier strength the ZBCP shows splitting — we call this type-II spectrum.

In figure 3.10 (b) we show a spectrum obtained from an Nb/Cd_3As_2 point contact with a normal state (high-bias) contact resistance of 2 Ω. The spectrum shows the superconducting gap structures at $\Delta = \pm 5.5\, meV$ respectively, as it was seen for Ag/Cd_3As_2 point contacts as shown in figure 3.10 (a). However, in contrast to figure 3.10 (a), the spectrum presented in figure 3.10 (b) shows a remarkably sharper ZBCP. When the point contact is physically changed in order to achieve a different effective interfacial barrier (Z, as defined in the BTK theory), the ZBCP spontaneously splits into two peaks symmetric about $V = 0$ (See Figure 3.10 (c)). For all the experiments presented here, the Nb tips were made out of $0.25\, mm$ dia. wires of pure (99.999%) Nb which shows a superconducting critical temperature of 9.1 K and a gap of $1.2\, meV$. It should be noted that the spectra for Nb/Cd_3As_2 point contacts are broader than the spectra for Ag/Cd_3As_2 point contacts. This can be attributed to the fact that the s-wave gap of Nb mixes non-trivially with the unconventional gap of Cd_3As_2 and the AR feature associated with Nb is hidden in the broadened spectra.

3.3.5.2 Magnetic field and temperature dependence: In order to find out whether the zero-bias conductance peak is associated with the superconductivity of the point contacts, we have performed magnetic field dependence of both types of

spectra. The systematic magnetic field dependent data are presented in figure 3.11. Both types of spectra, type I and type II evolve smoothly with magnetic field.

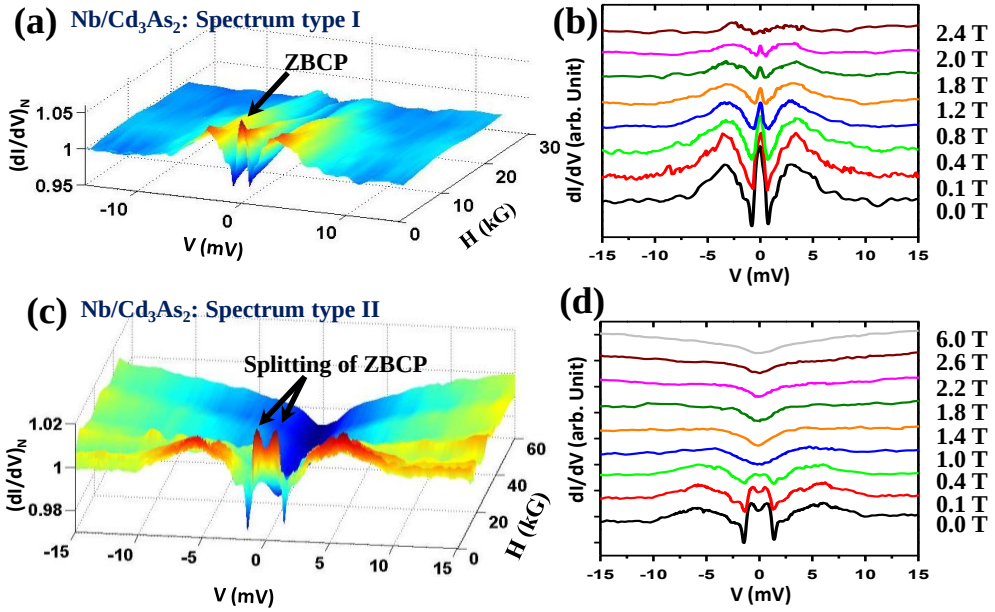

Figure 3.11: (a),(b) Magnetic field dependence of type-I spectra for Nb/Cd_3As_2 point-contact in 3-D and 2-D respectively. (c),(d) Magnetic field dependence of type-II spectra for Nb/Cd_3As_2 point-contact in 3-D and 2-D respectively. The point-contact spectra showing disappearance of a ZBCP and splitting of the ZBCP with stronger magnetic field.

The spectra of type I lose the prominent spectral features namely the induced gap structure at 5 meV and the single ZBCP at a magnetic field of 2.4 Tesla (figure 3.11 (a), figure 3.11 (b)). It should be noted that the ZBCP disappears at the same magnetic field where the induced superconducting gap structure disappears.

Therefore, it can be concluded that the observed ZBCP is related to superconductivity. In fact, a similar magnetic field dependence of the ZBCP was seen with non-superconducting tips. The spectra of type II that show the splitting of the ZBCP also show a systematic evolution with increasing magnetic field. The double peak structure gives rise to a single peak at 0.4 Tesla which further evolves to become a single dip at 1.0 Tesla. The dip structure, along with the induced gap structure at higher bias, almost disappears at a high magnetic field of 6 Tesla. The difference in the magnitude of fields at which the spectral features disappear for the spectra of type I and of type II further confirm that the nature of the point contacts in the two cases are significantly different. The observed difference in magnetic field depen-

dence for the two different point contacts is consistent with the expected variation in superconducting point contacts.

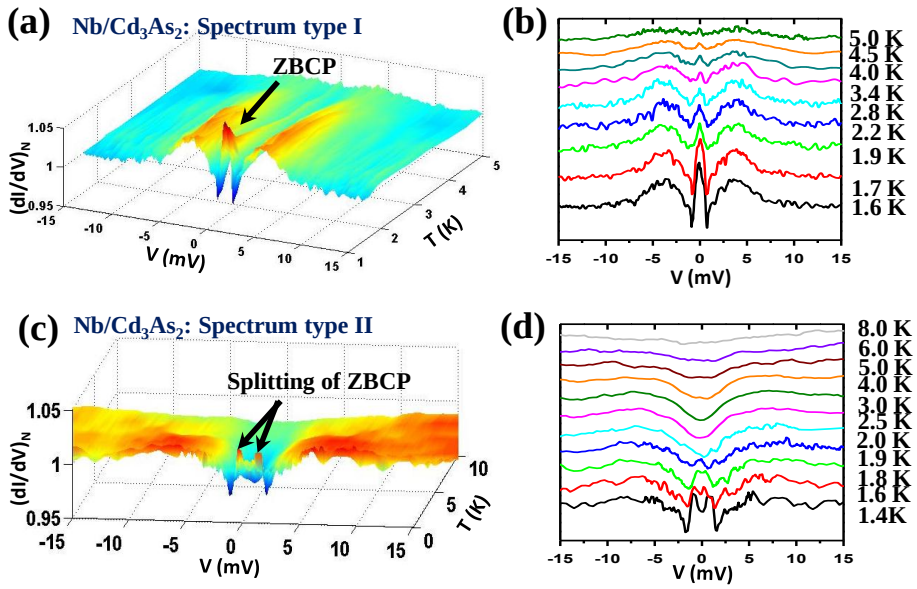

Figure 3.12: (a),(b) Temperature dependence of type-I spectra for Nb/Cd_3As_2 point-contact in 3-D and 2-D respectively. (c),(d) Temperature dependence of type-II spectra for Nb/Cd_3As_2 point-contact in 3-D and 2-D respectively. The point-contact spectra showing disappearance of a ZBCP and splitting of the ZBCP with higher temperature.

The relation between the ZBCP and it's splitting can also be confirmed from the temperature dependence of the AR spectra of type I and type II (Figure 3.12). All the spectral features evolve systematically with increasing temperature and the ZBCP disappears at the same temperature where the superconducting gap structure also disappears. It may be noted that the critical temperature of the point contacts vary slightly between the spectra of type I and of type II possibly due to the difference in the point contact geometry and the transparency of the point contacts.

In addition to that, the difference in spectral features in the two types of spectra (i.e. type-I and type-II) that we have presented above attributed to the difference in Z. This is reasonable because, in general, for a given combination of a tip and a sample, for different point contacts, Z is the parameter that changes most significantly from one-point contact to another. Statistically, the two types of spectra for Nb/Cd3As2 point contacts have been observed with equal likelihood for a large

number of point contacts. No other types of spectra could be recorded without driving the point contacts sufficiently away from the ballistic regime.

In conclusion, our experiments show an indication of an unconventional order parameter on Cd_3As_2/Ag point-contacts. The claim of unconventional component of the order parameter is based on several facts:

(a) Observation of a non-BCS like temperature dependence of the superconducting energy gap (as shown in Figure 3.5 (b)).

(b) The AR peaks are significantly broader than what is expected within conventional BTK theory (as shown in Figure 3.5 (a)).

(c) Emergence of a ZBCP (as shown in Figure 3.7).

While the above three points confirm the unconventional nature of superconductivity, our speculation of a p-wave component is based on the observation of ZBCP alone. It is understood that ZBCP is not a conclusive evidence of p-wave superconductivity. Furthermore, in Nb/Cd_3As_2 point contacts we observe a ZBCP which shows splitting when the barrier at the interface is tuned by physically changing the point contact. This observation is also consistent with a p-wave scenario. [61,64–66]

(d) Existence of robust magnetic field dependence ZBCP data and strong Andreev reflection signature using ferromagnetic tip of cobalt, there might be existence of p-wave component of order parameter. But we do not claim on p-wave pairing symmetry and Majorana modes on the basis of observed ZBCP with splitting or no splitting as shown in figures 3.10 and 3.11 with Nb tip. There are also other factors which might be responsible for the occurrence of ZBCP with splitting or no splitting (in the two types of spectra i.e. type-I and type-II) 1) level of disorder over the sample 2) shape and size of the contact diameter 3) interfacial barrier strength (Z). These parameters change from one-point contact to another randomly due to which there are two types of spectra have been observed for Nb/Cd_3As_2 point-contacts. Further, in order to comment on the height and width of the ZBC peaks which are no doubt too weak and wide, we believe that because of thermal broadening the

peaks become too wide. Therefore, there can not be given any conclusive remark on the basis of the height and width of these ZBCP.

We have also performed measurements with tips made of two other pure metals like platinum (Pt) and Gold (Au). The point-contacts on Cd_3As_2 with Pt and Au also show superconductivity with similar properties as with Ag. The relevant data with Au and Pt are presented in the Appendix. In order to understand how the local exotic superconducting phase might emerge here it is important to investigate the key features of the complex band structure of Cd_3As_2. From first-principle calculations it was shown that Cd_3As_2 is a symmetry-protected topological semi-metal. The bulk has a pair of three dimensional Dirac points in the Fermi level and there are Fermi arcs on the surfaces. [49] In this context it was also proposed that by certain symmetry breaking Cd_3As_2 can be driven into topologically distinct phases like a Weyl semimetal, a topological insulator or a topological superconductor. In our case we believe that the point-contacts formed on the surface of Cd_3As_2 might be driven into a superconducting phase through two possible mechanisms: (a) The metallic tip acts like a local dopant that might modify the local carrier concentration in a way so as to favor local superconductivity [43](b) the point-contact alters the local band structure underneath the tip by physically altering the local crystal structure and lowering the symmetry. This symmetry lowering effect might help stabilizing a local superconducting phase. [87] However, concrete theoretical investigation will be required to establish the origin of this superconducting phase.

3.4 Appendix

3.4.1 Measurements with Pt and Au Tips

In order to investigate whether the new superconducting phase emerges only in a point-contact with silver (Ag) tip, we have performed measurements with platinum (Pt) and gold (Au) tips as well. It is observed that for all metallic tips the superconducting phase emerges. The data obtained between Cd3As2 and Pt and Au tips are shown in figure A3.1.

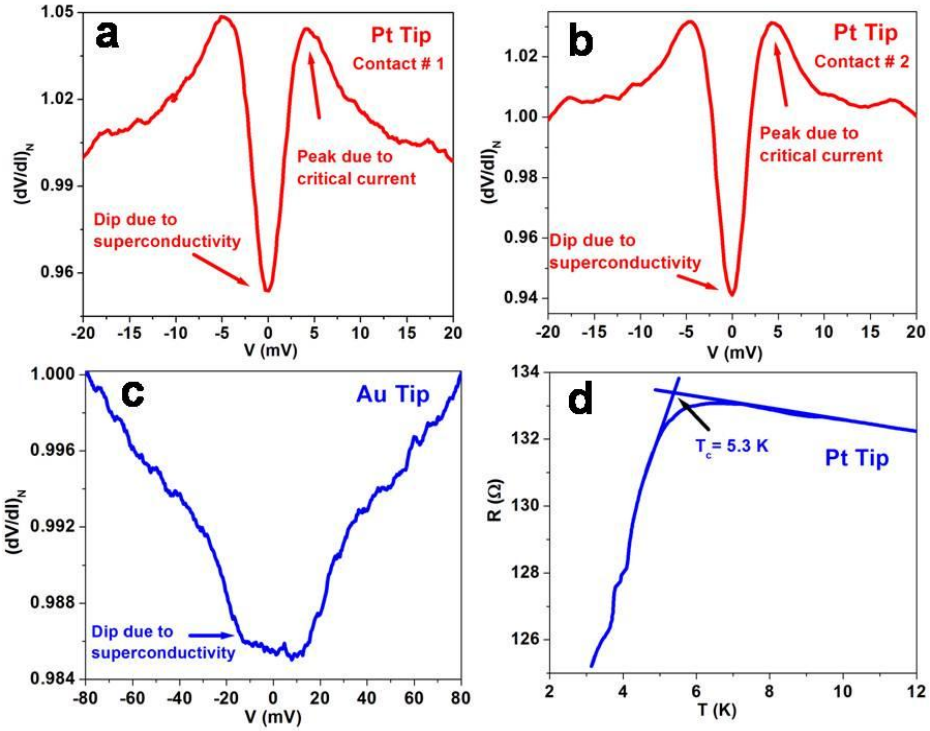

Figure A3.1: (a) and (b) showing representative spectra with superconducting dips that were obtained from two different point-contacts on Cd3As2 with a Pt tip. (c) A spectrum obtained with Au tip. This spectrum also shows the signature of the gap structure. (d) $R-T$ data of the point-contact shown in (a). The superconducting transition is clearly seen at 5.3 K.

3.4.2 Material Synthesis

Polycrystalline samples of Cd_3As_2 were obtained by heating the stoichiometric mixture of the constituent elements. A mixture of Cd and As powder ($\sim$ 1 gram) was sealed in an evacuated quartz tube ($\sim 10^{-5}$ mbar), heated at 500^0C for 8 hours, then at 850^0C for 24 hours with a typical ramping rate of 1^0C/min and furnace

cooled to room temperature. The shiny black crystalline product thus obtained was ground well, palletized (ϕ = 8 mm) and heated again in vacuum at 400^0C for 6 h for homogenization. The pellet was shiny black and hard in nature.

3.4.3 Characterization

3.4.3.1 X-ray diffraction: The samples were characterized by powder X-ray diffraction technique using Cu-Kα radiation (λ = 1.5406) on a Bruker D8 Advance diffractometer. All the peaks could be indexed on the basis of a centrosymmetric tetragonal cell in $I4_1/acd$ space group as reported by Cava *et al.* [88] The sample was pure with no apparent impurity phase present in the resolution limit of X-ray diffraction analysis. Lattice parameters calculated using *Le'Bail* method were in close agreement with the literature values (figure A3.2). It shows the *Le'Bail* fit to the powder x-ray diffraction pattern of polycrystalline Cd_3As_2. The vertical bars indicate the allowed Bragg reflections.

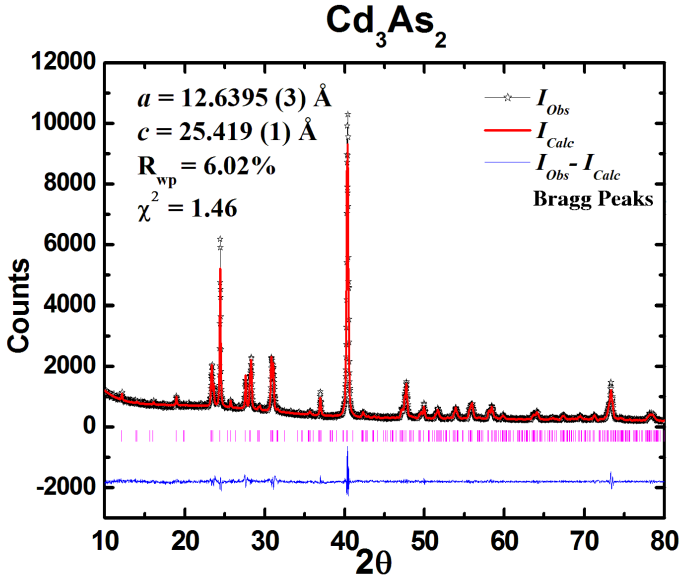

Figure A3.2: Powder x-ray diffraction pattern of polycrystalline Cd_3As_2 fitted with *Le'Bail*. The vertical bars indicate the allowed Bragg reflections.

3.4.3.2 Energy dispersive X-ray analysis (EDAX): Compositional analysis was done using a SEM-EDAX. The average stoichiometry found after collecting data on each sample at many different regions was close to 3:2 (Cd:As). There were

some regions were As was slightly deficient (5%). Figure A3.3 shows the presence of Cd and As. C and Si comes from the carbon tape and detector respectively. Inset of figure A3.3 shows a typical electron image of the polished pellet on which measurements were performed.

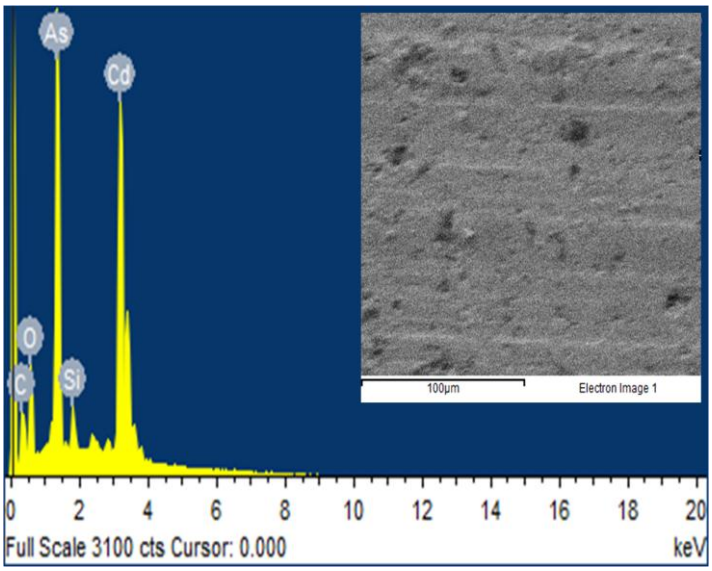

Figure A3.3: EDAX spectrum of Cd_3As_2. The inset shows image of polished pellet of Cd_3As_2.

3.4.3.3 Magnetization of the bulk Cd_3As_2 samples: The VSM (Vibrating Sample Magnetometer) experiment was done to investigate the possibility of hidden bulk superconducting phase in the material. The measurement was done in a Quantum Design (QD) PPMS (Physical properties measurement system) with a VSM probe supplied by QD. The measurement field was 100 Oe. The magnetization does not show any diamagnetic transition down to 2 K.

3.4.3.4 Four-probe resistivity of bulk Cd_3As_2 samples: Resistivity of the samples that were used for the point-contact spectroscopy measurements were measured by a four-probe technique in a Quantum Design PPMS. The resistivity as a function of temperature of three such samples is presented in figure A3.5. The samples show semi-metallic behavior with varying mobility. This further confirms that no superconducting phase is present in the bulk.

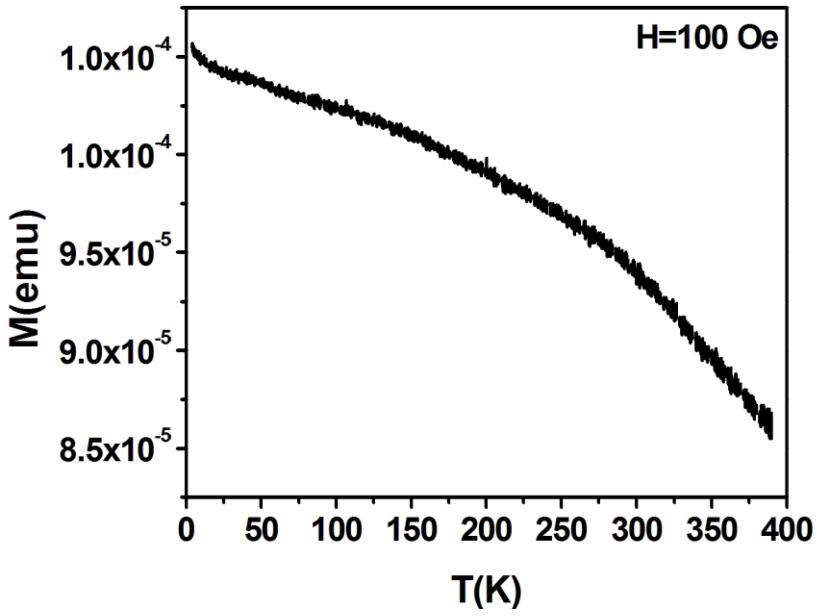

figure A3.4: Magnetization vs. temperature of the bulk sample measured in a VSM in a Quantum Design PPMS. The bulk sample does not show any diamagnetic transition at low temperature dov

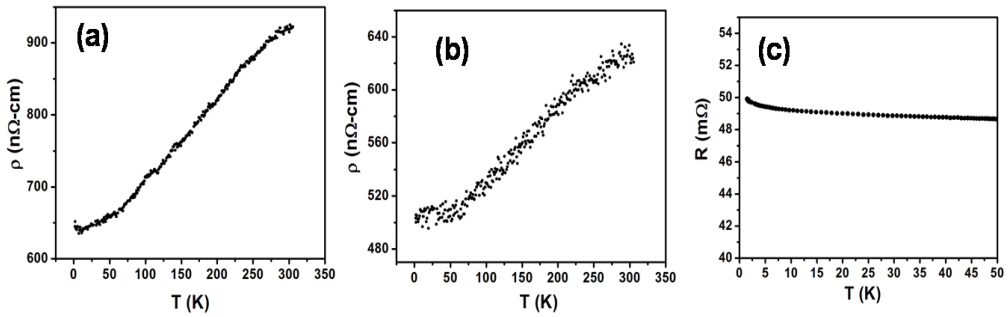

figure A3.5: Raw data for four probe resistance vs. temperature of three bulk Cd_3As_2 samples with varying mobility. All three of them lead to the new superconducting phase in a point-contact geometry.

3.4.4 How did we determine the critical temperature (T_c)?

For all the point-contacts reported here we have measured the temperature (T) dependence of the point-contact resistance (R) with $V = 0$. The $R-T$ data show a broad transition to the superconducting state. We have drawn the slope of the $R-T$ curves above and below the onset of transitions. The temperature at which the two slopes for a given $R-T$ curve meet has been taken as the T_c for the corresponding point-contacts. It is important to note that for the ballistic point-contacts we cannot measure the T_c as for such point-contacts the contact-resistance depends only on fundamental constants and remain temperature independent. However, from the

thermal limit point-contacts we learn that the T_c does not have a strong dependence on contact size for a given sample and therefore it is rational to conclude that for the ballistic point-contacts T_c remains close to 6 K. However, for the samples with higher mobility, the highest critical temperature that we have measured is slightly higher (8 K).

3.4.5 Size of the point-contacts

The point-contact spectroscopy measurements were done at different points on two samples grown in two different batches. The contact size was estimated from the normal state resistance (at high V) following Wexler's formula given by equation (1) in the first chapter. Where, $\Gamma(l/a)$ is a numerical factor close to unity. a is the contact diameter and $2h/e^2$ is quantum resistance i.e. $50k\Omega$. k_F is the magnitude of the Fermi wave vector which is 0.04 Åfor Cd_3As_2 and $\rho(T)$ is resistivity at temperature T(in K). $\rho(1.5) = 28\mu\Omega - \text{cm}$ for Cd_3As_2 (measured by conventional four-probe method). However, if we calculate the contact diameter by taking resistivity 650 n-ohm cm (as shown in figure A3.5 (a)) which is 50 times smaller than the 28 micro-Ohm cm as mentioned in figure A3.6, the order of magnitude of contact diameter does not change much. In fact, point–contact diameter further decreases by few nanometers.

In our case where we do measurements under metallic point-contacts, where the contact size is of the order of 100 nm. In such a large area, the effect of atomic scale disorders get averaged out. This is unlike in case of STM where the size scale is of the order of atomic length scales. This point has been mentioned in the thesis. We have ruled out the possibility of larger size disorders like clustering of elements etc. by our characterization of samples.

Point-contact No.	**Point-contact Resistance (R_{PC}) Ω**	**Contact Diameter (a) nm**
1	22	121
2	2.6	371
3	122	51
4	22	121
5	2.5	380
6	209	39
7	24	116
8	24	116
9	17.7	136
10	1.8	448
11	3.1	338
12	6.3	232
13	21	123
14	9	194

Figure A3.6: A representative list of the normal state resistance and size of the point-contacts.

4 TISC in the Weyl Semimetal TaAs

The discovery of Weyl semimetals [3, 4, 89–97] facilitated the realization of Weyl fermions in condensed matter systems after more than 80 years of their theoretical discovery. [98] In quantum field theory, the Weyl fermions [99] were first shown by Hermann Weyl to emerge as solutions to the relativistic Dirac equation. [89, 96] However, until the discovery of TaAs as a Weyl semimetal [89,90,92–96], such exotic particles remained elusive in nature. The Weyl semimetals are topologically non-trivial and are known to demonstrate exotic quantum phenomena and unique surface states. [100] The band structure of a Weyl semimetal involves Weyl nodes, which can be imagined as a monopole or an antimonopole of the Berry curvature in the momentum space. [93,101] Each of the Weyl nodes are associated with a quantized chiral charge and the Weyl nodes are connected with each other only through the boundary of the crystals via Fermi arcs, the characterizing topological surface states in a Weyl semimetal. [89, 92, 93, 96, 102] Recently it was shown that the Fermi arcs in the Weyl semimetal TaAs are highly spin polarized which lie in a completely 2D plane on the surface of the crystal. [103] As a consequence of such exotic topological properties, the Weyl semimetals are believed to host even richer set of physical phenomena that must be explored for better understanding of quantum mechanics and for potential device applications.

We have performed PCS at mesoscopic point contacts between elemental normal metals and high quality single crystals of the Weyl semimetal TaAs.

4.1 Point contact spectroscopy in different transport regimes on TaAs

As we have discussed before, since a tip-induced superconducting (TISC) phase emerges only under point contacts, the traditional bulk characterization tools for characterizing superconducting phases fail to detect TISC. However, by performing

point contact spectroscopy of such point contacts it is possible to explore different regimes of mesoscopic transport where the expected spectral features for superconducting point contacts are well understood. Such experiments can reveal mesoscopic superconducting phases like a TISC that emerge only under point contacts on exotic materials. [73, 104] Furthermore, by driving the point contacts to the ballistic/diffusive regime of transport, it is also possible to extract spectroscopic information of the superconducting phase. [105]

In figure 4.1 (a) we show a point contact spectrum between silver (Ag) and the crystal. The spectrum shows two conductance dips and a zero-bias conductance peak. Such spectra are usually seen for superconducting point contacts in the thermal regime of transport where critical current dominated effects give rise to the conductance dips. [105, 106] In order to further confirm the existence of a TISC, we have measured the magnetic field dependence of the point contact resistance (Figure 4.1 (b)) corresponding to the spectrum presented in figure 4.1 (a). A resistive transition similar to a superconducting transition is clearly seen at $\sim$7.3 K. Moreover, the transition temperature (T_c) systematically goes down with increasing magnetic field, as expected for a superconducting transition. However, though the above data provide sufficient hint to a TISC phase, from the point contact data captured in a single transport regime alone does not confirm the existence of superconductivity unambiguously unless the contact can be also driven to the other regimes of transport where features related to AR must also appear. We have successfully explored these regimes as discussed below.

If the point contact are indeed superconducting, it should be possible to observe characterizing spectroscopic features in two other regimes of mesoscopic transport, namely the intermediate and the ballistic regime. In the intermediate regime, in addition to the critical current dominated conductance dips, two peaks symmetric about $V = 0$, which are known as hallmarks of AR, must also appear. With further reducing the contact size it should be possible to transition to the ballistic/diffusive

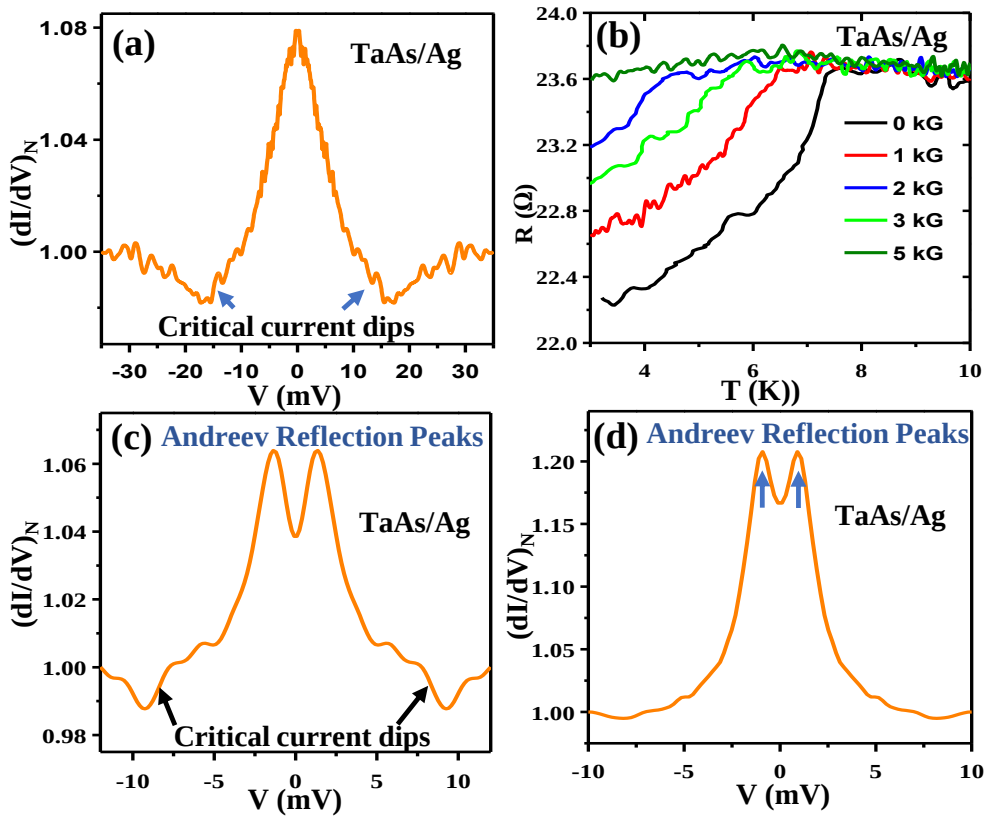

Figure 4.1: (a) A representative TaAs/Ag spectrum obtained in the thermal limit of transport at 1.8 K. (b) H-dependence of point contact $R-T$ showing a transition at 7 K that mimics a superconducting transition. (c) A spectrum obtained in the intermediate regime of transport showing the characteristic signatures of critical current and AR. (d) A ballistic limit experimental spectrum showing only Andreev refection peaks.

regime where the critical current driven dips should disappear and only the double peak feature associated with Andreev refection must remain. [73, 105] We have explored these two regimes and observed the expected features for superconducting point contacts successfully. In Figure 4.1(c) we illustrate a representative spectrum on TaAs in the intermediate regime showing signatures of both critical current and AR. In Figure 4.1(d) we present a representative ballistic regime spectrum where only the two-peak structure symmetric about $V = 0$ due to AR survive and the dips due to critical current disappear. [33, 106] From the observations made above it can be concluded that the point contacts on TaAs made with Ag tips are superconducting, though TaAs is not a superconductor. Hence the data presented above lead to the discovery of a new TISC phase on a Weyl semimetal TaAs.

4.2 Temperature and magnetic field dependence

In order to understand the nature of this new superconducting phase we concentrate on the temperature and the magnetic field dependence of the ballistic regime spectra presented in figure 4.2 (a) and figure 4.2 (b) respectively. The dotted lines show the experimental data points and the solid lines show the fits within the modified BTK model mentioned above. The remarkable match between the experimental

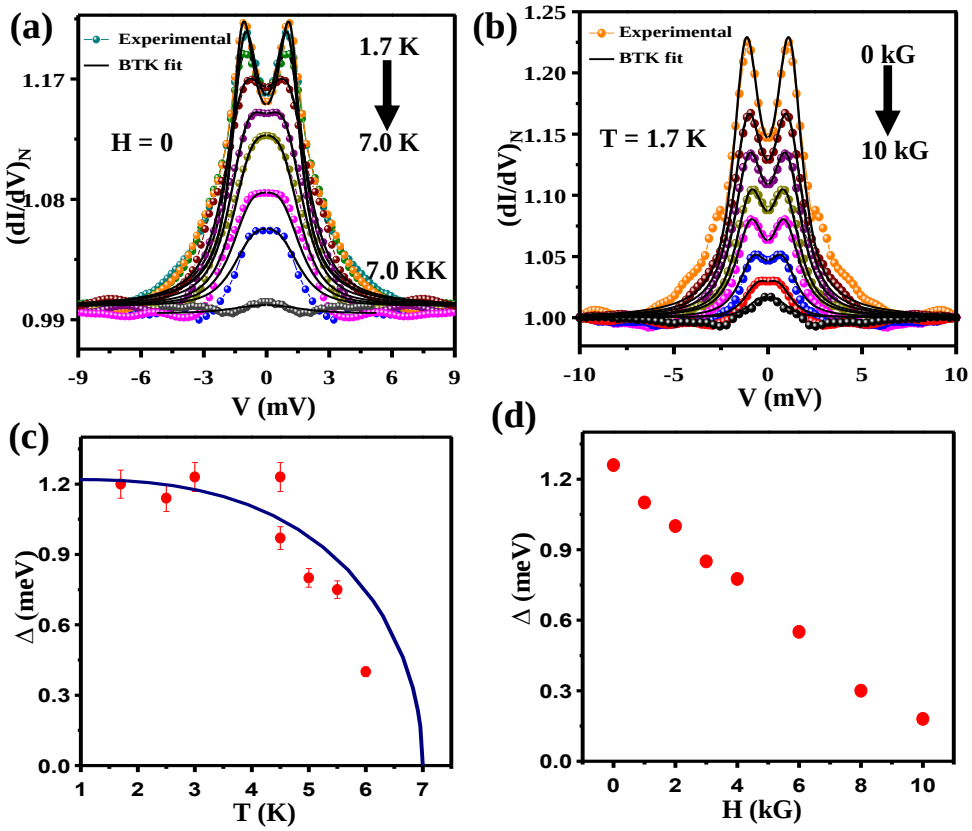

Figure 4.2: (a) Temperature dependence of the ballistic limit spectra (colored dots) and their theoretical fits (solid black lines), (b) Magnetic field dependence of the ballistic limit spectra (colored dots) and their theoretical fits (solid black lines) (c) Temperature dependence of the gap (Δ). The dashed line shows the expected BCS temperature dependence. The error bars depict the range of Δ for which a reasonable fit to the experimental spectra could be obtained. (d) H-dependence of the gap (Δ).

data points and the theoretical fits must be noted here in both the panels. This is surprising because the superconducting phase has been derived from TaAs, which is a complex system, namely a Weyl semimetal. The gap (Δ) *vs.* T curve extracted from the data in figure 4.2 (a) is shown in figure 4.2 (c) where the expected Δ vs. T curve for a BCS superconductor is also shown.

The maximum superconducting energy gap is found to be 1.2 meV which drops systematically with increasing temperature, but does not follow the BCS line. [106, 107] It is clear that the gap disappears at T_c and no pseudogap-like feature above T_c is observed, unlike in Cd_3As_2. [73] While the spectra could be fitted well with the conventional BTK model with spin polarization indicating the possibility of an s-wave component in the order parameter, when the deviation of the temperature dependence of Δ from the BCS and deviation of certain ballistic/diffusive regime spectra from the theoretical fits are considered, the possibility of a mixed angular momentum symmetry of the order parameter where an unconventional component is mixed with a strong s-wave component emerges. [109–111] Also, the possibility of the existence of multiple gaps cannot be ruled out from the set of data presented here. [112] It should be noted that for extracting spectroscopic information we have analysed only the ballistic/diffusive limit spectra where no critical current driven dips were observed and the normal state resistance remained temperature independent.

The gap structure (double conductance peak) is seen to decrease with increasing magnetic field, as expected. Fitting AR spectra could be non-trivial, particularly if the point contact diameter is large enough such that vortices can enter the point contact region. In absence of an exact theory for TISC, it is difficult to estimate the coherence length. Therefore, from the presented data, it is not possible to confirm if vortices enter the point contact region and if multiple vortices can exist there. We have followed the conventional practice and used BTK theory to fit the magnetic field dependent data and found that the field dependent data could be fitted well using the spin-polarized BTK model. A plot of Δ *vs.* H as extracted from the fitting of the spectra as shown in figure 4.2 (d). The critical magnetic field, the field at which Δ vanishes is found to be 10 kG for the point contact presented in figure 4.2 (d).

4.3 Measurement of spin polarization

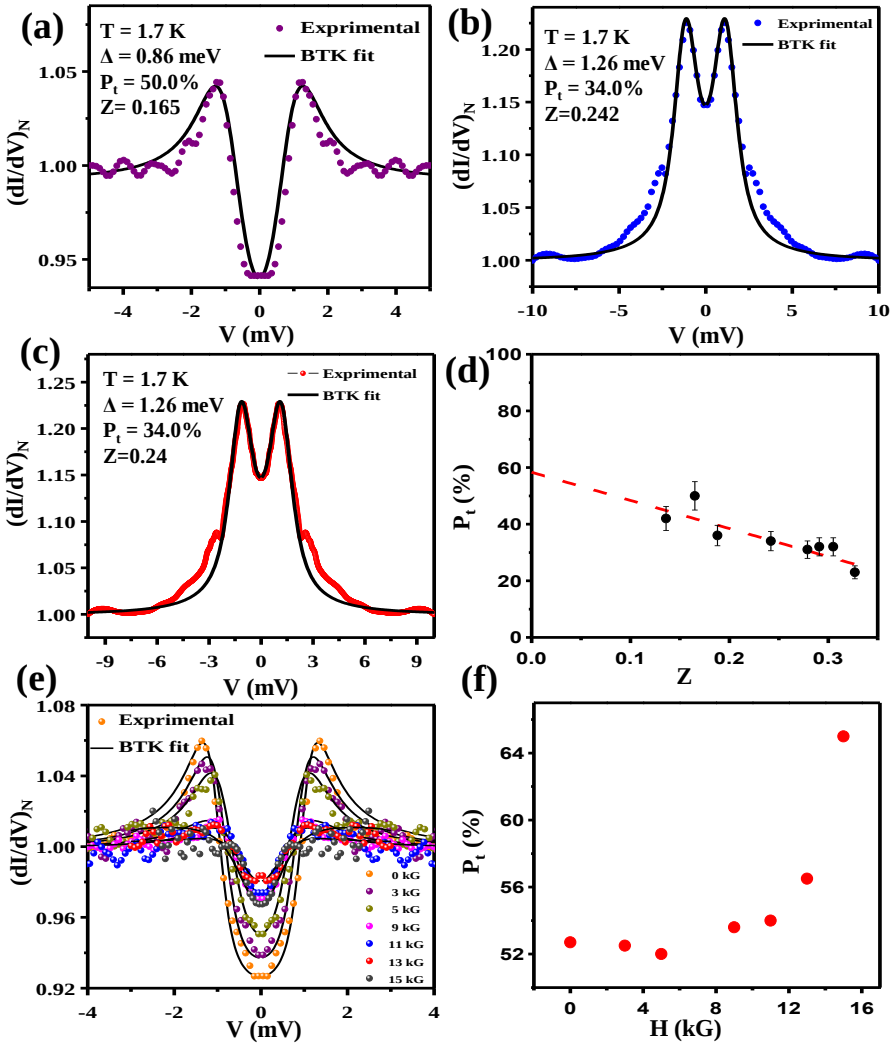

Figure 4.3: (a), (b), (c) Three representing TaAs/Ag spectra (dots) in the ballistic limit and the corresponding theoretical fits (solid lines) showing strong transport spin polarization. (d) Barrier (Z) dependence of spin polarization. A linear extrapolation of this dependence to $Z=0$ shows a large intrinsic transport spin polariation ($\sim$60%). (e) Magnetic field dependence of one of the ballistic point contact spectrum showing the high spin polarization. (f) Magnetic field dependence of spin polarization of the spectrum in (e).

As we mentioned before, in all the ballistic/diffusive limit spectra presented above, a significant suppression of AR was found. [113] Since for TaAs it is known that the surface states are spin polarized, [103] the suppression of AR can be attributed to the existence of spin polarization [33, 35] at the point contacts along with superconductivity. In order to test this effect, we have modified BTK theory to include the effect of spin polarization and the modified formalism yielded remarkably good fitting of the ballistic/diffusive limit point contact spectra with a large

value of transport spin polarization up to 60 %. A set of three representative ballistic/diffusive regime spectra showing high spin polarization are illustrated in Figure 4.3 (a), (b), (c) respectively. The value of the transport spin polarization is seen to decrease with increasing Z as seen in figure 4.3 (d). A linear extrapolation of this curve leads to an intrinsic transport spin polarization of 60%. The measured spin polarization for a finite Z is seen to increase with increasing magnetic field as shown in figure 4.3 (f). The value of spin polarization measured through this technique is lower than the 80 % spin polarization measured by ARPES [103] because point contact spectroscopy is a transport measurement and in this technique the spin polarization of the transport current is measured instead of the absolute value of the spin polarization. [36,114] Nevertheless, the results and the analysis presented above indicate that the super-current flowing through the TaAs point contacts is highly spin polarized.

4.4 Anisotropic magnetoresistance

In order to further confirm the presence of a spin polarized current along with superconductivity at TaAs point contacts, we have performed field-angle dependence of the resistance of a ballistic point contact where the direction of the magnetic field was rotated using a 3-axis vector magnet with respect to the direction of current. The field-angle dependent magnetoresistance data is presented in Figure 4.4 (a). With an applied bias $V = 13\,\mathrm{mV}$ which corresponds to the normal state of the TISC, a large anisotropy in the magnetoresistance is observed which increases with increasing the strength of the magnetic field. This anisotropy in magnetoresistance can be explained if the point contact constriction is assumed to be effectively in the shape of a nano-wire and the magnetic field is rotated with respect to the direction of current flow through the nanowire. Such AMR is also seen for hybrid nanostructures involving materials having surface states with complex spin texture. [115, 116] When the experiment was repeated in the superconducting state ($V = 0.3\,\mathrm{mV}$) of the

TISC as shown in figure 4.4 (b), the anisotropic magnetoresistance (AMR) remained equally noticeable. Therefore, the above observations conclude the co-existence of superconductivity and large spin polarization on TaAs point contacts.

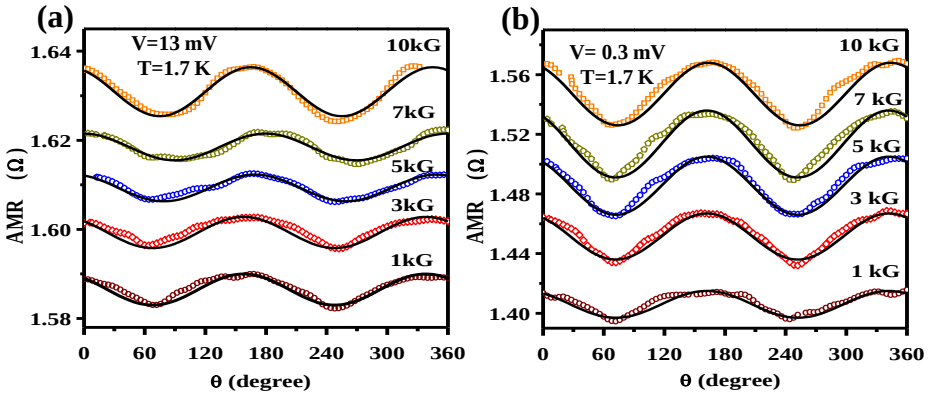

Figure 4.4: Anisotropic magnetoresistance of a point contact in the (a) normal state ($V = 10$ mV) and (b) in the superconducting state ($V = 0.3$ mV). The solid black lines are $cos^2\theta$ fits.

To further confirm that the emergence of AMR is due to the presence of spin polarized current, we have fitted the AMR data using the typical $cos^2\theta$ dependence. The fitting is also shown in Figure 4.4. It should also be noted that since the presented point contacts are either in the ballistic or in the diffusive regimes of transport, where the point contact resistance is predominantly given by Sharvin's resistance which remains to be independent of the bulk resistance of the materials forming a point contact. Therefore, it is reasonable to conclude that the large AMR that we observe here is not due to the bulk TaAs.

The TISC phase presented here might emerge due to a number of reasons including local pressure, local doping and confinement effects. Since the phase could not be realized on a macroscopic interface with metallic silver films deposited on TaAs, and pressure-induced superconductivity is not known on TaAs, we believe that a combination of all the three mechanisms mentioned above could be a possible reason for the emergence of the observed TISC phase. To understand the exact mechanism behind the emergence of a TISC on TaAs, and to determine the exact symmetry of the order parameter, one possible experiment could be to use a low-temperature double-probe scanning tunnelling microscope (STM), where the first

probe will be in contact with the sample to induce TISC and the second probe will perform spectroscopy in the TISC region, very close to the first tip. By moving the second tip away from the first tip while performing spectroscopy at different points, it is also possible to directly measure the length to which TISC extends under a point contact. Such experiments can also probe the possibility of topological and FFLO superconductivity.

Therefore, we have shown the emergence of a tip-induced superconducting (TISC) phase in mesoscopic point contacts between Ag and the Weyl semimetal TaAs through transport and magneto transport measurements at various regimes of mesoscopic transport. We used a modified BTK formalism that includes spin polarization to fit the experimental data which hinted to the coexistence of superconductivity and high transport spin polarization thereby indicating the flow of spin polarized supercurrent through TaAs point contacts. The TISC, though shows the possibility of an unconventional pairing mechanism, no zero-bias conductance peak or a pseudogap could be observed in the ballistic/diffusive limit data. This is in contrast to the earlier observations made on a similar TISC phase on the 3D Dirac semimetal Cd_3As_2. Our observation of the surprising co-existence of superconductivity and high transport spin polarization at TaAs point contacts make the Weyl semimetals particularly interesting for spintronic applications.

4.5 Appendix

4.5.1 Material Synthesis

All the experiments presented in this chapter were carried out on high quality single crystals of TaAs. Here we provide a brief description of sample synthesis which has been presented in detail elsewhere. [118] Single crystals of TaAs were grown via chemical vapour transport. As a first step for polycrystalline material, stoichiometric quantities of Ta (Alfa Aesar, 99.99 %) and As (Chempur, 99.9999 %) were weighed accurately in a quartz ampule, flushed with Ar, sealed under vacuum and heated in two consecutive temperatures of 600° C for 24 hrs and 800° C for 24 hrs, respectively. In the next step for crystal growth, we used microcrystalline powders from step one and then added iodine (7 -8 mg/ml) before sealing the powders in quartz tube. The crystal growth was carried out in a two-zone furnace between 900 to 1050° C for 2 weeks. Here, I_2 act as a transport agent. To obtain high quality of the crystals, temperature gradient is one of the most important parameters and it varies from material to material. We optimized the temperature gradient which is 900° C (source) to 1050° C (sink) for TaAs. The experimental lattice parameters of the TaAs compounds is a = 3.4310(4) Å, c = 11.6252(6) Å,. [119]

4.5.2 Characterization

4.5.2.1 X-ray diffraction: The crystal structure of the TaAs crystal and it's orientation was determined by X-ray diffraction at room temperature. A piece of TaAs single crystal was mounted on a four-circle Rigaku AFC7 X-diffractometer set-up of Mo-Ka ($\lambda = 0.71073\mathring{A}$) radiation with a built-in Saturn 724 CCD detector. The intensity of the obtained reflections were corrected for absorption by using a multi-scan technique. The unit cell was assigned by using a 30 images standard indexing procedure. Here oscillatory images about the crystallographic axes allowed the assignment of the crystal orientation, confirmed the appropriate choice of the

unit cell and showed the excellent crystal quality.

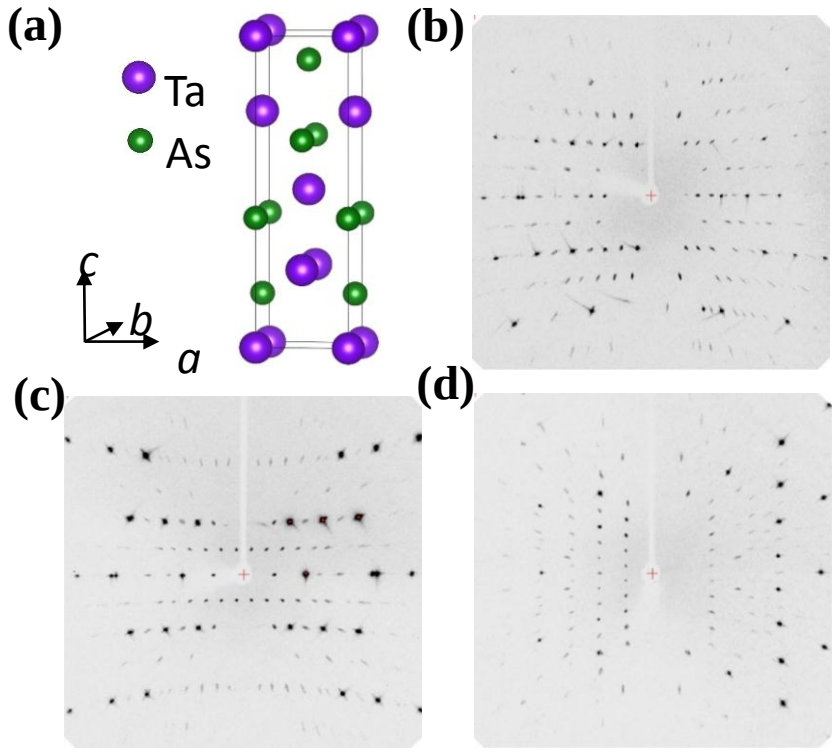

Figure A4.1: **Unit cell and x-ray diffraction of TaAs crystal:** (a) a non-centrosymmetric unit cell of TaAs. (b, (c) and (d), show the rotating x-ray diffraction patterns of the TaAs crystal about the crystallographic a, b, and c-axis respectively. For each case, the rotating axis is vertical.

4.5.2.2 Single crystal X-ray diffraction:

4.5.3 Transport Measurements

Temperature dependent resistivity, ρ (T) of TaAs shows a metal-like behavior in absence of a magnetic field (see figure A4.2 (a)). ρ at 2 K and 300 K are 4 $\mu\Omega$cm and 35 $\mu\Omega$cm, respectively resulting in a residual resistivity ratio of 8.75. When the field is turned on, TaAs shows extremely high magnetoresistance (MR) comprising of Shubnikov de-Haas (SdH) oscillations at low temperatures (see figure A4.2 (b)). The MR values are found to be $1.5 \times 10^5\%$ and $1.7 \times 10^5\%$ at 3 K and 10 K in 90 kG of magnetic field, respectively which slightly vary from 2 K to 25 K. MR is calculated from $MR(\%) = 100 \times (\rho_H - \rho_0)/\rho_0$, where ρ_H and ρ_0 are resistivity in field and 0 field, respectively. After subtracting a cubic polynomial as a background

from the measured data at each temperature, the periodic oscillations in 1/H are visible up to 25 K (see figure A4.2 (c)) and their fast Fourier transform (FFT) correspond to $F_\alpha = 68\,kG$, $F_\beta = 198\,kG$ frequencies (see inset of the figure A4.2 (c)). The quantum oscillation frequency is directly linked to the extremal area of the pocket (AF) by the Onsager relation, $F(=\phi_0/2\pi^2)$, where $\phi_0 = 2.068 \times 10^{-15}\,Wb$. The calculated corresponding area of the Fermi pockets α and β are 0.00065 $\mathring{A}^{-2}$ and 0.0019 $\mathring{A}^{-2}$, which are consistent with the existence of tiny carrier pockets near the Fermi surface [120]. The effective mass is calculated from Lifshitz-Kosevich (LK) relation [121]:

$$\Delta \propto \exp \frac{-14.69 m^* T_D}{H} 14.69 m^* T/H sinh(14.69 m^* T/H)$$

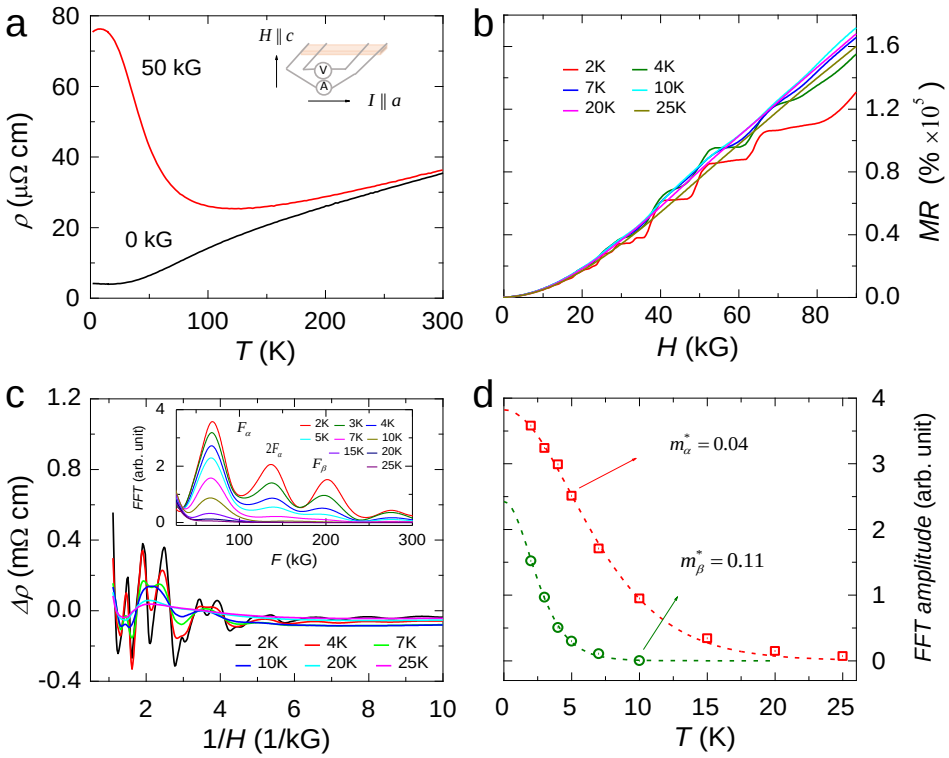

Figure A4.2: **Magneto-resistivity at various temperatures:** (a) temperature dependent resistivity, ρ (T) at 0 field and 50 kG field, (b) magnetoresistance (MR) up to 90 kG at different temperatures. A large amplitude of Shubnikov de-Haas can be seen up to 25 K, (c) (SdH) oscillations after subtracting a cubic polynomial. Fast Fourier transform (FFT) of SdH oscillations mainly gives two frequencies at F_α= 68 kG, F_β = 198 kG (inset). (d) Effective mass corresponding to frequencies F_α and F_β.

where m^* is effective mass, T_D is the Dingle temperature, $H = 18(H = 2/(10 + 1.11))$ kG is average field of taken FFT and m_0 is bare mass of electron. From the above LK formula, the value of m^* can be determined through the fit of the

temperature dependence of the oscillation amplitude (see figure A4.2 (d)). We find the values of $m^*_\alpha = 0.04$ and $m^*_\beta = 0.11$, which are very low and most likely emerged due to the linear-type of dispersion of bands. Further, the Dingle temperature T_{D} is determined to be $\sim 6.3K$ and $\sim 4.8K$, respectively for α and β pockets and corresponding quantum relaxations time, τ_{q} $(= \hbar/(2\pi k_{\mathrm{B}} T_{\mathrm{D}}) = 1.22 \times 10^{-12}/T_{\mathrm{D}})$ are 1.9×10^{-13} s and 2.5×10^{-13} s. Furthermore, measured Hall data together with resistivity show non-linear behavior at all over temperature ranges (2-300 K) evolving the presence of two types of charge carrier which is obvious in a semimetal. After fitting Hall conductivity by two-band model, the carrier density and mobility for electron are found to be $9.1 \times 10^{18} cm^{-3}$ and $0.9 \times 10^5 cm^{22}/Vs$, respectively. Similarly these quantities for hole charge carrier are $8.6 \times 10^{18} cm^{18}$ and $0.7 \times 10^5 cm^2/Vs$. Extremely high MR and mobility, low fields quantum oscillations and low charge carrier density reflect high quality TaAs single crystal.

4.5.4 Fitting parameters of fitted point-contacts spectra

S. No. of Point-Contact	R_{PC} (Ω)	T (K)	Delta (meV)	P (%)	Z	Gamma (Γ)
1	0.39	1.7	1	42	0.136	0.075
2	1.64	1.7	1.1	31	0.279	0.012
3	0.072	1.7	0.8	49.5	0.08	0.006
4	0.93	1.7	1.26	34	0.242	0.001
5	3.01	1.7	0.98	33.3	0.255	0.07
6	0.66	1.7	1.1	36	0.188	0.1
7	0.485	1.7	0.87	23	0.2	0.109
8	0.71	1.7	1	37.8	0.092	0.018
9	0.23	1.7	0.87	44	0.001	0.001
10	0.274	1.7	0.67	28	0.17	0.095
11	0.71	1.7	1.05	32	0.291	0.071
12	0.7	1.7	1	32	0.305	0.06
13	0.85	1.7	0.765	40.2	0.092	0.017

Figure A4.3: Fitting parameters used to fit certain point contacts in the ballistic/diffusive regime.

5 TISC in the nodal Semimetal ZrSiS

Topological systems hosting exotic quasiparticles, like massless Dirac and Weyl fermions, have attained enormous received due to their unusual physical properties. Unlike Dirac and Weyl topological semimetals, some semimetals like ZrSiS, show one dimensional band loops or lines touching each other. [125, 126] One unusual but interesting aspect of ZrSiS in that the range of energy of dispersed bands in ZrSiS is of the order of 2 eV, much larger than the other known Dirac materials [127–129], this makes it a fascinating topological system with various expected anomalous properties some of which have already been observed, like, large magnetoresistance [130] and multiple quantum oscillations existing even at high temperatures [131].

In the previous two chapters, we have discussed a surprising TISC phase in two topological systems—a DSM (Cd_3As_2) [73], a WSM (TaAs) [132]. In this chapter, we show a similar TISC phase on ZrSiS.

ZrSiS single crystals were grown in standard iodine vapor transport method. The polycrystalline powder was prepared in two steps. At first, elemental Si (Strem Chem. 99.999%) and S (Alfa Aesar 99.9995%) were mixed in stoichiometric ratio (1:1) and heated at 1000^oC under vacuum. The resultant powder was mixed with elemental Zr (Alfa Aesar 99.9%) and again heated at 1100^oC. This polycrystalline ZrSiS along with iodine ($5mg/cm^3$) were sealed in a quartz tube under vacuum and kept in a gradient furnace for 72h. During this period, a temperature gradient of 1000^oC was maintained along the quartz tube with hotter end at 1100^oC. Shinny rectangular plate like crystals were obtained at the cooler end. The single crystals have been characterized by High-resolution transmission electron microscopy (HRTEM) and energy-dispersive X-ray (EDX) spectroscopy in a FEI, TECNAI G2 F30, S-TWIN microscope operating at 300 kV. The details of characterization techniques are described in arXive[:1609.09397v2]. [133]

5.1 Point-contact spectroscopy in different transport regimes on ZrSiS

As we have discussed already in chapter 1 (in section 1.2.1 and section 1.2.2.2) that for mesoscopic point contacts, the resistance R_{PC} is given by Wexler's formula [25]. It suggests that when the contact diameter is small compared to electronic mean free path *i.e.*, when the contact is in the so-called ballistic regime, R_S dominates and in the other extreme called the thermal regime, R_M contributes most to R_{PC}. For superconducting point contacts in the thermal regime, as the current through

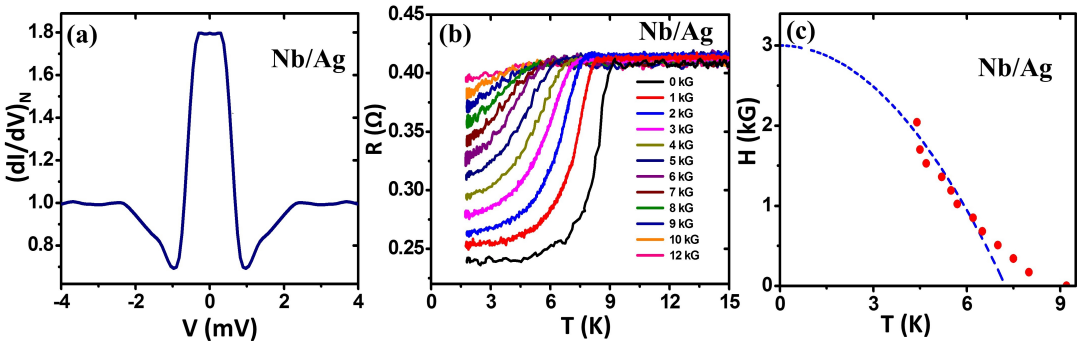

Figure 5.1: (a) A $(dI/dV)_N$ versus V point contact spectrum for a conventional superconductor Nb using Ag tip at 1.8 K in the thermal regime of transport. (b) $R-T$ curves showing systematic drop of the superconducting transition temperature with varying the applied magnetic field. (c) The dotted blue line is $H-T$ phase diagram extracted from $R-T$ curves for a conventional superconductor, Nb. The red line is the expected empirical $H-T$ phase diagram for a conventional superconductor.

a point contact exceeds the critical current (I_c) associated with the point contact, the resistivity (ρ) of the superconducting component of the point contact will be zero leading to a sharp change in R_M. This change leads to a large non-linearity in the $I-V$ characteristic of a thermal regime point contact. In fact, this leads to two sharp dips in the differential conductance dI/dV vs. dc bias (V) spectra. Such dips are seen to be symmetric about $V=0$ and the position of the dips normalized by the normal state resistance of the point contacts provide a direct estimate of the magnitude of I_c.

In order to highlight the points discussed above directly, in figure 5.1 (a), we show a dI/dV spectrum acquired in the thermal regime point contact between a known

conventional superconductor niobium (Nb) and a sharp metallic tip of silver (Ag). The conductance dips symmetric about $V = 0$ are clearly visible. [26] Furthermore, as shown in figure 5.1 (b), the resistance (R) vs. temperature (T) of a superconducting (thermal regime) point contact on Nb shows a sharp change corresponding to the superconducting transition of Nb at 9.2 K. The $R-T$ evolves systematically involving a monotonic decrease in T_c with increasing magnetic field (H).

5.2 Magnetic field and temperature dependence

Now we focus on the data obtained on high quality single crystals of ZrSiS. In figure 5.2 (a) we present the magnetic field dependence of a spectrum obtained on ZrSiS/Ag point contacts. The striking similarity of the zero field data with that

obtained on Nb point contacts must be noted. The conductance dips appearing in the spectrum originates from the critical current of the point contact. All the spectral features show monotonic evolution with increasing magnetic field until all the features smoothly disappear at 20 kG. In order to highlight the superconducting nature of ZrSiS/Ag point contacts, in figure 5.2 (b) we provide the systematic magnetic field dependent data obtained on superconducting Nb/Ag point contacts. The qualitative similarity in the magnetic field dependence of ZrSiS point contacts and Nb point contacts is clear. In figure 5.2 (c) we present the magneto-transport data on ZrSiS/Ag point contacts. The superconducting transition temperature (T_C) is seen to be 7.6 K. This value is remarkably high and comparable to the T_C of the celebrated elemental superconductors like Pb and Nb. The critical temperature decreases monotonically with increasing magnetic field. Again, the zero resistance state cannot be directly measured for reasons discussed before. The $H - T$ phase diagram extracted from this data has been shown in figure 5.2 (d). The blue dotted line in figure 5.2 (d) shows the expected dependence for a conventional superconductor as known empirically. The projected upper critical field of the superconducting

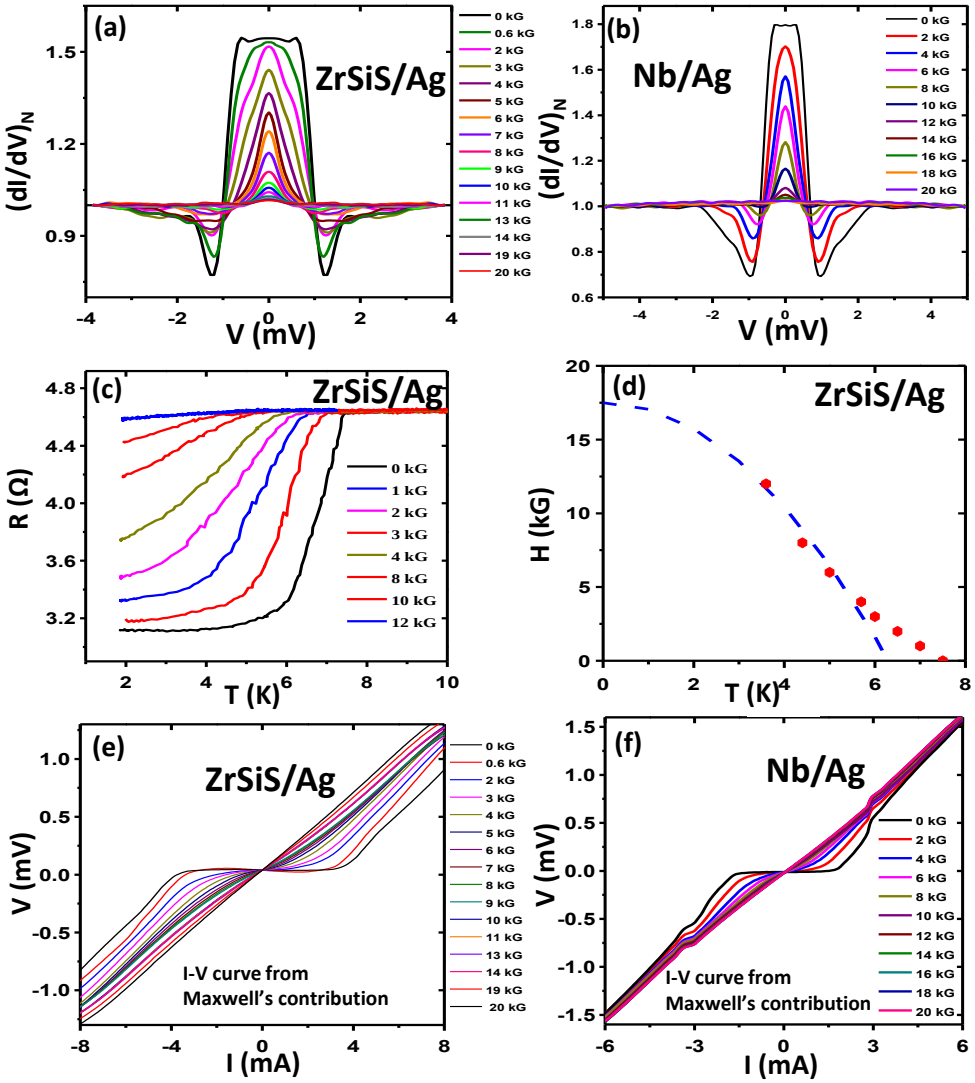

Figure 5.2: (a) Magnetic field dependence spectra in thermal regime on ZrSiS/Ag point-contact. (b) Magnetic field dependence spectra in thermal regime on Nb/Ag point-contact. (c) Magnetic field dependence R-T curves showing disappearance of superconducting transition temperature with increasing magnetic field. (d) The dashes blue line is $H-T$ phase diagram extracted from $R-T$ curves showing in Figure (c). The red line is the expected empirical $H-T$ phase diagram. (e) Evolution of $I-V$ curves with magnetic field for Nb/Ag point-contact with only Maxwell's contribution showing zero resistance part and evolution with magnetic field. (f) Evolution of $I-V$ curves with magnetic field for ZrSiS/Ag point-contact with only Maxwell's contribution showing zero resistance part.

phase could be as high as 17 Tesla and the experimentally measured data points deviate slightly from the empirical expectation. This might be an indication of the existence of an unconventional component in the superconducting phase realized on the topologically non-trivial system ZrSiS.

In order to illustrate the role of critical current on the point contact spectra obtained on ZrSiS, we have used BTK theory [33] to calculate an approximate $I-V$

characteristic associated with the ballistic component (R_S) of the point contact resistance and then subtracted the same from the $I-V$ associated with the total point contact resistance (R_{PC}). The resultant $I-V$ thus obtained is associated with the Maxwell's contribution (R_M) alone (as calculated for Pb/Ag point-contact in the thermal regime of transport in section 1.2.2.2 of chapter 1). The resultant $I-V$ characteristic and the magnetic field dependence of the same has been shown in figure 5.2 (e). This $I-V$ directly reflects the non-linearities associated with the critical current of the superconducting point contact. The smooth decrease of the range over which the voltage remains zero with increasing magnetic field is totally consistent with the magnetic field dependence of a critical current dominated $I-V$ for a superconducting point contact. For comparison, in figure 5.2 (f) we have also provided a similar data extracted from the magnetic field dependent point contact spectra obtained on superconducting Nb (figure 5.2(b)).

In order to provide further support for the superconducting origin of the spectra presented here, we have performed detailed temperature dependence of the spectra. In figure 5.3 (a) we show the temperature dependence. The spectral features disappear at the critical temperature. We have also extracted the temperature evolution of the critical current dominated $I-V$ following the protocol discussed above (figure 5.3 (b)). For comparison, we have also included the temperature dependent data on superconducting Nb point contacts (figure 5.3(c, d)).

Even when a point contact is in the thermal regime of transport, as per Wexler's formula, a small but finite ballistic component exists. From a visual inspection it is clear that between -0.8 meV and +0.8 meV, the zero field spectrum on ZrSiS remains flat. This could be a signature of AR when the barrier potential at the interface is extremely small making the barriers almost transparent. Such an attribution is consistent with the prediction from the theory of Blonder, Tinkham and Klapwijk (BTK) for superconducting point contacts. Going by the arguments provided by BTK, there is a strong indication that the superconducting energy gap (Δ) of the

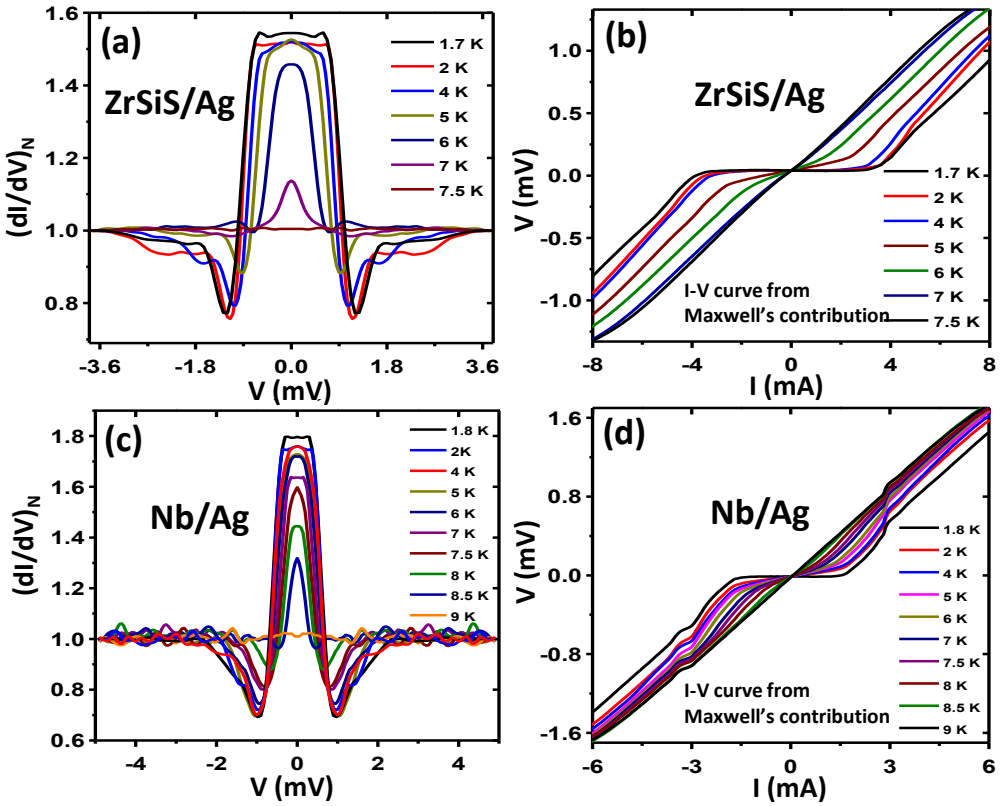

Figure 5.3: (a) Temperature dependence of thermal limit spectra on ZrSiS/Ag point-contact. (b) Evolution of $I-V$ curves with temperature for ZrSiS/Ag point-contact with only Maxwell's contribution showing zero resistance part. (c) Temperature dependence of the thermal limit spectra on Nb/Ag point-contact (d) Evolution of $I-V$ curves with temperature for Nb/Ag point-contact with only Maxwell's contribution showing zero resistance part.

superconducting phase realized on ZrSiS is 0.8 meV. In that case $2\Delta/k_BT_c$ is found to be 2.48. This is consistent with a weak-coupling superconducting phase emerging due to phonon mediated pairing up of electrons. Therefore, it is rational to conclude that the presence of a metallic tip on ZrSiS modifies the electron-phonon coupling strength locally under the point contact, which in turn facilitates the emergence of the observed superconducting phase.

In conclusion, we observed TISC in another novel topological material ZrSiS. [125, 126] The TISC on ZrSiS shows a critical temperature (T_c) of ~ 7.5 K and a superconducting energy gap $\Delta_{(T=0)} \sim 1$ meV. This discovery is particularly important because ZrSiS is known to show a linear band dispersion over a large energy range ~ 2 eV. [127] This is in contrast with most other topological materials for which the band dispersion is usually seen over a few hundred meV from the respective Dirac

points. [128, 129] This makes the topological properties of ZrSiS extremely robust against carrier doping, variation of stoichiometry and other external perturbative effects. This means, when a superconducting phase is realized on ZrSiS point contacts, the topological properties of ZrSiS are not expected to be destroyed merely by the presence of a metallic tip forming the point contacts. Therefore, the superconducting phase realized on ZrSiS does not emerge at the expense of the topological nature of ZrSiS. This makes ZrSiS the most promising candidate for a topological superconductor.

From our studies on several topological systems it is true that most of them undergo a topological phase transition under the tip within the temperature range that is accessible to us. This is the first time that the tip-induced superconductivity is observed in topologically non-trivial materials under the point-contacts where both material as well as tip are non-superconducting in nature but superconducting at point-contact. Therefore, there is no previous work reported on this. However, it may be noted that prior to our first observation of TISC in Cd3As2, there had been theoretical predictions of achieving other phases of matter out of topological materials by external perturbation. [3, 4, 6, 45, 47]

6 Scanning probe microscopy (SPM): Imaging, spectroscopy and domain writing

In addition to the above presented work on low temperature measurements of topological systems. I have also investigated physical properties of semiconductors by scanning probe microscopy at high temperature. In this chapter, we will show such experiments.

Scanning probe microscopy (SPM) experimental techniques under the general category of SPM is one of the powerful techniques to investigate the condensed matter systems even down to sub-atomic length scales with high energy resolution [134–136]. The study of wide variety of systems showing unusual electronic and magnetic properties [134, 137] have extended the domain of application of SPM to a vast variety of subjects including material science [138–140], nanoscience, bioscience [141, 142], chemistry [143], earth and environmental science *etc.* SPM, when use in the Piezoresponse force microscopy, provides information of ferroelectric/piezoelectric properties of a material. Using scanning-probe based lithography, one can also image, write and erase ferroelectric domains *etc.*.

During my work, I have explored different operational SPM modes like, Atomic force microscopy (AFM) [144], Magnetic force microscopy (MFM) [145], Piezoresponse force microscopy (PFM) [146, 147], lithography [139] to investigate the electric and magnetic properties in various systems like $AgSbSe_2$, SnTe and Silicon, discussed in the following sections. First section is about the investigation of ferroelectric properties at nanometer length scales on the surface of thermoelectric semiconductor $AgSbSe_2$, using piezo-response force microscopy (PFM). Second section unravels the unexpectedly high temperature local ferroelectricity in thermoelectric SnTe. Third section gives the most important message regarding the artifacts of PFM experiments by showing the hysteretic behavior on Silicon which is a non-ferroelectric material. The presented PFM results also indicate that the electrical

response from the materials like silicon, PCB (printed circuit board), which have been used as a substrates, might sometime not be an appropriate measurement to study the ferroelectric/piezoelectric properties of the materials.

6.1 Experimental Details

For SPM measurements, a $3mm \times 3mm$ rectangular sample was loaded on a glass slide using scotch tape and a titanium-Iridium coated tip was mounted at the end of a silicon cantilever. The schematic diagram of PFM measurements is shown in figure 6.1, describing the experimental details to investigate the ferroelectric/piezoelectric properties of the materials. For probing the piezoresponse of the microscopic region underneath the tip, an ac voltage V_{ac} was applied between the tip and the sample mounted on a metal piece which was directly connected to the ground of the voltage source. The frequency of V_{ac} was swept and the amplitude response of the cantilever in the contact mode was recorded to identify the contact resonance frequency of the cantilever on the sample in order to achieve highest sensitivity. In PFM mode, we investigate the ferroelectric ordering on the microscopic region by domain imaging.

PFM imaging was done by bringing the tip in contact with the sample, applying the voltage V_{ac} on the tip and scanning the tip on the sample while keeping the deflection of the cantilever constant. If the electric polarization is opposite in two different domains, the measured value of ϕ varies by 180^0 between the two domains. By plotting the magnitude of ϕ as a function of the position of the tip, a PFM image exhibiting the distribution of ferroelectric domains on the sample surface is constructed. During PFM imaging the resonance frequency might shift as the cantilever rubs against the surface and interacts differently with the sample at different points. In order to track the contact-resonance in real time the measurements were done in so-called DART (dual ac resonance tracking) mode [148].

The spectroscopy mode of PFM shows ferroelectric switching in phase and simultaneously displacement in amplitude due to local ferroelectric domains which are the

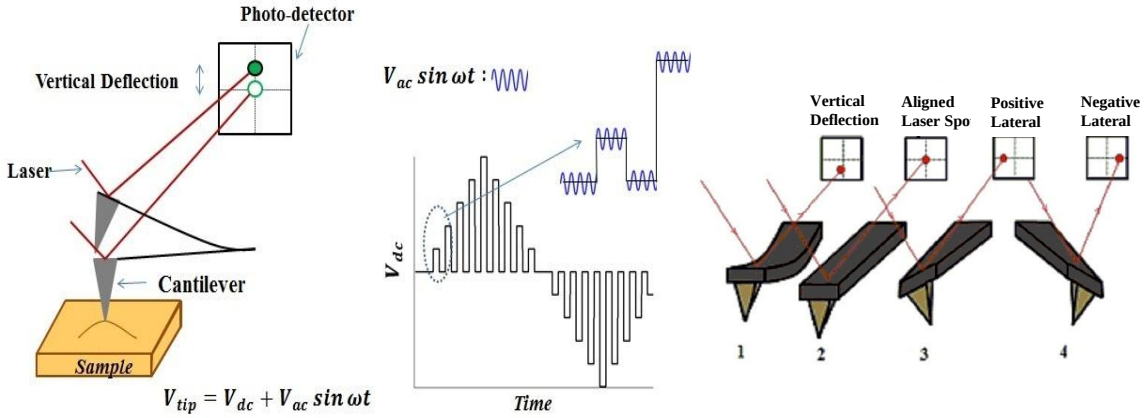

Figure 6.1: The schematic of the PFM technique presenting the switching waveform in the DART PFM spectroscopic mode and the tip movement in Lateral PFM mode.

hallmark signatures of ferroelectric/piezoelectric properties respectively. For PFM spectroscopy measurements, ac voltage ($V = V_{ac}cos\omega t$) is coupled with dc voltage ((V_{dc})) and the sum $V_{tip} = V_{dc} + V_{ac}cos\omega t$ is applied between the tip and the sample. If the sample is piezoelectric, the area underneath the tip will be deformed due to the application of the electric field. Since the applied field has a periodic component, the amplitude of deformation can be written as $A = A_0 + A_\omega cos(\omega t + \phi)$, where ϕ is the phase difference between the applied field and the amplitude response. ϕ gives information about the electric polarization direction below the tip. Depending on the direction of the applied V_{dc}, the polarization underneath the tip switches direction. This is expected to give rise to a 180^0 shift in ϕ vs V_{dc} curve as passes through $V_{dc} = 0$. In general, for ferroelectric switching, the phase ϕ switches hysteretically and shows a finite coercive voltage. Similarly, from local strain vs. voltage measurements we also observe a clear butterfly loop which is a hallmark of piezoelectricity.

However, it should also be noted that such hysteresis in phase and amplitude may also arise from electrostatic and electrochemical effects [139]. In order to minimize the role of the electrostatic effects, all the measurements were performed following SS-PFM (switching spectroscopy piezoresponse force microscopy) pioneered by Jesse *et al.* [149, 150]. In this method, instead of sweeping V_{dc} continuously, it is applied in sequence of pulses and the phase and amplitude measurements are done in the

"off"-states of the pulses. The possibility of electrochemical reactions under the tip is ruled out by topographic imaging after the spectroscopic measurements, where we do not observe any topographic modification that is usually expected to result from tip-induced electrochemical processes [139]. However, ruling out the above-mentioned possibilities with absolute certainty may not be possible by spectroscopic measurements alone. In addition to the hysteretic switching effects, the observation of domains on the sample surface would be unambiguous proof of ferroelectricity.

All the presented data in the following sections to investigate the ferroelectric properties of the materials are confirmed by performing SS-PFM ("off"-states of the pulses) along with ferroelectric domains obtained by PFM imaging which minimizes the artifacts.

6.2 Local ferroelectric ordering in a thermoelectric semiconductor, $AgSbS_2$

Thermoelectric materials enable direct and reversible conversion of untapped heat into electrical energy and will play a significant role in the future energy management [151–156]. Ferroelectric materials exhibit a spontaneous electric polarization that can be reversed by the application of an external electric field. Ferroelectric materials have found several applications in diverse functional systems including capacitors with tunable capacitance [157, 158], non volatile memory devices [159], sensors [160], transistors [161, 162], photovoltaic devices [163], thermistor [164] *etc.* Therefore, combining thermoelectric and ferroelectric properties in a single compound might lead to a new class of multiferroics namely the ferroelectric thermoeletrics that would undoubtedly be of immense fundamental and technological importance. In order to accomplish this, it is most important to first identify the existing high performance thermoelectric materials containing electrically active ferroelectric domains and investigate how ferroelectricity is coupled with thermoelectricity.

Although the direct evidence of ferroelectricity in thermoelectric materials through

the imaging of ferroelectric domains is absent in the literature, few thermoelectrics have been shown to possess local electric polarization. For example, ferroelectric Aurivillius phase, $Bi_4Ti_3O_{12}$, exhibited enhanced thermoelectric behavior [165]. Single crystal of the relaxor ferroelectric oxide, $Sr_{1-x}Ba_xNb_2O_6$, showed low thermal conductivity and high power factor [166]. In the lead chalcogenides, which are known to be high performance thermoelectric materials, local ferroelectric distortion has been observed by pair distribution function analysis of temperature dependent neutron diffraction data [167]. Using combination of inelastic neutron scattering and first principle calculations, strong anharmonic coupling between ferroelectric transverse optic mode and longitudinal acoustic modes have been evidenced in $PbTe$, which has been shown to be important for low thermal conductivity [168]. In certain systems, it was found that the itinerant electrons responsible for electrical conductivity were strongly coupled with the ferroelectric polarization [166, 169]. Therefore, in principle, by tuning ferroelectric properties it should also be possible to tune electrical properties, hence thermoelectric properties, in those systems [170]. In such systems, the nano-meter scale ferroelectric domain boundaries could act as potential scatterers of the mid/long mean free path phonons thereby limiting the thermal conductivity. However, complete understanding of the correlation between ferroelectric and thermoelectric properties, so far, has remained elusive. This understanding is extremely important in order to be able to design novel materials with superior thermoelectric properties by hitherto unexplored techniques like engineering of ferroelectricity in semiconductors. Investigating the possibility of the existence of ferroelectric ordering in novel thermoelectric materials is, therefore, a major step forward to this direction.

In order to study the existence of local ferroelectric ordering by PFM in a new thermoelectric semiconductor $AgSbSe_2$. We perform PFM measurements between a conducting AFM cantilever and a polycrystalline ingot sample of $AgSbSe_2$. $AgSbSe_2$ crystallizes in cubic rock salt structure (space group, $Fm-3m$) with disordered Ag

and Sb positions. $AgSbSe_2$ is a p-type semiconductor that shows high thermoelectric figure of merit, zT that becomes very high ~ 1.2, when properly doped [171, 172]. The high zT was attributed to enhance electrical conductivity and low lattice thermal conductivity. The low lattice thermal conductivity arises due to the presence of high degree of anharmonicity in the $Sb - Se$ bond [173, 174]. Our observation of the existence of strong local ferroelectricity is intriguing as $AgSbSe_2$ crystallizes in centro-symmetric space group ($Fm - 3m$) and therefore no ferroelectricity is expected. However, from high resolution transmission electron microscopy (HRTEM) measurement we found the evidence of local superstructure formation which, we believe, leads to local distortion of the centro-symmetric arrangement in $AgSbSe_2$ and gives rise to the observed ferroelectricity. Stereochemically active $5s^2$ lone pair of Sb can also give rise to local structural distortion, which creates ferroelectricity in $AgSbSe_2$.

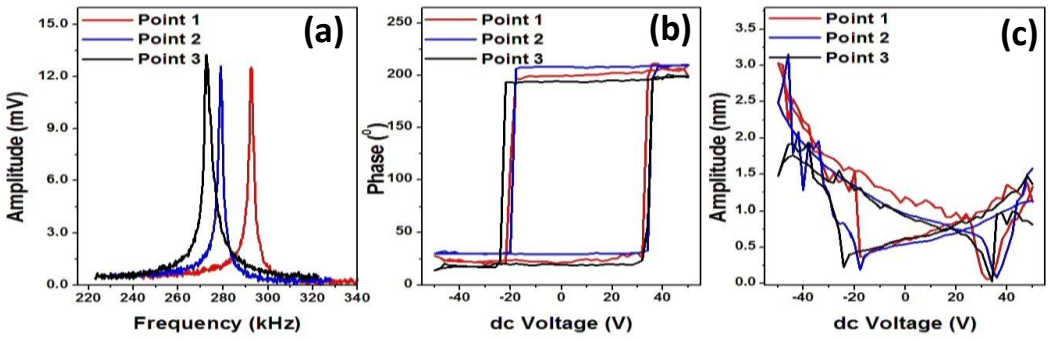

Figure 6.2: (b) Tuning of the conducting AFM cantilever in DART PFM mode prior to spectroscopic measurements. (c) PFM phase hysteresis loop and (d) butterfly loop measured at three different points in the "off"-state.

The contact resonance frequency in order to achieve highest sensitivity is shown in figure 6.2 (a), the contact resonance frequency varied between 270 kHz to 300 kHz during our measurements. In figure 6.2 (b) we show the hysteresis loops obtained at three different points on $AgSbSe_2$. The hysteretic 180$\mathring{A}$ phase switching is clearly visible. For piezoelectric samples, when amplitude A_ω is plotted against the sweeping V_{dc}, the curve is expected to be hysteretic resembling a butterfly. This is called a "butterfly loop" which is traditionally considered to be a hallmark of piezoelectricity. The representative butterfly loops measured at three different points on $AgSbSe_2$

are shown in figure 6.2 (c). Observation of hysteretic phase switching and "butterfly loops" indicate that $AgSbSe_2$ has ferroelectric and piezoelectric properties.

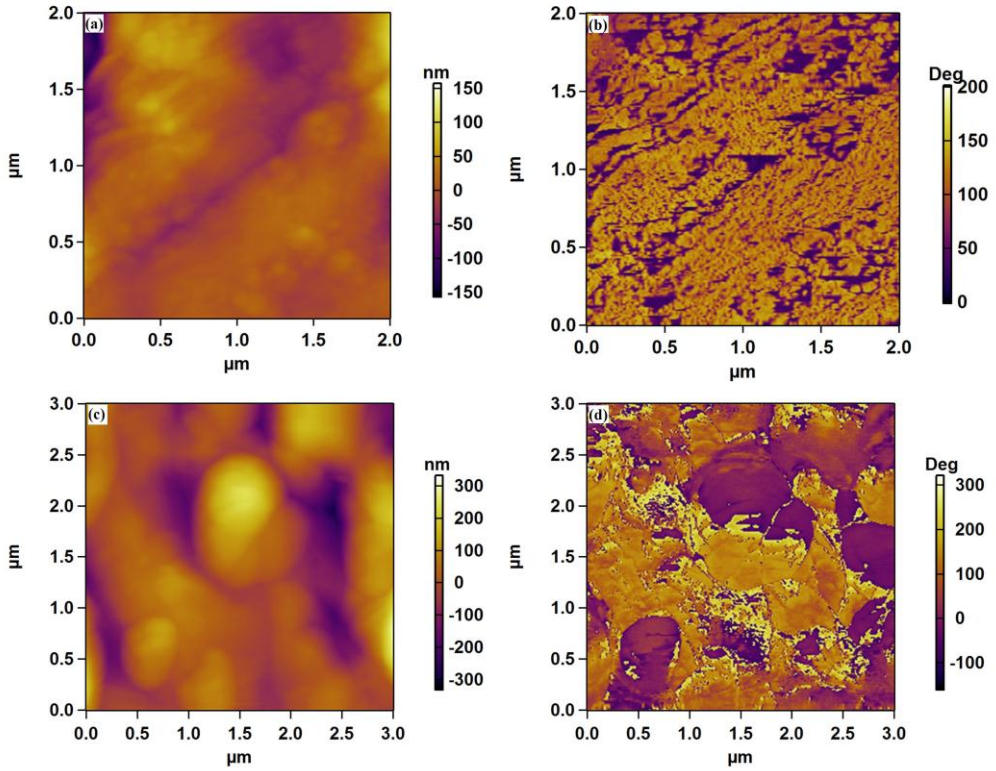

Figure 6.3: (a) Topography of a $2\mu m \times 2\mu m$ area on the sample. (b) PFM phase image showing nanometer scale domains in the same area as in (a). (c) Topography of a $3\mu m \times 3\mu m$ area on the sample. (d) Lateral PFM phase image showing nanometer scale domains in the same area as in (c).

In order to confirm the ferroelectric behavior, we also present the observation of ferroelectric domains by PFM imaging in the following section. In figure 6.3 (a) we show the topographic image of a $2\mu m$ x $2\mu m$ area. In figure 6.3 (b) we show the phase image corresponding to the same area. The phase image shows regions with high (bright) and low (dark) values of ϕ. From the bright to the dark region the phase ϕ shifts by 180° indicating that the bright and dark regions are respectively 'up' polarized and 'down' polarized ferroelectric domains.In the imaging method described above only the vertical amplitude and phase response on the photodiode are recorded. The image thus obtained gives information about the components of electric polarization along the directions parallel and antiparallel to the axis of the tip. By probing the lateral deflection of the cantilever it is also possible to image the domains where the polarization axis remains on the plane of the sample surface.

The images of the lateral domains of a $3\mu m$ x $3\mu m$ area (topography shown in figure 6.3 (c)) is presented in figure 6.3 (d). Bright and dark regions comprising of domains of different electric polarization are clearly visible in the image. There is absolutely no correlation between the topographic and the phase image confirming that the phase image is not affected by the topography.

From the above results it can be inferred that $AgSbSe_2$ has local ferroelectric properties. Since $AgSbSe_2$ crystallizes in the centro-symmetric structure, the observation of ferroelectricity is surprising. It is therefore necessary to understand the origin of ferroelectricity in $AgSbSe_2$. $AgSbSe_2$ is a member of cubic $I-V-VI_2$, where I = Cu, Ag, Au or alkali metal; V = As, Sb, Bi; and VI = Se, Te. In $AgSbSe_2$, the valence electronic configuration of Sb is $5s^2 5p^3$, where only $5p^3$ electrons take part in the formation of bonds with the Se valence electrons, while the beguiling $5s^2$ electrons of Sb form lone pairs. Such ns^2 lone pairs electrons are often found to effective to distort the local structure, resulting in local dipole in the global centro-symmetric structure [167, 175–178]. Thus, lone pair induced local distortion in the structure may give rise to ferroelectric properties in $AgSbSe_2$.

In order to investigate the nanoscale architectures, we have performed transmission electron microscopic (TEM) investigation on pristine $AgSbSe_2$ (figure 6.4 (a)). Although earlier powder X-ray diffraction measurements of $AgSbSe_2$ indicated that Ag and Sb position were disordered in the cation site of the NaCl-type structure [171], careful TEM studies revealed the evidence of local Ag/Sb ordering in nanoscale regions distributed throughout the $AgSbSe_2$ sample. We have also observed weak superstructure spots in the electron diffraction along the $<110>$ and $<201>$ direction (arrows in figure 6.4 (b)), which resulted due to ordering of Ag and Sb atoms in $AgSbSe_2$. Figure 6.4 (c) and figure 6.4 (d) depict representative high resolution TEM (HRTEM) images of $AgSbSe_2$ at two different locations of the sample. The grain size of the present polycrystalline $AgSbSe_2$ varies in between $1.5-3\mu m$. Close inspection of the images reveal the presence of two types of region in the sam-

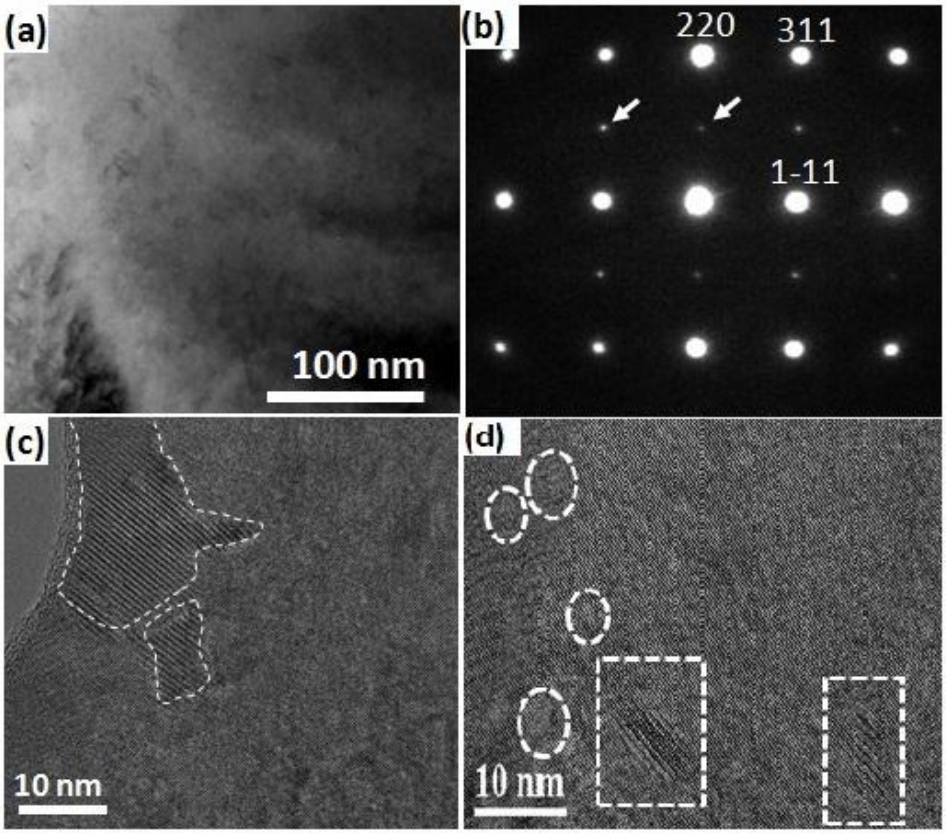

Figure 6.4: Nanoscale architecture of $AgSbSe_2$. (a) Low magnification TEM image of $AgSbSe_2$. (b) Fast Fourier transform (FFT) pattern of (a). Arrows in (b) show the weak superstructure spots. (c, d) High resolution TEM images of $AgSbSe_2$, dotted portion showing nanoprecipitates with the doubling of lattice parameter compared to matrix.

ple. The dotted marked region in the image are nanodomains with doubled lattice parameter (figure 6.4 (c)), which might have formed due to local cation ordering in the $AgSbSe_2$. Similar ordering of cations in $AgSbTe_2$ had been earlier predicted by first-principle calculations for ground state structure [179, 180] and were recently observed by inelastic neutron scattering and TEM investigations in $AgSbTe_2$ [181]. Recent electrical transport measurements on cubic $AgBiS_2$ nanocrystals also indicated the presence of cation ordering near room temperature [182]. The local cation ordering in the nanoscale regime might alter the structure making it non-centrosymmetric locally, which in turn could be responsible for the observed local ferroelectricity in $AgSbSe_2$.

Further, to explore the cross-correlation between thermoelectricity and ferroelectricity in $AgSbSe_2$ we have performed PFM imaging by varying the amount of heat

flowing through the sample. For this measurement we had mounted the sample on a heater plate which is electrically grounded to the high voltage amplifier ground of the AFM electronics. Heat was supplied through the sample by setting the temperature of the heater plate at an elevated value. Since the sample thickness was large ($5\,mm$) and the thermal conductivity of $AgSbSe_2$ is small ($0.35 W m^{-1} K^{-1}$), a natural thermal gradient existed between the bottom and the top surface of the sample. PFM imaging was done on the top surface. The heat flow-dependent data is presented in the figure 6.5. The top panels show the topography confirming that for all heater temperatures we have scanned the same area. The bottom panels demonstrate the clear change in the domain structures.

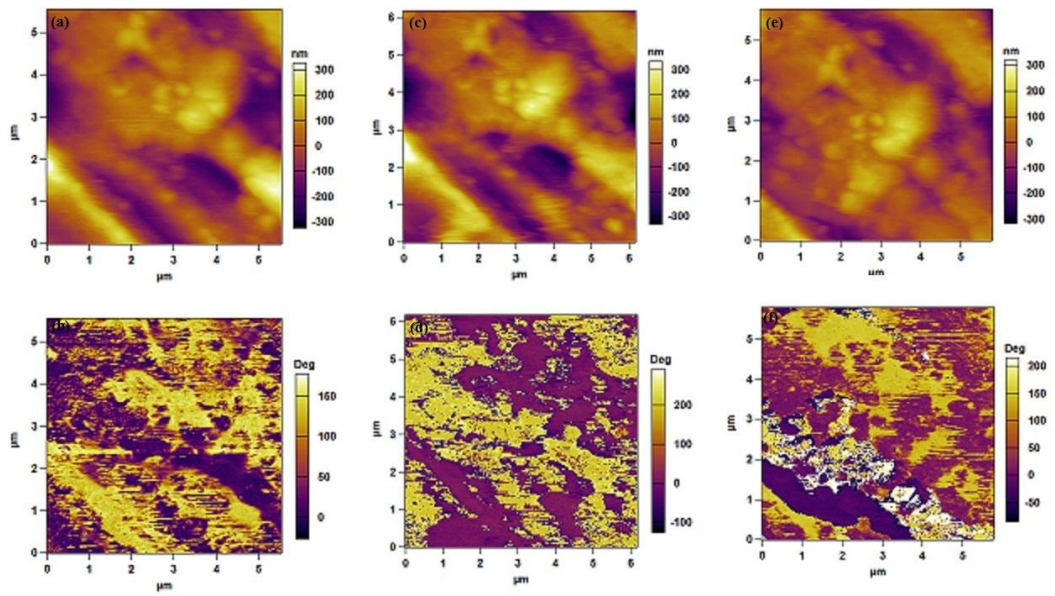

Figure 6.5: PFM images with varying heat flow: (a) Topography (top) and (b) PFM phase image (bottom) at room temperature without heating the sample. (c) Topography (top) and (d) PFM phase image (bottom) while keeping the base of the sample at $100°C$ C and scanning on the top of the sample. (e) Topography (top) and (f) PFM phase image (bottom) while keeping the base of the sample at $200°C$ and scanning on the top of the sample. From the topographic images it is clear that we have scanned the same area at different heating level with little thermal drift. The change in the corresponding domain structures with temperature is clear.

It is seen that with varying heat flow, the ferroelectric domain structures change significantly indicating that ferroelectricity and thermoelectricity in $AgSbSe_2$ are cross-correlated. It was suggested in the past that ferroelectric domain-walls might scatter phonons causing a reduction of k_{lat} [183]. The effect of ferroelectric domains

on the thermoelectric properties may be further investigated by artificially designing the domain structures by nano-structuring and/or by fabricating epitaxial thin films on different substrates [184].

In conclusion, we have performed PFM on $AgSbSe_2$ and observed the signature of strong local ferroelectricity and piezoelectricity. From nanoscale structural analysis we show that natural formation of superstructure nanodomains in the sample makes the local crystal structure to be non-centrosymmetric, thereby inducing ferroelectricity. The local dipole could also be created due to the local structural distortion caused by $5s^2$ lone pair of Sb. Nano-meter scale ferroelectric domains were clearly imaged by PFM. The naturally occurring ferroelectric domain-walls might act as effective scatterers for phonons and reduce the thermal conductivity of the materials. Based on the observation reported in this Letter, enhancing thermoelectricity by ferroelectric domain engineering might emerge as a promising field of research. Further, it would be interesting to search for ferroelectricity in other known $I - V - VI_2$ thermoelectric semiconductors.

6.3 Local Ferroelectricity in SnTe above Room Temperature

It is well known that a crystal with centro-symmetric structure cannot exhibit macroscopic electric dipoles, i.e ferroelectricity. In these systems, the center of positive charges coincides with the center of negative charges. However, there are rarely known systems, in which emergence of a locally broken symmetry state arises from a high symmetry state [167,185–188]. In centro-symmetric lead chalcogenides (PbTe and PbS) with rocksalt cubic structure, which are known to be high performance thermoelectrics, [189–191] local structural distortion has been evidenced in atomic pair distribution function (PDF) analysis of the temperature dependent neutron diffraction data. [167] The PDF analysis, which simultaneously probes both average and local atomic structure, revealed that a local off-centering of Pb in PbTe and

PbS is as large as of 0.25 $\mathring{A}$. [167] This finding was supported by maximum entropy analysis of single-crystal diffraction [188] as well as ab initio molecular dynamics simulations. [192, 193] However, extended X-ray absorption fine structure (EXAFS) investigation showed no evidence of Pb off-centering at all in PbTe. [194] Thus, interpretation of the PDF and EXAFS data has been tricky and contradictory, and possible existence and understanding of the mechanism of local structural distortion induced dipole formation in PbTe are unclear.,

SnTe, a lead-free rocksalt analogue of PbTe, with similar electronic structure as of PbTe, has recently attracted attention due to its high thermoelectric performance [195–199] and topological crystalline insulating properties. [199–201] SnTe has a low temperature ferroelectric phase below 100 K, having a non-centrosymmetric rhombohedral structure (R3m), that transforms to a centrosymmetric cubic phase ($Fm3-m$) above 100 K. [202–204] However, at higher temperatures, like in PbTe, there has been indication of the development of local rhombohedral distortion (Sn-off centering) in the globally cubic phase of SnTe. [202–204] Such local distortion in the crystal structure on warming was shown by temperature dependent PDF [202] as well as EXAFS studies. [203] Based on inelastic neutron scattering and first principle calculations, strong anharmonic coupling between ferroelectric transverse optic mode and longitudinal acoustic modes were evidenced in PbTe, which was shown to be important for low thermal conductivity. [204, 205] Recent inelastic neutron scattering experiments have revealed that transverse optic mode in SnTe is less anharmonic than PbTe, even though SnTe is closer to ferroelectric instability. [206] However, owing to relatively high charge carrier density in SnTe originating from intrinsic Sn vacancies, it is commonly believed that such local distortion of crystal structure may not drive the system into a locally ferroelectric state, where the electric polarization can be switched by an external electric field.

Herein, we use the temperature-dependent PFM to directly show that local ferroelectric domains exist in SnTe at high temperatures (300-473 K) that can be switched

by an externally applied electric field, although there is no global ferroelectric ordering. We observe a clear butterfly loop in the local strain measured as a function of electric field, which is a hall-mark of piezoelectricity. We have employed first-principles Density Functional Theory (DFT) calculations to understand the origin of the local ferroelectricity in SnTe.

We brought a conducting $Pt-Ir$ coated Si tip mounted on a cantilever in contact with the surface of a high quality rectangular polycrystalline sample of SnTe. In order to probe the ferroelectric and piezoelectric properties of the microscopic region underneath the tip, an ac voltage V_{ac} was applied between the tip and the sample. In contact mode, frequency dependent amplitude (V_{ac}) response of the cantilever was recorded to identify the contact resonance frequency of the cantilever. [138] All the measurements presented here were performed at the contact resonance frequency in order to achieve the highest sensitivity. As shown in figure 6.6 (a), the contact resonance frequency varied between 50 kHz to 60 kHz during our measurements.

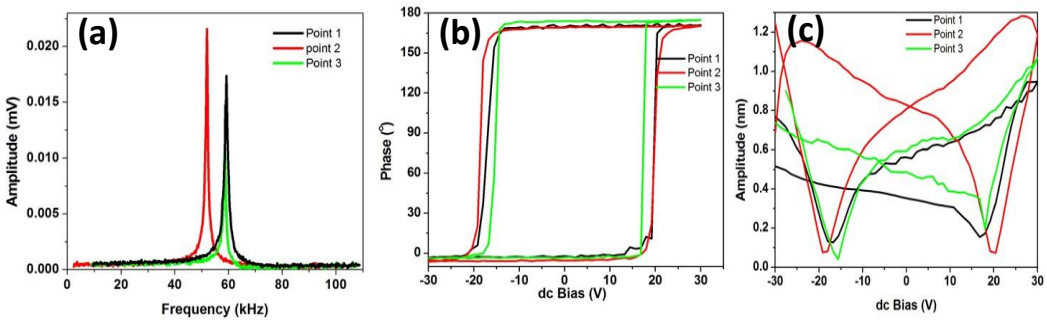

Figure 6.6: (a) Tuning curve of $Pt-Ir$ conducting tip, (b) Hysteresis loops between phase and dc bias of 30 V and, (c) butterfly-like loops between response signal and DC bias at three different points on the sample in the "off" state.

In figure 6.6 (b), the hysteresis loop with coercive voltage 20 V and 180 Åswitching of phase at three different points on the $2\mu m$ x $2\mu m$ area of the SnTe is shown which directly shows switching of ferroelectric polarization. It should be noted that the length scale that is probed at a time is of the order of 40 nm which is estimated from the tip size. The butterfly loops captured at corresponding three points are also shown in figure 6.6 (c).

Excluding ferroelectricity, other factors like electrostatic effects or electro-chemical

effects could also contribute to phase switching in PFM experiments. [139, 149] In order to minimize the role of electrostatic effects, all the spectroscopic measurements were done in off state of the DC pulse sequence following the switching spectroscopy PFM protocol pioneered by Jesse *et al.* [149,150] In order to confirm the absence of the electro-chemical effects, [148] we performed non-contact topographic measurements after PFM spectroscopy. However, no topographic structure growth due to local electrochemical reaction was observed. In addition, we have performed measurements by changing the temperature and relative humidity of the room and no noticeable difference in the results were seen.

To further confirm the presence of local ferroelectricity in SnTe, we also imaged the ferroelectric domains using DART PFM imaging mode. In this, an AC signal was sent to the conducting probe which was in contact with the sample and the response signal was measured as a function of the position of the tip on the sample. Since the resonance frequency of the cantilever might also depend on the position of the cantilever on the sample due to the variation in local physical properties of the sample, the contact-mode resonance frequency of the cantilever may vary as the tip scans on the sample. Since the resonance frequency of the cantilever might also depend on the position of the cantilever on the sample due to the variation in local physical properties of the sample, the contact-mode resonance frequency of the cantilever may vary as the tip scans on the sample.

To keep the cantilever in resonance during the entire measurement an additional feedback loop was used to track the shift in resonance frequency and drive the cantilever at resonance throughout the imaging process [26]. In figure 6.7 (a), the topographic image of the sample of $2\mu m$ x $2\mu m$ areas is shown. In figure 6.7 (b), the phase image corresponding to the same area is also shown. Though the phase image appears different from the topographic image, certain amount of topographic cross-talk can also be seen in the phase image. The color contrast in the phase image exhibits the distribution of domains with polarization pointing to different

directions. The phase image shows regions with high (bright) and low (dark) values of . From the bright to the dark region the phase shifts by 180° indicating that the bright and dark regions are respectively 'up' polarized and 'down' polarized ferroelectric domains.

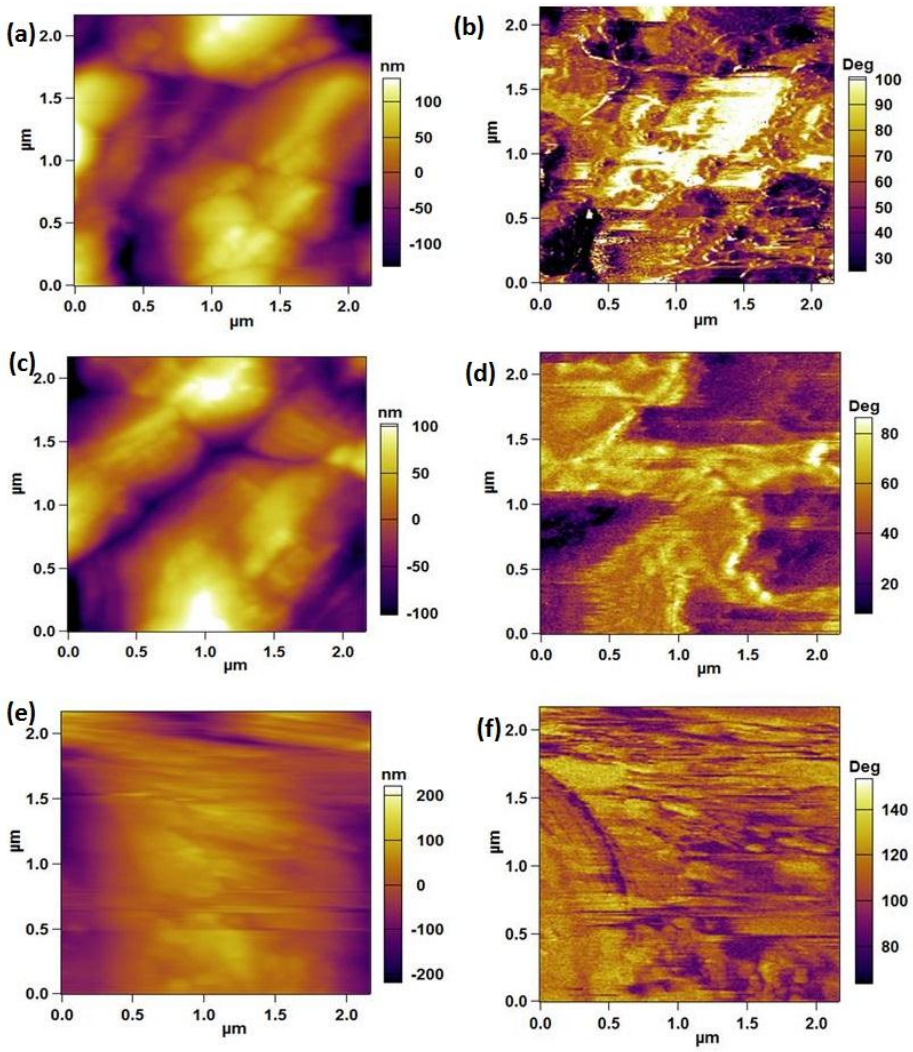

Figure 6.7: Ferroelectric domains imaged at different temperatures. (a), (b) topography and phase images respectively on $2\,\mu m \times 2\,\mu m$ area of the sample at $50°C$. (c), (d) topography and phase images respectively on 2 m x 2 m area of the sample at $150°C$. (e), (f) topography and phase images respectively on 2 m x 2 m area of the sample at $200°C$.

To investigate the temperature dependence of the ferroelectric phase, we have performed PFM imaging at higher temperatures up to 200°C. The domains are seen to exist up to 200°C. The domains imaged at 50°C, 150°C and 200°C are shown in figure 6.8. Due to the increased thermal drift during scans at higher temperatures, the domain boundaries could not be clearly resolved, which restricted us from clearly

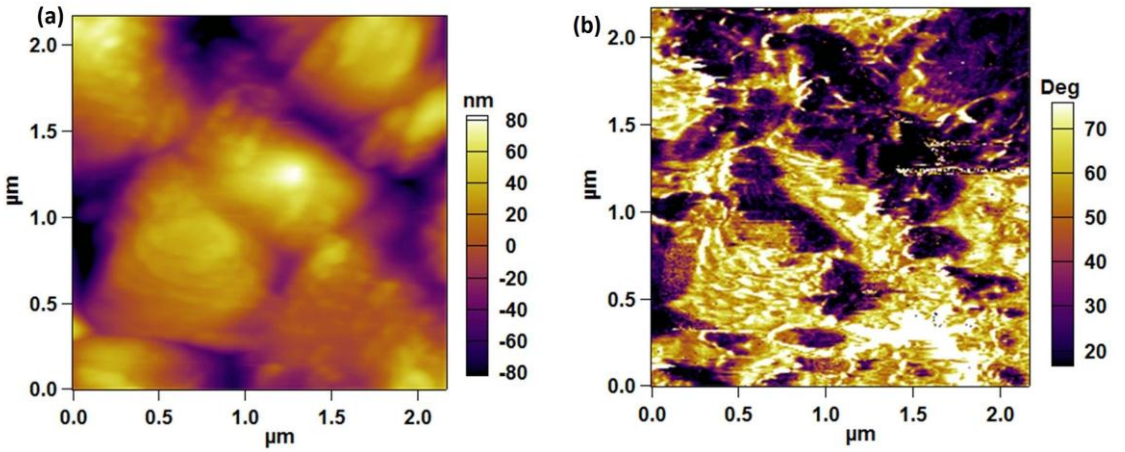

Figure 6.8: (a) Topographic image on $2\mu m \times 2\mu m$ area on the sample using DART PFM. (b) Phase image on the same region of the sample as in (a) showing domains at room temperature.

detecting the evolution of the domain shape and size with increasing temperature.

The PFM results clearly demonstrate the existence of local ferroelectric ordering in SnTe. Since SnTe crystallizes globally in a cetrosymmetric structure, the observation of ferroelectricity is surprising. It is therefore necessary to understand the origin of local ferroelectricity in SnTe. Local off-centering of Sn atom in SnTe was earlier confirmed by PDF [202] and EXAFS [203]analysis. Such off-centering might create a local rhombohedral distortion, thereby resulting in local dipole in the global centrosymmetric structure. [138, 176, 177] In addition, for SnTe, sp-hybridization is small as s-band (lone pair) is significantly lower in energy than p-band. Therefore valence state is mainly contributed by p electrons and each atom has three valence electrons on average. Both Sn and Te in SnTe occupy octahedral coordination sites; thus the required number of valence electrons per atom is six for forming six bonds. Given the octahedral structure of SnTe and its three valence electrons per atom, the choice of bond occupation is not unique. This leads to hybridization between all possible choices for the three electrons forming six bonds. Such resonance or hybridization between different electronic configurations is known as resonant bonding, which should make the bonds in SnTe soft. [203, 207] Resonant bonding might also lead to low frequency (soft) transverse optical phonon modes in SnTe thereby causing local rhombohedral distortion (local dipoles) in otherwise cetrosymmetric cubic

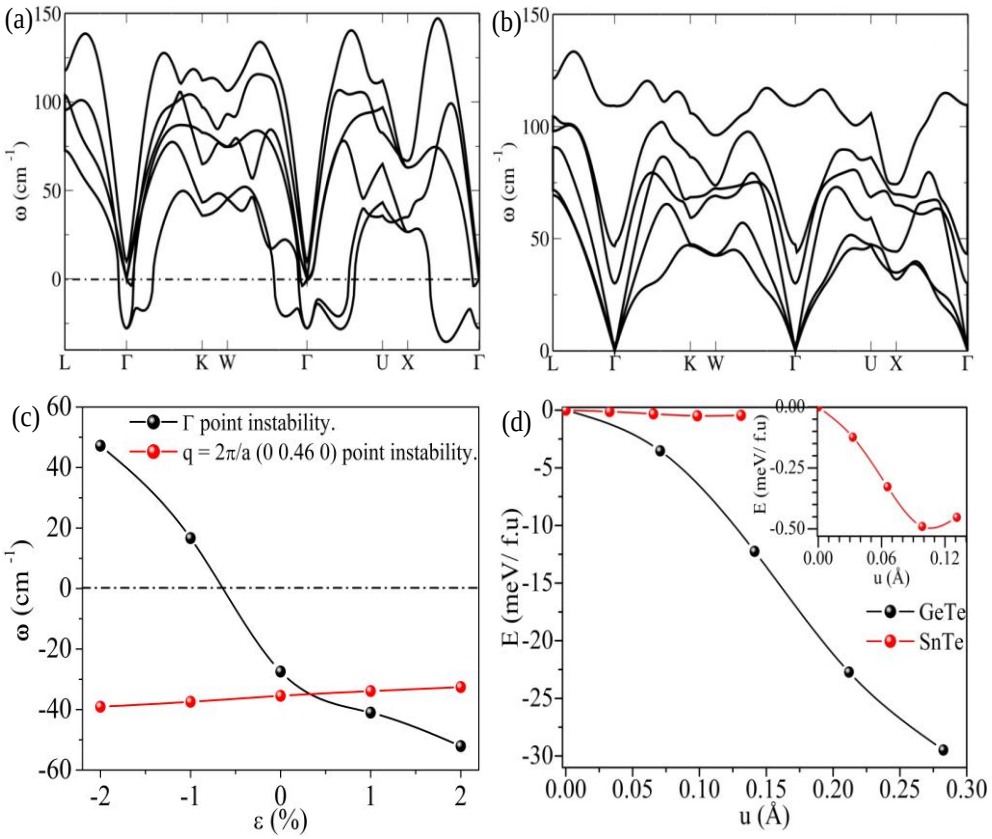

Figure 6.9: Phonon dispersion of (a) SnTe in the centrosymmetric cubic rocksalt structure and in its (b) structure with Sn sublattice off-centered along (111) direction by $\sim 0.13\,\mathring{A}$; (c) Dependence of unstable phonon frequencies at q = 2/a (0 0 0) and q = 2/a (0 0.46 0) on hydrostatic strain ($\varepsilon = aa_0/a_0$), where $a_0 = 6.419\mathring{A}$; and (d) Dependence of total energy difference (per formula unit) between ferroelectric and paraelectric states of SnTe and GeTe, with electric dipole arising from displacement of Sn and Ge along (111) direction. Inset: (d) magnified plot for SnTe.

structure. Another way to view this problem is to understand the role of $5s^2$ lone pair of electron of Sn in SnTe, which is often effective in distorting the local structure, resulting in a local dipole in the cetrosymmetric structures. [138, 176, 202, 203]

To gain deeper understanding of the local ferroelectricity in SnTe observed here, we determined phonon spectrum (figure 6.9 (a)) of its centrosymmetric cubic structure using first-principles Density Functional Perturbation Theory (DFPT). Optical phonons exhibit triply degenerate instability with frequency of $28icm^{-1}$ at the Γ point. To identify related structural instabilities, we examined phonon spectrum along the k-point path (L → Γ → K → W → Γ → U → X → Γ) in the Brillouin Zone, covering all the high symmetry directions that join with five other high symmetry (K, L, X, W, U) points. In addition to the point instability, we find a set

of unstable modes (see figure 6.9 (a)) in small pockets of the k-space lying along the paths $\Gamma \rightarrow$ X and $\Gamma \rightarrow$ U. The strongest instability at $q = 2\pi/a$ (0, 0.46, 0) is slightly stronger ($35\, cm^{-1}$) than the one at point. The transverse phonon instabilities at wave vectors in the neighborhood of $q = 2\pi/a$ (0, 0.46, 0) give long period anti-ferroelectric displacements of atoms (like in 180° domain walls). The frequencies of these unstable modes vary sharply in k-space (see path $\Gamma \rightarrow$ X figure 6.9 (a)), signifying fairly long-range interactions. From the mixed opto-acoustic character of these normal modes, the origin of long-range interaction is traced to coupling between acoustic and optical modes. Thus, cubic SnTe exhibits polar instabilities of comparable strengths at the long wavelength (at Γ, ferroelectric) as well as at intermediate (at $q = 2\pi/a$ (0, 0.46, 0)) wavelengths.

We compared this behavior of SnTe with that of cubic GeTe, a closely related conventional ferroelectric. GeTe is the only other ferroelectric (at low temperatures) in the family of $IV - VI$ rock salt chalcogenide with cation off-centering along (111). [208] In contrast to SnTe, the instability at the point of GeTe is the strongest among all of its structural instabilities. We determined energetics of the distortions of the cubic structure of SnTe with the unstable mode at point, by displacing the atoms along its eigenvectors, and relaxed the structure. The off-centering of the Sn atoms after complete relaxation of the structure is $\sim 0.13 \mathring{A}$ along the (111) direction, which is accompanied by a rhombohedral strain ($a = 4.55\, \mathring{A}$, $\alpha = 59.780$) in the cubic unit cell. Phonon spectrum of the relaxed structure with off-centered Sn sub-lattice exhibits no unstable modes (see figure 6.9 (b)), showing that uniform Sn off-centering makes the structure locally stable and energetically favorable to the cubic one as a result of weak anharmonicity evident in its shallow double well energetics (figure 6.9 (d)).

The structural distortion associated with Sn off-centering in the cubic structure of SnTe is expected to couple with strain. Since various phonon instabilities in SnTe are of comparable strengths, we determine their dependence on strain (see figure

6.9 (c)). Clearly, the ferroelectric instability at point varies strongly with strain, vanishing completely upon application of small negative (compressive) strain, but dominating in strength at positive (tensile) strains. The phonon spectrum of SnTe at a tensile strain $\varepsilon = 0.02$, in fact, bears a striking resemblance with that of GeTe. In contrast, the instability at the point $q = 2\pi/a$ (0, 0.46, 0) is relatively insensitive to strain, persisting for compressive strains of $\varepsilon = -0.02$. The mixed acoustic and optical character of the unstable modes at $q = 2\pi/a$ (0, 0.46, 0) evidently becomes weaker for $\varepsilon = -0.02$. Such competition between ferroelectric (Γ) and intermediate wavelength instability and crossover in their dominance with local strain is responsible for the local ferroelectricity observed here. The energy gain associated with cationic off-centering along (111) direction in SnTe (see inset figure 6.9 (d)) is marginal. In comparison with other ferroelectrics the cationic displacement is however quite sizeable ($\sim 0.13\,\mathring{A}$). From the comparison of such energetics of cationic displacement in SnTe and that in GeTe (figure 6.9 (d)), it is clear that both the ferroelectric instability and anharmonicity of SnTe are much weaker than those in GeTe [32]. This is consistent with our interpretations of the experiment here that the Sn-Te bonds in SnTe are resonant with a very small stiffness (soft bonds), and hence there is a small energy barrier for switching of its dipole moment. Hence, a switchable local polarization is possible in SnTe.

Recent experimental observations by Knox et al. [202] using pair distribution function (PDF) analysis give a strong evidence of the flat energy well we find in SnTe (see figure 6.9 (d)).The authors observe relative sub-lattice shift of about 0.02 Åin the low temperature ferroelectric phase ($T_C \sim 100\,K$) of SnTe, while the high temperature (above 400 K) locally off-centered emphanitic phase exhibited atomic displacements of about $0.05\,\mathring{A}$ [16]. However, allowing for local distortions explicitly in the PDF analysis of the emphanitic phase produced atomic off-centering in the range $0.1 - 0.2\mathring{A}$. This variability in atomic displacements is consistent with a highly shallow energy surface and soft bonding in SnTe evident in figure 6.9 (d). Thus,

the local ferroelectricity observed in SnTe above room temperature arises from (a) its easily switchable dipoles due to a flat energy well, (b) its weak ferroelectric instability competing with other intermediate wavelength $\lambda \in [2a_0, \infty]$ instabilities of comparable strengths, which disrupt long range ferroelectric ordering, and (c) a disparate anharmonic coupling of these polar instabilities with strain.

In conclusion, through direct PFM measurements of local polarization switching, we demonstrate that the recently discovered topological crystalline insulator, SnTe, exhibits local ferroelectric ordering in globally centrosymmetric cubic structure above room temperature. Local ferroelectric ordering arises from the emergence of dipoles associated with local structural distortions (Sn off-centering) accompanied by local rhombohedral strain in the cubic SnTe, that originate from soft resonant bonding and competing polar phonon instabilities. It will be worth searching for local ferroelectricity in other resonantly bonded solids with cetrosymmetric structure, such as PbTe, PbSe and PbS using local probes like PFM.

6.4 PFM is not a " Smoking Gun" of ferroelectricity: Voltage induced local hysteretic phase switching in silicon

Owing to its semiconducting behavior, resilience against high temperature and high electrical power, silicon has become one of the most popular substrates for wide variety of systems ranging from thin solid films to bio-materials. [209–211] Such systems grown/mounted on silicon are studied by diverse characterization and measurement probes. One of the important measurement techniques where silicon is often used as a substrate is piezoresponse force microscopy (PFM). [210–212] In PFM spectroscopy, a conducting AFM (atomic force microscope) cantilever is brought in touch with a sample and the electro-mechanical interaction between the cantilever and the sample is studied to determine how the sample responds to a sweeping dc electric field applied on the cantilever. An ac signal rides on the sweeping dc field for tracking the sample characteristics as the dc field sweeps. [212, 213] In PFM

spectroscopy 180^0 phase switching with voltage and a hysteresis in the phase vs. dc voltage plot is traditionally considered to be a signature of polarization switching thereby confirming the material under study to be ferroelectric. Furthermore, a hysteretic amplitude vs. dc voltage curve (traditionally known as a "butterfly loop") is considered to be the hallmark of piezoelectricity. [213] Silicon has been used in the past as a very popular substrate for searching potential ferroelectrics/piezoelectrics by PFM in solid semiconducting films [214], ferroelectric films, [215] soft materials [211], bio-materials [216, 217] etc. Silicon is widely used as a substrate for PFM because it is thought that silicon is not ferroelectric and therefore it does not contribute to phase-switching.

In the past the effect of the application of a large electric field by an AFM tip on the surface of silicon in air was studied. In such studies, it was observed that the silicon surface undergoes an electrochemical reaction resulting in nano-scale structures of silicon oxide on the surface under the AFM tip. [218–223] However, the electrical response of silicon was not studied by PFM spectroscopy and the role of the substrate in PFM measurements on materials mounted on silicon remained unknown.

Here, we report PFM measurements on un-doped silicon (100) wafers of resistivity $\sim 10\Omega - cm$ in air. The silicon wafers exhibit clear and strong hysteresis as well as "butterfly loops". Nano-structures of silicon oxide grow under the PFM tip during the hysteresis measurements due to the electrochemical reaction initiated by the applied measurement potential. From the measurements on thick non-ferroelectric samples mounted on silicon, we show that the observed hysteresis on silicon in air may contribute significantly to the response from the sample mounted on it. This might give rise to misleading results about the ferroelectric/piezoelectric properties of samples mounted on silicon. We have repeated the experiments on silicon wafers with different doping and different crystal orientation, no dependence on doping or orientation was observed.

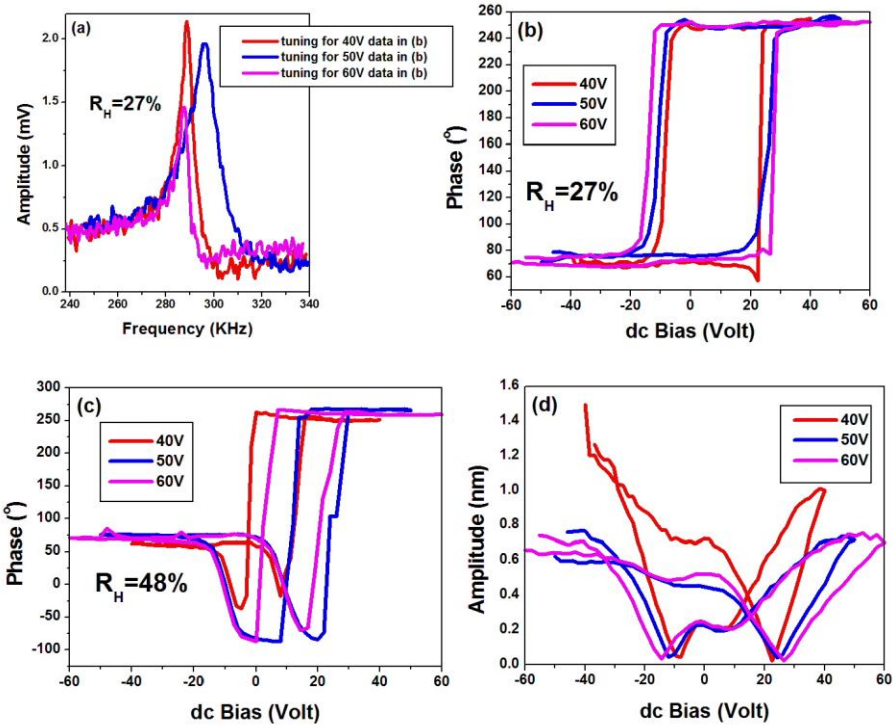

Figure 6.10: "Piezo-response"-like signal observed on silicon: (a) Tuning of the conducting AFM cantilever in the PFM mode prior to spectroscopic measurements, (b) Phase vs. dc-Bias data (at relative humidity $R_H = 27\%$) showing hysteresis for the maximum dc- voltage of $40V$ (red), $50V$ (blue), and $60V$ (magenta), (c) Phase vs. dc-Bias data (at relative humidity $R_H = 48\%$) showing hysteresis for maximum dc- voltages of $40V$ (red), $50V$ (blue), and $60V$ (magenta), (d) Amplitude vs. dc-Bias data showing "hysteresis loops" for maximum dc- voltages of $40V$ (red), $50V$ (blue) and $60V$ (magenta).

In figure 6.10 (a), the in-contact resonance frequency varied between 280 to 300 kHz. The measurements were carried out at the resonance frequency in order to achieve higher sensitivity and for simultaneously obtaining spectroscopic information regarding strain and dissipation. The entire work was done in dual AC resonance tracking (DART) mode of PFM. [148] V_{ac} was kept constant at $10V$ during all the measurements.

In figure 6.10 (b), we show the hysteresis in phase (ϕ) vs. dc bias (V_{dc}) plots for different ranges of V_{dc}. At a relative humidity of 27%, we clearly observe hysteresis loops for all ranges of V_{dc}, where the phase switches by nearly 180^0 with a coercive voltage of $18-20V$. A phase switching of 180^0 is generally believed to originate from polarization switching in ferro-electrics. The coercive voltage in this case depends on the maximum V_{dc} applied. Coercive voltage increases by approximately 10% as

the maximum applied V_{dc} increases from $40V$ to $60V$. The overall shape of the hysteresis loop significantly depends on the ambient relative humidity. At higher humidity levels (typically for $R_H \sim 40\%$), we also observe a dip near the switching bias in the hysteresis loop. Figure 6.10(c) shows the hysteresis data obtained at $R_H = 48\%$, where the dip is very large. The amplitude (A) vs. V_{dc} curve (shown in figure 6.10 (d)) is also hysteretic and the shape of the loop strongly resembles the so-called "butterfly loop" normally observed in piezoelectrics. The amplitude (A) is directly related to the local strain experienced by the cantilever. In case of piezoelectric materials the hysteresis in strain vs. voltage originate from the dynamics of the piezoelectric domains in the material under an applied electric field [224]. We have also investigated the time relaxation dynamics by varying the rate at which we applied the voltage pulses during spectroscopic measurements. No clear dependence of the spectroscopic data on the pulse rate was observed.

After every spectroscopic measurement we imaged the topography in non-contact mode and observed that nanometer size structures were grown on the points where the measurements were carried out. The overall size of the nano-structures varied as the maximum range of V_{dc} varied. In figure 6.11 (a), we show the topographic image of an area where a number of measurements were done with different ranges of V_{dc}. The nano-structures grown during the spectroscopic measurements for different V_{dc} are clearly visible in the figure. [225] In figure 6.11 (b) we show the height and width of the nano-structures grown corresponding to the line-cuts drawn in figure 6.11 (a). In the insets of figure 6.11 (b) and figure 6.11 (d) we also show how the heights vary with the maximum V_{dc} range applied. It is seen that the height of the nano-structures grown during spectroscopy are $90nm$, $190nm$, $210nm$, $470nm$ for the maximum V_{dc} ranges of $80V$, $90V$, $100V$, and $110V$ respectively.

In order to understand the possible role of applied bias on the growth of nano-structures during spectroscopic measurements, we have attempted to grow nano-structures on the silicon surface by usual AFM lithographic technique. In this tech-

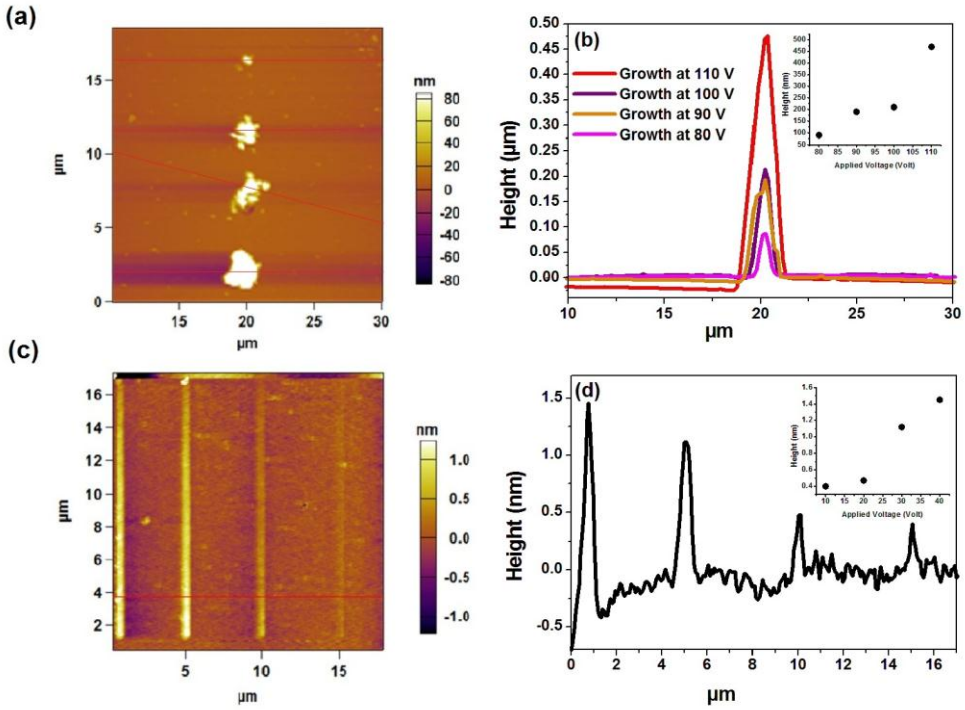

Figure 6.11: (a) Topographic image of nano-structures grown on silicon during spectroscopic measurements with maximum bias of $80V$, $90V$, $100V$, $110V$, (b) height variation of the nano-structures grown during measurements at $80V$ (magenta), $90V$ (orange), $100V$ (purple), $110V$ (red) corresponding to the line-cuts shown in (a),(c) Topographic image of nanowires lithographically written on silicon by the AFM tip at $10V$, $20V$, $30V$, and $40V$, (d) height variations of nanowires corresponding to the line-cut in (c).

nique simply a dc-voltage is applied to the tip and the tip is scanned along a designed geometrical shape on the sample surface. [226] If the sample material is electrochemically active, the applied voltage will write a nano-structure on the sample as the tip scans over it. In contrast, during the spectroscopic measurements, the tip remains in contact with the sample at a particular point and the voltage is scanned between $-V_{dc}$ and $+V_{dc}$. In figure 6.11 (c), we show four parallel nano-wires lithographically grown on the same silicon wafer by a conducting tip with applied voltages of $10\,V$, $20\,V$, $30\,V$, and $40\,V$, respectively. From the line profile corresponding to the line-cut shown in the image (figure 6.11 (d)), it is clear that height and the width of the lithographically written nano-wires are dependent on the voltage between the tip and Silicon. The height of the nano-wires are $0.40\,nm, 0.4\,7nm, 1.12\,nm, 1.45\,nm$ at $10\,V, 20\,V, 30\,V$, and $40V$ respectively. The growth of such nanostructures was not reversible, i.e., applying an opposite voltage after writing a structure did not

erase the structure. The growth of such nano-wires on silicon surfaces was investigated [218, 219, 221, 227, 228], and was attributed to electro-chemical reactions on the silicon surface in presence of moisture. From various analytical tools it was inferred that the chemical composition of these structures were primarily silicon oxide [229]. Therefore, it is rational to conclude that the nano-structures grown during the spectroscopic measurements that we have carried out are also primarily made up of silicon oxide formed due to the application of a high measurement voltage in the presence of moisture.

In the context of electrochemical strain microscopy (ESM) [230, 231], it has been demonstrated that the growth of nano-structures underneath a conducting cantilever might give rise to a deflection of the cantilever due to the electrochemical strain developed during the reaction. [232] This might also lead to a hysteresis in the phase and amplitude as we observe in the case of silicon. In case of silicon, since the shape of the hysteresis loop depends on the relative humidity of the ambience during the measurements, it can be inferred that the electrochemical processes are indeed playing prominent role in generating the hysteresis effects. From the AFM imaging and PFM spectroscopy alone it is impossible to comment on the reaction dynamics under the tip. From the visual inspection of the hysteresis data it is clear that the reaction dynamics is different at different humidity levels. While the hysteresis itself may originate from some electrochemical reaction that leads to the nano-structure growth, the dip in the phase vs. voltage curve at high humidity might arise from a secondary chemical reaction favoured by high level of moisture. This is somewhat similar to what is observed in the current(I) vs. voltage (V) response in cyclic voltametry of electrochemical processes with liquid electrolytes. [233] It should be noted that even in the case of typical cyclic voltametry, the current vs. voltage curves often show hysteresis and when more than one reactions are involved, corresponding multiple features are observed in the hystertic $I - V$ curves.

It is usually believed if the thickness of a given sample is large enough, the contri-

bution from the substrate in the PFM results obtained on the samples (mounted on the substrate) is not significant. This idea has been quantitatively explored in the modified effective charge model developed by Morozovska et al. [234] According to this model, the electric field induced by a charged PFM tip on the surface is given by $E_3 \propto \frac{Q}{(x_3+d)^2}$, where Q is the effective charge on the tip which is proportional to the applied voltage V_{dc}, d is the distance between the tip and the equipotential surface underneath the sample and x_3 is the distance of the measured surface from the equipotential surface under the sample, which is usually equal to the sample thickness. It is argued that when the sample is thick *i.e.*, d is large, the effective electric field experienced by the underlying substrate is small and hence, the voltage induced dynamics of the substrate should not contribute in the spectroscopic measurements on the sample. Even though this model is widely used for analysing PFM data on new materials, it should be noted that this model has been developed for ferroelectric domain nucleation and switching. When the hysteresis appears from phenomena not related to ferro-electricity, applying this model to rule out the role of the substrate for thick samples may not be appropriate. In order to investigate the influence of the silicon substrate on PFM measurements, we mounted a $1.36\,mm$ thick Printed Circuit Board (PCB) (a known non-ferroelectric insulator) on silicon and observed clear hysteresis and "butterfly loops" (figure 6.12 (c), figure 6.12 (e)). Furthermore, for $R_H > 40\,\%$ a dip near the switching bias appeared, which is similar to the characteristic dip observed on silicon (figure 6.12 (b)) for $R_H > 40\,\%$. When the measurement is done on the piece of PCB alone (mounted on a metal disk), hysteretic behavior is observed (figure 6.12 (a,b))that shows identical shape at all humidity levels i.e., the dip does not appear at high humidity levels. Hence, it is clear that the dip observed in PCB mounted on silicon at higher humidity levels appears due to the contribution from the silicon substrate. It can be concluded that when PFM measurements are performed on samples mounted on silicon, hysteresis effects that mimic ferroelectricity-induced switching may be obtained.

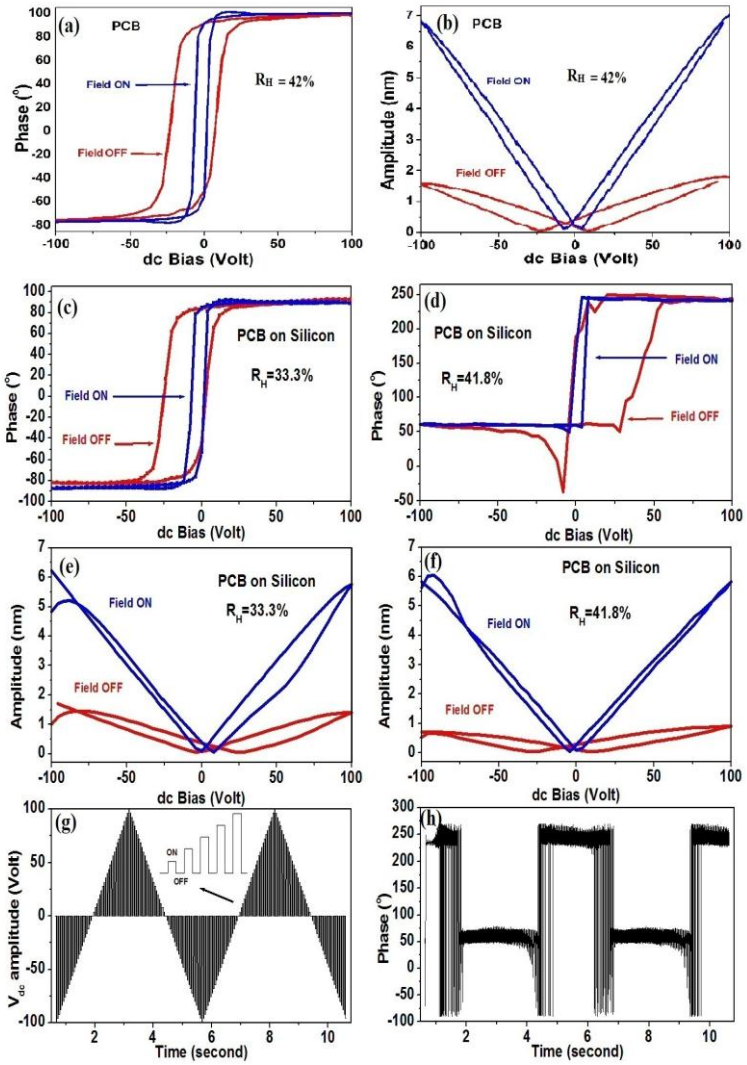

Figure 6.12: (a)Phase vs. dc-Bias voltage in "on" (blue) and "off" (red) states measured on a piece of 1.36 mm thick PCB mounted on metal disk at $R_H = 42\,\%$, (b)Amplitude vs. dc-Bias voltage measurement showing the typical "butterfly loops" on PCB mounted on metal disk, Phase vs. dc-Bias voltage in "on" (blue) and "off" (red) states measured on a piece of 1.36 mm thick PCB mounted on silicon at relative humidity of (c) $R_H = 33.3\,\%$, (d) $R_H = 41.8\,\%$. Amplitude vs. dc-Bias voltage measurement showing the typical "butterfly loops" on PCB mounted on silicon at relative humidity of (e) $R_H = 33.3\,\%$, (f) $R_H = 41.8\,\%$. (g) Triangular pulsed signal used for biasing the tip during spectroscopic measurements, (h) typical phase-switching behaviour in time domain.

It should be noted that in PFM measurements the hysteresis effects could also arise due to the capacitive coupling between the conducting tip and the sample. [222] In order to mitigate this effect all the spectroscopic data reported here were measured by employing a switching spectroscopy PFM (SSPFM) protocol pioneered by Jesse et al., where a sequence of dc voltages in triangular saw tooth form is applied between the conducting cantilever and the silicon wafer. [149, 150] A profile of the typical waveform applied during such measurements is shown in figure 6.12 (g) and the corresponding 180^0 phase switching in time domain is shown in figure 6.12 (h). Bias dependent responses of phase and amplitude were recorded in the "off" state to minimize the contribution of electrostatic interaction. [211] As it is seen in figure 6.12 (d) and figure 6.12 (f), the "off" state ϕ vs. V_{dc} and A vs. V_{dc} curves saturate at higher voltages than the curves recorded in the "on" state. In addition, the "coercive voltage" in the "off" state is also seen to be higher than that in the "on" state. This difference indicates that the role of electrostatic interaction in the observed results in the "off" state has been minimized.

In conclusion, we have performed PFM measurements on a popular semiconductors like Silicon, a material that is frequently used as a base material/substrate for PFM measurements and observed ferroelectric like hysteresis in phase vs. voltage and piezo-electric like "butterfly loops" in amplitude vs. voltage curves. The overall shape of the hysteresis loops depends on the level of relative humidity in the ambience during measurements. Furthermore, we have also shown how nano-meter scale topographic structures can be written on Silicon through AFM lithography under ambient conditions. We attribute all the observation to electrochemical processes taking place under the cantilever. When a thick non-ferroelectric sample material is mounted on silicon for PFM measurements, the hysteresis is observed on the sample which shows similar humidity dependence as silicon confirming that the observed hysteresis in such case results from silicon. This makes Silicon a bad choice as substrate for PFM measurements. Therefore, the observation of hysteresis loops alone

in PFM is not a proof of ferroelectricity and/or piezoelectricity in materials as strikingly similar hysteresis may also arise from phenomena other than ferroelectricity and/or piezoelectricity. Moreover, by performing PFM experiments on a large number of non-ferroelectric systems we have shown that PFM hysteresis and "butterfly loops" cannot be considered as "hallmark signatures" of ferroelectricity.

7 Summary

We have discovered a novel TISC phase at mesoscopic interfaces between pure elemental metals and the topological non-trivial systems like 3-D Dirac semi-metal Cd_3As_2, a Weyl semimetal TaAs and the topological nodal semimetal ZrSiS. The majority of my thesis work is devoted to the point contact studies of the topological material in search of topological superconductivity. Our home made point contact system is used to acquiring the spectra using all elemental tips to explore the spectroscopic informations on the unknown materials in ballistic regime of transport. In case of Cd_3As_2/Ag, the superconducting phase was seen to be unconventional in nature where a robust zero-bias conductance peak also appears which might, in principle, be attributed to a p-wave component in the order parameter symmetry. In contrast, the TISC observed in TaAs was found to be surprisingly conventional in nature. By employing the same technique it was also possible to induced a TISC phase in other topological systems like ZrSiS and $Pb_{0.6}Sn_{0.4}Te$, a topological crystalline insulator. [235] Based on our experiments on a limited number of topological systems out of a large number of such systems known, it is not possible to conclude anything about the possibility of a common mechanism of TISC for the entire class of topological systems. It is not known whether ALL topological materials will show a TISC phase at low enough temperatures. This discover is new and until now no concrete understanding of the mechanism through which the TISC phase emerges has not been achieved, we surmise that there could be multiple possibilities which are worth looking at in detail e.g., (a) the metallic tip might introduce local charge doping in a way so as to favor local superconductivity, (b) the point-contact might alter the local band structure underneath the tip by physically altering the local crystal structure and lowering the symmetry, which might help in stabilize a local superconducting phase, and (c) it is believed that the topological semimetals can be driven into topologically distinct phases under breaking of certain symme-

tries. [6, 45]. In this case the symmetry that can be lowered is the gauge symmetry which leads to a local phase coherence underneath the tip through stiffening of the phase of the order parameter which fluctuate otherwise. Due to that, superconductivity (TISC) appears under the point-contacts. Therefore, it is also possible that the emerging TISC phase in the topological semimetals emerges through a topological phase transition under a point contact geometry. Our results are strongly in favor of topological superconducting phase in topological semimetals, but additional theoretical work is needed to fully understand the results.

8 Future Outlook

The discovery of TISC in a wide range of topological systems provided a new route to realizing superconductivity at mesoscopic interfaces of non-superconducting systems. At present it is not clear whether the superconducting phase thus emerging in such non-trivial interfaces has topological properties or not. The main difficulty in addressing this issue is the extremely small volume fraction of superconductivity in TISC. However, a better understanding of TISC through controlled experiments can lead to better understanding of superconductivity and topological phase transitions. Following is a list of investigations that can be carried out in order to understand the phase better.

1) Investigation of the band structures in presence of a tip is required for every system that shows TISC. Such calculations may reveal whether the superconducting phase coexists with the topological properties or not.

2) There should be an extension of the PCAR experiments to explore the mesoscopic origin of emerging superconductivity under the point-contacts. In order to do that, it will be required to perform double probe scanning tunneling microscopy (STM) experiments. In such experiments, one probe can be used to induce superconductivity, and the other probe will do the spectroscopic measurements near the point of contact of the first probe and then move away from it. These experiments will clearly reveal the length scale of the TISC phase and will also help conclude on the possibility of emergence of superconductivity through stiffening of the phase of the order parameter.

3) It should be explored whether better control on the TISC phase can be achieved by engineering nano-structures on pristine surfaces of topological semimetals.

4) Detailed theoretical calculations are necessary to understand how a phase transition to a TISC phase takes place locally on topological semimetals.

BIBLIOGRAPHY

[1] B. P. Palash, *American Journal of Physics***79**, 485 (2011).

[2] M. Leijnse & K. Flensberg, *Semiconductor Science and Technology* **27**, 12 (2012).

[3] X. Wan, A. M.Turner, A. Vishwanath & S. Y. Savrasov, *Phys. Rev. B* **83**, 205101 (2011).

[4] A. A. Burkov & L. Balents, *Phys. Rev. Lett.* **107**, 127205 (2011).

[5] L. Fu, & C. Kane, *Phys. Rev. Lett.* **100**, 096407 (2008).

[6] M. Z. Hasan & C. L. Kane, *Rev. Mod. Phys.* **82**, 3045 (2010).

[7] Y. Ando & L. T. Fu, *Annu. Rev. Condens. Matter Phys.* **6**, 361 (2015).

[8] M. Wang, Y. Song, L. You, Z. Li, B. Gao, X. Xie & M. Jiang, *Scientific Reports* **6**, 22713 (2016).

[9] C. Q. Han *etal*, *Appl. Phys. Lett.* **107**, 171602 (2015).

[10] G. Du, Z. Du, D. Fang, H. Yang, R. D. Zhong, J. Schneeloch, G. D. Gu & H-H. Wen, *Phys. Rev. B* **92**, 020512 (2015).

[11] C. P. Xing *etal*, Nature Communications **6**, 7805 (2015).

[12] J. Zhu *etal*, *Scientific Reports* **3**, 2016 (2013).

[13] Y. Zhou *etal*, *PNAS* **113**, 2904 (2016).

[14] A. P. Drozdov, M. I. Eremets, I. A. Troyan, V. Ksenofontov & S. I. Shylin, *Nature* **525**, 73 (2015).

[15] P. P. Kong *et al.* , *Journal of physics: Condensed matter* **25**, 362204 (2013).

[16] J. L. Zhang *et al.* , *PNAS* **108**, 24 (2011).

[17] M. I. Tinkham, *Introduction to Superconductivity*, Dover, Second Edition (2004).

[18] Y. G. Naidyuk & I. K. Yanson, *Point-contact Spectroscopy*, Springer-Verlag New York (2005).

[19] S. Datta, *Electronic Transport in Mesoscopic Systems*, Cambridge University Press, Cambridge (1999).

[20] L. Janson, M. Klein, H. Lewis, A. Lucas, A. Marantan & K. U. Luna, *American Journal of Physics* **80**, 133 (2012).

[21] D. Daghero & R. S. Gonnelli, *Supercond. Sci. Tech.* **23** 043001 (2010).

[22] M. Cheng, R. M Lutchyn & S. D. Sarma, *Phys. Rev. B* **85**,165124 (2012).

[23] D. J. Clarke, J. D. Sau & S. D. Sarma. arXiv:1510.00007v2.

[24] E. Majorana, *Nuovo Cimento* **14**, 171 (1937).

[25] A. Wexler, *Proc* **89**, 927 (1966).

[26] G. Sheet, S. Mukhopadhyay & P. Raychaudhur, *Phys. Rev. B* **69**, 134507 (2004).

[27] A. M. Duif, A. G. M. Jansen & P. Wyder, *J. Phys.: Condens. Matter.* **l**, 3157 (1989).

[28] A. V. Khotkevich, K. Igor. Yanson, *Atlas of Point Contact Spectra of Electron-Phonon Interactions in Metals*, Springer US, the University of California (1995).

[29] A. I. Akimenko & I. K. Yanson, *JETP* **31**, 191 (1980).

[30] J. M. V. Ruitenbeek, *Conductance quantisation in metallic point contacts*, Springer Berlin Heidelberg (2000).

[31] Yu. V. Sharvin, *Sov. Phys. JETP* **21**, 655 (1965).

[32] A. F. Andreev, *JETP* **19**, 1228 (1964).

[33] G. E. Blonder, M. Tinkham & T. M. Klapwijk, *Phys. Rev. B* **25**, 4515 (1982).

[34] I. Giacver, *Phys. Rev. Lett.* **5**, 147 (1960)

[35] R. J. Soulen *et al.*, *Science* **282**, 85 (1998).

[36] I. I. Mazin, *Phys. Rev. Lett.* **83**, 1427 (1999).

[37] A. Plecenik, M. Grajcar, S. Benaka, P. Seidel & A. Pfuch, *Phys. Rev. B* **49**, 10016 (1994).

[38] A. G. M. Jansen, F. M. Mueller & P. Wyder, *Phys. Rev. B* **16**, 1325 (1977).

[39] P. N. Chubov, I. K. Yanson & A. I. Akimenko, *Sov. J. Low Temp. Phys.* **8**, 32 (1982).

[40] C.J. Muller, J.M. van Ruitenbeek, L.J. de Jongh. *Physica C: Superconductivity* **191**, 485 (1992).

[41] K. S. Ralls & R. A. Buhrman, *Phys. Lett.* **55**, (1989).

[42] Z. K. Liu *et al.*, *Science* **343**, 864 (2014).

[43] Z. K. Liu *et al.*, *Nature Materials* **13**, 677 (2014).

[44] S. M. S. Young *et al.*, *Phys. Rev. Lett.* **108**, 140405 (2012).

[45] Z. Wang *et al.*, *Phys. Rev. B* **85**, 195320 (2012).

[46] X. Wan, A. M. Turner, A. Vishwanath & S. Y. Savrasov, *Phys. Rev. B* **83**, 205101 (2011).

[47] X. -L. Qi & S. -C. Zhang, *Rev. Mod. Phys.* **83**, 1057 (2011).

[48] L. Fu & C. Kane, *Phys. Rev. Lett.* **100**, 096407 (2008).

[49] Z. Wang, H. Weng, Q. Wu, X. Dai & Z. Fang, *Phys. Rev. B* **88**, 125427 (2013).

[50] X.-L. Qi, T. L. Hughes & S.-C. Zhang, *Phys. Rev. B* **81**, 134508 (2010).

[51] S. Jeon *et al.*, *Nature Materials* **13**, 851 (2014).

[52] J. Bardeen, L. N Cooper & J. R. Schrieffer, *Phys. Rev.* **106**, 162 (1957).

[53] J. Bardeen, L. N Cooper & J. R. Schrieffer, *Phys. Rev.* **108**, 1175 (1957).

[54] Ch. Renner, B. Revaz, J. Y. Genoud, K. Kadowaki & O. Fischer, *Phys. Rev. Lett.* **80**, 149 (1998).

[55] M. Buchanan, *Nature* **409**, 8 (2001)

[56] G. Sheet *et al.*, *Phys. Rev. Lett.* **105**, 167003 (2010).

[57] H. Z. Arham *et al.*, *Journal of Physics: Conference Series* **400**, 022001 (2012).

[58] H. Y. Choi, Y, Bang & D. K. Campbell, *Phys. Rev. B* **61**, 9748 (2000).

[59] A. Sirohi, P. Saha, S. Gayen, A. Singh & G. Sheet, *Nanotechnology* **27**, 285701 (2016).

[60] Y. Tanaka & S. Kashiwaya, *Phys. Rev. Lett.* **74**, 3451 (1995).

[61] Y. Tanaka, Y. Tanuma, K. Kuroki & S. Kashiwaya, *J. Phys. Soc. Jpn.* **71**, 2102 (2002).

[62] M. Sato, Y. Tanaka, K. Yada, & T. Yokoyama, *Phys. Rev. B* **83**, 224511 (2011).

[63] Y. Tanaka, M. Sato & N. Nagaosa, *J. Phys. Soc. Jpn.* **81**, 011013 (2012).

[64] S. Sasaki *et al.*, *Phys. Rev. Lett.* **107**, 217001 (2011).

[65] S. Takami *et al.*, *J. Phys. Soc. Japan* **83**, 064705 (2014).

[66] A. Yamakage, K. Yada, K, M. Sato & Y. Tanaka, *Phys. Rev. B* **85**, 180509 (2012).

[67] S. Kashiwaya & Y. Tanaka, *Rep. Prog. Phys.* **63**, 1641 (1999).

[68] F. Wilczek, *Nature Physics* **5**, 614 (2009).

[69] F. Wilczek, *Nature* **486**, 195 (2012).

[70] Z. K. Liu *et al.*, *Science* **343**, 864 (2014).

[71] Z. K. Liu *et al.*, *Nature Mater.* **13**, 677 (2014).

[72] S. M. S. Young, S. Zaheer, J. C. Y. Teo, C. L. Kane, E. J. Mele & A. M. Rappe, *Phys. Rev. Lett.* **108**, 140405 (2012).

[73] L. Aggarwal, A. Gaurav, G. S. Thakur, Z. Haque, A. K. Ganguli & G. Sheet, *Nature Materials* **15**, 32 (2016).

[74] Y. Ando & L. Fu, *Annual Review of Condensed Matter Physics* **6**, 361 (2015).

[75] H. Y. Hui, J. D. Sau & S. D. Sarma, *Phys. Rev. B* **90**, 064516 (2014)

[76] W. S. Cole, S. D. Sarma & T. D. Stanescu, *Phys. Rev. B* **92**, 174511 (2015).

[77] F. Setiawan, P. M. R. Brydon, J. D. Sau & S. D. Sarma. arXiv:1503.060801v3.

[78] W. S. Cole, S. D. Sarma & T. D. Stanescu, *Phys. Rev. B* **92**, 174511 (2015).

[79] S. Takei, B. M. Fregoso, V. Galitski & S. D. Sarma, *Phys. Rev. B* **87**, 014504 (2013).

[80] X. Liu, J. D. Sau & S. D. Sarma. arXiv:1501.07273v2

[81] T. D. Stanescu, R. M. Lutchyn & S. D. Sarma, *Phys. Rev. Lett.* **110**, 186803 (2013)

[82] R. M. Lutchyn, T. D. Stanescu & S. D. Sarma, *Phys. Rev. Lett.* **106**, 127001 (2011)

[83] Y. Kim, M. Cheng, B. Bauer, R. M. Lutchyn & S. D. Sarma, *Phys. Rev. B* **90**, 060401(R) (2014)

[84] H. Y. Hui, A. M. Lobos, J. D. Sau & S. D. Sarma, *Phys. Rev. B* **90**, 224517 (2014).

[85] S. Ganeshan & S. D. Sarma, *Phys. Rev. B* **91**, 125438 (2015).

[86] T. D. Stanescu & S. D. Sarma, *Phys. Rev. B* **87**, 180504(R) (2013).

[87] S. Kobayashi & M. Sato, *Phys. Rev. Lett.* **115**, 187001 (2015).

[88] M. N. Ali, Q. Gibson, S. Jeon, B. B. Zhou, A. Yazdani & R. J. Cava, *Inorg. Chem.* **53**, 4062 (2014).

[89] S. Y. Xu *et al.*, *Science* **349**, 613 (2015).

[90] B. Q. Lv *et al.*, *Phys. Rev. X* **5**, 031013 (2015).

[91] G. Xu, H. M. Weng, Z. Wang, X. Dai & Z. Fang, *Phys. Rev. Lett.* **107**, 186806 (2011).

[92] S. M. Huang *et al.*, *Nat. Commun.* **6**, 7373 (2015).

[93] B. Q. Lv *et al.*, *Nat. Phys.* **11**, 724 (2015).

[94] X. C. Huang *et al.*, *Phys. Rev. X* **5**, 031023 (2015).

[95] H. Weng, C. Fang, Z. Fang, B. A. Bernevig & X. Dai, *Phys. Rev. X* **5**, 011029 (2015).

[96] C. L. Zhang *et al.*, *Nat. Commun.* **7**, 10735 (2016).

[97] C. Shekhar *et al.*, *Nat. Phys.* **11**, 645 (2015).

[98] S. Y. Xu *et al.*, *Sci. Adv.* **1** e1501092 (2015).

[99] H. Weyl, *I. Z. Phys.* **56**, 330 (1929).

[100] C. Zhang *et al.*, Tantalum monoarsenide: An exotic compensated semimetal. Preprint at [http://arxiv.org/abs/1502.00251]

[101] H. Murakawa *et al.*, *Science* **342**, 1490-1493 (2013).

[102] G. Chang *et al.*, *Phys. Rev. Lett.* **116**, 066601(1-6) (2016).

[103] S. Y. Xu *et al.*, *Phys. Rev. Lett.* **116**, 096801(1-7) (2016).

[104] S. Das *et al.*, *Appl. Phys. Lett.* **109**, 132601(1-5) (2016).

[105] G. Sheet, S. Mukhopadhyay & P. Raychaudhuri, *Phys. Rev. B* **69**, 134507(1-6) (2004).

[106] Y. G. Naidyuk & Yanson, I. K. *Point-contact Spectroscopy*, (Springer, 2004).

[107] M. Tinkham, *Introduction to Superconductivity*, 2nd edn, (McGraw-Hill, 2004).

[108] H. Wang *et al.*, *Nat. Mat.* **15**, 38 (2016).

[109] R. S. Gonnelli *et al.*, *Physical Review B* **79**, 184526(1-11) (2009)

[110] Y. Tanaka, M. Sato & N. Nagaosa, *J. Phys. Soc. Jpn* **81**, 011013 (2012).

[111] M. Sato, Y. Tanaka, K. Yada & T. Yokoyama, *Phys. Rev. B* **83**, 224511 (2011).

[112] A. A. Golubov, A. Brinkman, Y. Tanaka, I. I. Mazin & O. V. Dolgov, *Phys. Rev. Lett.* **103**, 077003 (2009).

[113] Y. Bugoslavsky *et al.*, *Phys. Rev. B* **71**, 104523(1-10) (2005).

[114] S. Anshu *et al.*, *Appl. Phys. Lett.*, **108**, 242411(1-5) (2016).

[115] T. Shang *et al.*, *Scientific Reports* **5**, 17734 (2015).

[116] A. Kandala, A. Richardella, S. Kempinger, C-X. Liu & N. Samarth, *Nat. Commun.* **6**, 7434 (2015).

[117] H. Wang *et al.*, Tip induced unconventional superconductivity on Weyl semimetal TaAs. [http://arxiv.org/abs/1607.00513].

[118] C. Shekhar, V. Süß & M. Schmidt,Mobility induced unsaturated high linear magnetoresistance in transition-metal monopnictides Weyl semimetals. [http://arxiv.org/abs/1606.066493].

[119] H. Boller & E.Parthe, *Acta Crystallogr.* **16** 1095 (1963).

[120] F. Arnold, M. Naumann, S.-C. Wu, Y. Sun, M. Schmidt, H. Borrmann, C. Felser, B. Yan & E. Hassinger *Phys. Rev. Lett.* **117**, 146401 (2016).

[121] D. Shoenberg, *Magnetic Oscillations in Metals*, Cambridge University Press, (2009).

[122] Y. T. Hsu, A. Vaezi, M. H. Fischer & E. A. Ki, *Nature Communications* **8**, 14985 (2017).

[123] Y. M. Lu, T. Xiang & D. H. Lee, *Nature Physics* **10**, 634 (2014).

[124] C. Beenakker & L. Kouwenhoven, *Nature Physics* **12**, 618 (2016).

[125] R. Sankar *et al.*, *Scientific Reports* **7**, 40603 (2017).

[126] M. Neupane *et al.*, *Physical Review B* **93**, 201104 (2016).

[127] M. Leslie *et al.*, *Nature Communications* **7**, 11696 (2016).

[128] K. H. Jin, H. W. Yeom & S. H. Jhi, *Physical Review B* **93**, 075308 (2016).

[129] W. Ko *et al.*, *Scientific Reports* **3**, 2656 (2013).

[130] Y-Y. Lv, B-B. Zhang, X. Li, S-H. Yao, Y. B. Chen, J. Zhou, S-T. Zhang, M-H. Lu & Y-F. Chen, *Appl. Phys. Lett.* **108**, 244101 (2016).

[131] M. Matusiak, J. R. Cooper & D. Kaczorowski, *Nature Communications* **8**, 15219 (2017).

[132] L. Aggarwal, S. Gayen, S. Das, R. Kumar, V. S, C. Shekhar, C. Felser & G. Sheet, *Nature Communications* **8**, 13974 (2017).

[133] R. Singha, B. Satpati & P. Mandal, arXiv:1609.09397v2 (2017).

[134] G. Binnig, C. F. Quate, & Ch. Gerber, *Phys. Rev. Lett.* **56**, 930 (1986).

[135] G. Binnig, *Atomic Force Microscope and Method for Imaging Surfaces with Atomic Resolution*, US Patent No. 4, 724, 318 (1986).

[136] G. Meyer & N. M. Amer, *Appl. Phys. Lett.* **56**, 2100 (1990).

[137] D. M. Eigler & E. K. Schweizer, *Nature* **344**, 524 (1990).

[138] L. Aggarwal, J. S. Sekhon, S. N. Guin, A. Arora, D. S. Negi, R. Datta, K. Biswas & G. Sheet, *Applied Physics Letters* **105**, 113903 (2014).

[139] J. S. Sekhon, L. Aggarwal & G. Sheet, *Applied Physics Letters* **104**, 162908 (2014).

[140] L. Aggarwal, A. Banik, S. Anand, U. V. Waghmare K. Biswa & G. Sheet, *Journal of Materiomics* **2**, 196 (2016).

[141] S. Kasas, V. Gotzos & M. R. Celio, *Biophys. J. Biophysical Society* **64**, 539 (1993).

[142] C. Bustamante, J. Vesenka, C. L. Tang, W. Rees, M. Guthold & R. Keller, *Biochemistry* **31**, 22 (1992).

[143] S. Maji, P. K. Sarkar, L. Aggarwal, S. K. Ghosh, D. Mandal, G. Sheet & S. Acharya, *Phys. Chem. Chem. Phys.* **17**, 8159 (2015).

[144] R. Bennewitz, M. Bammerlin & E. Meyer, 2002, Noncontact Atomic Force Microscopy, S. Morita, R. Wiesendanger, and E. Meyer (Springer, Berlin), Chap. 5, pp. 93108.

[145] Y. Martin, D. Rugar & H. K. Wickrama singhe, *Appl. Phys. Lett.* **52**, 244 (1988).check

[146] M. Alexe, A. G Nanoscale Characterisation of Ferroelectric Materials. *Scanning Probe Microscopy*, Springer (2004).

[147] Shubhra Jyotsna, Ashima Arora, Jagmeet S. Sekhon, & Goutam Sheeta, *Journal of Applied Physics* **116**, 104903 (2014).

[148] B. J. Rodriguez, C. Callahan, S. V. Kalinin & R. Proksch, *Nanotechnology* **18**, 475504 (2007).

[149] S. Jesse, B. Mirman & S. V. Kalinin, *Appl. Phys. Lett.* **89**, 022906 (2006).

[150] S. Jesse, A. P. Baddorf & S. V. Kalinin, *Appl. Phys. Lett.* **88**, 062908 (2006).

[151] K. Biswas, J. He , Q. Zhang ,G. Wang , C. Uher , V. P. Dravid & M. G. Kanatzidis, *Nat. Chem.* **3**, 160 (2011).

[152] K. Biswas, J. He, I. D. Blum, Chun-I Wu, T. P. Hogan, D. N. Seidman, V. P. Dravid & M. G. Kanatzidis, *Nature* **489**, 414 (2012).

[153] L. D. Zhao, S. H. Lo, Y. Zhang, H. Sun, G. Tan, C. Uher, C. Wolverton, V. P. Dravid & M. G. Kanatzidis, *Nature* **508**, 373 (2014).

[154] Y. Pei, X. Shi, A. LaLonde, H. Wang, L. Chen & G. J. Snyder, *Nature* **473**, 66 (2011).

[155] J. P. Heremans, V. Jovovic, E. S. Toberer, A. Saramat, K. Kurosaki, A. Charoenphakdee, S. Yamanaka & G. J. Snyder, *Science* **321**, 554 (2008).

[156] B. Poudel *et al.*, *Science* **320**, 634 (2008).

[157] A. Tombak, J. P. Maria, F. T. Ayguavives, Z. Jin, G. T. Stauf, A. I. Kingon & A. Mortazawi, *IEEE Trans. Microw. Theory Tech* **51**, 462 (2003).

[158] A. Stamm, D. J. Kim, H. Lu, C. W. Bark, C. B. Eom and A. Gruverman, *Appl. Phys. Lett.* **102**, 092901 (2013).

[159] Z. Hu, M. Tian, B. Nysten & A. M. Jonas, *Nature Materials* **8**, 62 (2009).

[160] P. Muralt, *Micromech. Microeng.* **10**, 136 (2000).

[161] J. F. Scott, *Science* **315**, 954 (2007).

[162] R. C. G. Naber, C. Tanase, P. W. M. Blom, G. H. Gelinck, A. W. Marsman, F. J. Touwslager, S. Setayesh & D. M. D. Leeuw, *Nature Materials* **4**, 243 (2005).

[163] Y. Yuan, Z. Xiao, B. Yang & J. Huang, *J. Mater. Chem. A* **2**, 6027 (2014).

[164] S. Lanfredi, G. Palacio, F. S. Bellucci, C. V. Colin & M. A. L. Nobre, *J. Phys. D* **45**, 435302 (2012).

[165] Y. Shen, D. R. Clarke & P. A. Fuierer, *Appl. Phys. Lett* **93**, 102907 (2008).

[166] S. Lee, J. A. Bock, S. T. McKinstry & C. A. Randall, *Journal of the European Ceramic Society* **32**, 3971 (2012).

[167] E. S. Bozin, C. D. Malliakas, P. Souvatzis, T. Proffen, N. A. Spaldin, M. G. Kanatzidis & S. J. L. Billinge, *Science* **330**, 1660 (2010).

[168] O. Delaire *et al.*, *Nature Mater* **10**, 614 (2011).

[169] T. Kolodiazhnyi, *Phys. Rev. B* **78**, 045107 (2008).

[170] N. Balke *et al.*, *Nature Physics* **8**, 81 (2012).

[171] S. N. Guin, A. Chatterjee, D. S. Negi, R. Datta & K. Biswas, **6**, 2603 (2013).

[172] S. N. Guin, D. S. Negi, R. Datta & K. Biswas, *J. Mater. Chem. A* **2**, 4324 (2014).

[173] D. T. Morelli, V. Jovovic & J. P. Heremans, *Phys Rev. Lett.* **101**, 035901 (2008).

[174] M. D. Nielsen, V. Ozolins & J. P. Heremans, *Energy Environ. Sci.* **6**, 570 (2013).

[175] R. Seshadri & N. A. Hill, *Chem. Mater.* **13**, 2892 (2001).

[176] U. V. Waghmare, N. A. Spaldin, H. C. Kandpal & R. Seshadri, *Phys. Rev. B* **67**, 125111 (2003).

[177] J. B. Neaton, C. Ederer, U. V. Waghmare, N. A. Spaldin & K. M. Rabe, *Phys. Rev. B* **71**, 014113 (2005).

[178] C. N. R. Rao & C. R. Serrao, *J. Mater. Chem.* **17**, 4931 (2007).

[179] K. Hoang, S. D. Mahanti, J. R Salvador & M. G. Kanatzidis, *Phys. Rev. Lett.* **99**, 156403 (2007).

[180] S. V. Barabash, V. Ozolins & C. Wolverton, *Phys. Rev. Lett.* **101**, 155704 (2008).

[181] J. Ma *et al.*, *Nature Nanotech.* **8**, 445 (2013).

[182] S. N. Guin & K. Biswas, *Chem. Mater.* **25**, 3225 (2013).

[183] M. A. Weilert, M. E. Msall, J. P. Wolfe & A. C. Anderson, *J. Phys. B.* **91**, 179 (1993).

[184] H. W. Jang, D. Ortiz, S. H. Baek, C. M. Folkman, R. R. Das, P. Shafer, Y. Chen, C. T. Nelson, X. Pan, R. Ramesh & C. B. Eom, *Advanced Mater.* **21**, 817 (2009).

[185] P. Fons, A. V. Kolobov, M. Krbal, J. Tominaga, K. S. Andrikopoulos, S. N. Yannopoulos, G. A. Voyiatzis & T. Uruga, *Phys. Rev. B* **82**, 155209 (2010).

[186] T. Matsunaga, P. Fons, A. V. Kolobov, J. Tominaga & N. Yamada, *App. Phys. Lett.* **92**, 231907 (2011).

[187] H. Krakauer, R. Yu, C.-Z. Wang, K. M Rabe & U. V. Waghmare, *J. Phys. Condens Mater.* **11**, 3779 (1999).

[188] S. Kastbjerg, N. Bindzus, M. Sndergaard, S. Johnsen, N. Lock, M. Christensen, M. Takata, M. A. Spackman & I. B. Brummerstedt, *Adv. Funct. Mater.* **23**, 5477 (2013).

[189] X. Zhang, L. D. Zhao, *J Materiomics* **1**, 92 (2015).

[190] Y. Tang, S. W. Chen & G. J. Snyder, *J Materiomics* **1**, 75 (2015).

[191] A. Sussardi, T. Tanaka, A. U. Khan, L. Schlapbach, T.Mori, *J. Materiomics* **1** 19‘6 (2015).

[192] Y. Zhang, X. Ke, P. R. C. Kent, J. Yang & C. Chen, *Phys. Rev. Lett.* **107**, 175503 (2011).

[193] H. Kim & M. Kaviany, *Phys. Rev. B* **86**, 045213 (2012).

[194] T. Keiber, F. Bridges & B. C. Sales, *Phys. Rev. Lett.* **11**, 095504 (2013).

[195] Q. Zhang, B. Liao, Y. Lan, K. Lukas, W. Liu, K. Esfarjani, C. Opeil, D. Broido, G. Chen & Z. Ren, *Proc. Natl. Acad. Sci.* **110**, 13261(2013).

[196] A. Banik & K. Biswas, *J. Mater. Chem. A* **2**, 9602 (2014).

[197] G. Tan, L-D. Zhao, F. Shi, J-W. Doak, S-H. Lo, H. Sun, C. Wolverton, V. P. Dravid, C. Uher & M. G. Kanatzidis, *J. Am. Chem. Soc.* **136**, 7006 (2014).

[198] A. Banik, S. U. Shenoy, S. Anand, U. V. Waghmare & K. Biswas, *Chem. Mater.* **27**, 581 (2015).

[199] T. H. Hsieh, H. Lin, J. Liu, W. Duan, A. Bansil & L. Fu, *Nat. Commun.* **3**, 982 (2012).

[200] Y. Tanaka., Z. Ren, T. Sato, K. Nakayama, S. Souma, T. Takahashi, K. Segawa & Y. Ando, *Nat. Phys.* **8**, 800 (2012).

[201] J. Liu, T. H. Hsieh, P. Wei, W. Duan, J. Moodera & L. Fu, *Nat. Mater.* **13**, 178 (2014).

[202] K. R. Knox, E. S. Bozin, C. D. Malliakas, M. G. Kanatzidis & S. J. L. Billinge, *Phys. Rev. B* **89**, 014102 (2014).

[203] K. V. Mitrofanov, A. V. Kolobov, P. Fons, M. Krbal, T. Shintani, J. Tominaga & T. Uruga, *Phys. Rev. B* 90, 134101 (2014).

[204] O. Delaire, J. Ma, K. Marty, A. F. May, M. A. McGuire, M. -H. Du, D. J. Singh, A. Podlesnyak, G. Ehlers, M. D. Lumsden & B. C. Sales, *Nat. Mater.* **10**, 614 (2011).

[205] T. Shiga, J. Shiomi, J. Ma, O. Delaire, T. Radzynski, A. Lusakowski, K. Esfarjani & G. Chen, *Phys. Rev. B* **85**, 155203 (2012).

[206] C. W. Li, O. Hellman, J. Ma, A. F. May, H. B. Cao, X. Chen, A. D. Christianson, G. Ehlers, D. J. Singh, B. C. Sales & Delaire, *Phys. Rev. Lett.* **112**, 175501 (2014).

[207] S. Lee, K. Esfarjani, T. Luo, J. Zhou, Z. Tian & G. Chen, *Nat. Commun.* **5**, 3525 (2014).

[208] M. J. Polking, M. Han, A. Yourdkhani, V. Petkov, C. F. Kisielowski, V. V. Volkov, Y. Zhu, G. Caruntu, A. P. Alivisatos & R. Ramesh,*Nat. Mater.* **11**, 700 (2012).

[209] F. Priolo, T. Gregorkiewicz, M. Galli & T. Krauss, *Nature Nanotechnology* **9**, 19 (2014).

[210] M. Lebedev, J. Akedo & Y. Akiyama, *Jpn. J. Appl. Phys.* **39**, 5600 (2000).

[211] Y. Liu, Y. Zhang, M. J. Chow, N. Q. Chen & J. Li, *Phys. Rev. Lett.* **108**, 078103 (2012).

[212] E. Soergel, *J. Phys. D: Appl. Phys.* **44**, 464003 (2011).

[213] S. V. Kalinin, B. J. Rodriguez, S. Jesse, P. Maksymovych, K. Seal, M. Nikiforov, A. P. Baddorf, A. L. Kholkin & R. Proksch, *Materials today* **11**, 16 (2008).

[214] C. Dubourdieu, J. Bruley, T. M. Arruda, A. Posadas, J. Jordan-Sweet, M. M. Frank, E. Cartier, D. J. Frank, S. V. Kalinin, A. A. Demkobv & V. Narayan, *Nature Nanotechnology* **8**, 748 (2013).

[215] M. Narayanan M. Pan, S. Liu, S. Tong, S. Hong, B. Ma & U. Balachandran, *RSC Advances* **2**, 11901 (2012).

[216] B.J. Rodriguez, S. V. Kalinin, J. Shin, S. Jesse, V. Grichko, T. Thundat, A. P. Baddorf & A. Gruverman, *Journal of Structural Biology* **153**, 151 (2006).

[217] S. B. Lang, S. A. M. Tofail, A. L. Kholkin, M. Wojtas, M. Gregor, A. A. Gandhi, Y. Wang, S. Bauer, M. Krause & A. Plecenik, *Scientific Reports* **3**, 1 (2013).

[218] P. M. Campbell, E. S. Snow, P. J. McMarr, *Physica B* **227**, 315 (1996).

[219] J. B. Wang, M. Y. Lai, Y. L. Wang, *Chinese Journal of Physics* **36**, 642 (1998).

[220] D. Wang, L. Tsau, K. L. Wang, *Applied Physics Letter* **65**, 1415 (1994).

[221] M. T. Asmah, S. D. Hutagalung, O. Sidek, *Journal of Physics: Conference Series* **431**, 1 (2013).

[222] J. A. Dagata, F. Perez-Murano, C. Martin, H. Kuramochi, H. Yokoyama, *J. Appl. Phys.* **96**, 2386 (2004).

[223] M. Tello, R. Garcia, *Appl. Phys. Lett.* **79**, 424 (2001).

[224] S. V. Kalinin, E. Karapetian, M. Kachanov, *Phys. Rev. B* **70**, 184101 (2004).

[225] A. Dehzangi, F. Larki, S. D. Hutagalung, M. G. Naseri, B. Y. Majilis, M. Navasery, N. A. Hamid, M. M. Noor, PLOSone **8**, 1 (2013).

[226] X. N. Xie, H. J. Chung, C. H. Sow, A. T. S. Wee, Materials Science and Engineering R **54**, 1 (2006).

[227] A. Giguere, J. Beerens, B. Terreault, *Nanotechnology* **17**, 600 (2006).

[228] X. Jiang, G. Wu, J. Zhou, S. Wang, A. A. Tseng & Z. Du, *Nanoscale Research Letters* **6**, 518 (2011).

[229] R. Garcia, R. V. Martinez, J. Martinez, *Chem. Soc. Rev.* **35**, 29 (2006).

[230] A. Morozovska, E. Eliseev, N. Balke & S.V. Kalinin, J. Appl. Phys. **108**, 053712 (2010).

[231] N. Balke, S. Jesse, Y. Kim, L. Adamczyk, I. N. Ivanov, N. J. Dudney & S. V. Kalinin, *ACS Nano* **4**, 7349 (2010).

[232] R. Proksch, e-print arXiv:1312.6933.

[233] D. Andrienko, Cyclic Voltammetry, January 22, (2008).

[234] A. N. Morozovska, E. A. Eliseev, S. V. Kalinin, *Appl. Phys. Lett.* **89**, 192901 (2006).

[235] S. Das, L. Aggarwal, S. Roychowdhury, M. Aslam, S. Gayen, K. Biwas & G. Sheet, *Applied Physics Letters* **109**, 13 (2016).